DEPARTMENT OF TRANSPORTATION

Performance Specification for Geogrid Reinforced Aggregate Base

John Siekmeier, Principal Investigator
Office of Materials and Road Research
Minnesota Department of Transportation

October 2018

Research Project
Final Report 2018-30

To request this document in an alternative format, such as braille or large print, call 651-366-4718 or 1-800-657-3774 (Greater Minnesota) or email your request to ADArequest.dot@state.mn.us. Please request at least one week in advance.

Technical Report Documentation Page

1. Report No.	2.	3. Recipients Accession No.
MN/RC 2018-30		

4. Title	5. Report Date
Performance Specification for Geogrid Reinforced Aggregate Base	October 2018
	6.

7. Author	8. Performing Organization Report No.
John Siekmeier	

9. Performing Organization Name and Address	10. Project/Task/Work Unit No.
Minnesota Department of Transportation Office of Materials and Road Research Mailstop 645 1400 Gervais Avenue Maplewood, MN 55109	11. Contract (C) or Grant (G) No. (C) LAB1026258

12. Sponsoring Organization Name and Address	13. Type of Report and Period Covered
Minnesota Department of Transportation Research Services & Library 395 John Ireland Boulevard, MS 330 St. Paul, Minnesota 55155-1899	Final Report 14. Sponsoring Agency Code

15. Supplementary Notes

http:// mndot.gov/research/reports/2018/201830.pdf

16. Abstract (Limit: 250 words)

A performance specification has been developed for geogrid reinforced aggregate base, which utilizes the dynamic cone penetrometer (DCP) and light weight deflectometer (LWD) to test the aggregate base reinforced with geogrid. These quality assurance devices, in particular the DCP, are very familiar to construction inspection staff in Minnesota, and therefore this performance specification is expected to be readily implemented. In summary, the construction quality assurance test locations are selected to accurately represent the constructed aggregate base layer and the DCP or LWD is placed at the appropriately prepared test location. For both the DCP and LWD, the weight is raised and released to deliver a predetermined number of drops that result in a measured penetration (DCP-MV) or plate displacement (LWD-MV), which is then compared to a predetermined target value (DCP-TV or LWD-TV).

17. Document Analysis/Descriptors	18. Availability Statement
Geogrids, Performance based specifications, Aggregates, Discrete systems, Deflectometers, Cone penetrometers	No restrictions. Document available from: National Technical Information Services, Alexandria, Virginia 22312

19. Security Class (this report)	20. Security Class (this page)	21. No. of Pages	22. Price
Unclassified	Unclassified	175	

PERFORMANCE SPECIFICATION FOR GEOGRID REINFORCED AGGREGATE BASE

FINAL REPORT

Prepared by:

John Siekmeier
Office of Materials and Road Research
Minnesota Department of Transportation

October 2018

Published by:

Minnesota Department of Transportation
Research Services & Library
395 John Ireland Boulevard, MS 330
St. Paul, Minnesota 55155-1899

ACKNOWLEDGMENTS

The contributions of the technical advisory panel members, technical liaison Bruce Tanquist, MnDOT Bemidji District staff, student interns Amy Guo and Joe Casanova, and the Minnesota Local Road Research Board are gratefully acknowledged. Tensar International is also gratefully acknowledged for granting access to the geogrid modeling methodology developed on its behalf by Itasca Consulting Group.

TABLE OF CONTENTS

LIST OF FIGURES

LIST OF TABLES

EXECUTIVE SUMMARY

A performance specification has been developed for geogrid reinforced aggregate base, which utilizes the dynamic cone penetrometer (DCP) and light weight deflectometer (LWD) to test the aggregate base reinforced with geogrid. These quality assurance devices, in particular the DCP, are very familiar to construction inspection staff in Minnesota, and therefore this performance specification is expected to be readily implemented. In summary, the construction quality assurance test locations are selected to accurately represent the constructed aggregate base layer and the DCP or LWD is placed at the appropriately prepared test location. For both the DCP and LWD, the weight is raised and released to deliver a predetermined number of drops that result in a measured penetration (DCP-MV) or plate displacement (LWD-MV), which is then compared to a predetermined target value (DCP-TV or LWD-TV).

These construction quality assurance target values are based on the required pavement foundation strength and stiffness determined during design. MnDOT's flexible pavement design method, MnPAVE-Flexible, links the design inputs to these construction measurements and estimates pavement life. MnPAVE-Flexible has been enhanced using the pavement design package added to the PFC3D distinct element software to support creation and cyclic triaxial compression testing of an unsaturated aggregate base containing geogrid. The geogrid provides lateral restraint to the aggregate base as a result of interlocking and friction between the geogrid and the aggregate particles. The macroscopic system properties are affected by the microstructural properties. Therefore, the modeled system can be used to study and quantify the effect of the microstructural properties on the macroscopic system such as the stress-strain relationship produced during cyclic triaxial tests at different confining stresses. The macrostructural properties specific to the geogrid include aperture shape and structural stiffness. The microstructural properties of the geogrid include rib dimensions, rib stiffness, and rib surface friction. The microstructural properties of the aggregate base include particle size, particle type (density, Young's modulus, Poisson's ratio, and surface friction), moisture content (tensile stress and separation distance), and initial aggregate base porosity.

The pavement design package provides a mechanistically defensible model for aggregate-geogrid interaction. The package is being used to improve pavement design methodology in Minnesota by estimating geogrid gain factors and unsaturated gain factors for typical roadway configurations in which the aggregate size distribution, initial porosity, moisture content, and confining stress are varied. A simplified geogrid gain factor adjustment is being trialed for MnDOT pavement design on projects where geogrid is being considered (MnPAVE-Flexible Beta 2018). The current work builds on previous studies and specifically addresses the benefits of geogrid reinforced aggregate base at lower strains by applying the distinct element method to better understand the aggregate-geogrid interaction. In addition, the importance of moisture is quantified mechanistically by applying suction (tensile stress) between aggregate particles at defined separation distances.

CHAPTER 1: INTRODUCTION

1.1 GEOSYNTHETICS

The two main types of geosynthetics used in roadways are geotextiles and geogrids. This report is focused on geogrids, and therefore the benefits of geotextiles will not be discussed. The structural benefits of geogrid have been described as: lateral restraint, modified failure surface, and tensioned membrane (Erickson and Drescher 2001). Lateral restraint occurs when the properly placed geogrid constrains the unbound pavement foundation material. Modified failure surface occurs when the geogrid reinforces a potential failure surface and increases the bearing capacity. Tensioned membrane occurs when deflection is resisted by the tensile stiffness of the geogrid acting similar to a trampoline. Geogrid is a petroleum product typically made of polypropylene or polyethylene that is punched and stretched, or woven, to create a planar structure. Geogrid can be further split into three broad categories: uniaxial, biaxial, and triaxial. Uniaxial geogrid provides tensile stiffness and strength mainly in one planar direction. Biaxial geogrid provides tensile stiffness and strength both longitudinally and laterally. Triaxial geogrid provides additional deformation resistance in the plane of the geogrid due its triangular truss-like structure. The benefits of geogrid reinforced aggregate base have been well quantified during the last decade in many publications that include the extensive study by Nazzal in 2007 up to the recently published study by the National Cooperative Highway Research Program (NCHRP 2017). The current work described in the following pages builds on these previous studies and specifically addresses the benefits of geogrid reinforced aggregate base at lower strains by applying the distinct element method to better understand the geogrid-aggregate interaction. In addition, the importance of moisture is quantified mechanistically by applying suction (tensile stress) between aggregate particles at defined separation distances.

1.2 MINNESOTA APPLICATIONS

In Minnesota, geogrid has traditionally been used to provide a more stable construction platform by improving the strength of the pavement foundation when weak soils are present (Clyne 2011). A more recent geogrid application has been to provide additional stiffness to the aggregate base layer, which can then more effectively protect the underlying soil layers from traffic loads. Geogrid reinforcement is known to help increase aggregate compaction during construction and it is also expected to improve both the short-term and long-term performance of roadways (Skallman 2010). However, because greater justification of this expectation was desired, the investigation described in this report was undertaken in three phases to better understand and quantify the structural benefit of geogrid on the performance of asphalt surfaced roadways.

Phase one of the investigation combined the analyses completed by Braun Intertec (Oman 2013) with analyses using the mechanistic empirical pavement design program, MnPAVE-Flexible (Tanquist 2012). During the spring of 2013 Braun Intertec conducted falling weight deflectometer tests on two trunk highways in the Bemidji District to compare roadways with geosynthetics to roadways without

geosynthetics. Using the information delivered by Braun Intertec, two of the Bemidji District test sections were investigated in more detail using the layered elastic analyses (Casanova and Siekmeier 2013). One test section included biaxial geogrid and the second test section, which was very similar in structure and materials, did not include geogrid. As a result of that comparison it was confirmed that geogrid provided benefit, but the relative amount of benefit was uncertain due to soil variability under the roadway. It was concluded that the geogrid generally reduces pavement deflection, but it was not possible to accurately quantify the structural benefit due to variability of the recycled aggregate base produced by full depth reclamation and the variability of the in situ soil layers.

Phase two of this investigation began in 2014 when Itasca Consulting Group was contracted by MnDOT to enhance its distinct element software Particle Flow Code 3D (PFC3D). PFC3D was used to estimate the increased stiffness of geogrid reinforced aggregate base for use in MnPAVE-Flexible. The conclusions contained in that report are based on field and laboratory testing combined with numerical analyses performed using both PFC3D and MnPAVE-Flexible (Siekmeier and Casanova 2016). The third phase of this investigation is described in the following pages.

1.3 AUTOMATED PLATE LOAD TEST AND FALLING WEIGHT DEFLECTOMETER

The automated plate load test system developed by Ingios Geotechnics performs cyclic plate load testing on the surface using varying cyclic loading frequencies and stresses. The cyclic tests are designed to obtain frequency and stress dependent dynamic modulus values and permanent deformation characteristics of the asphalt layer and stress dependent resilient moduli values of the underlying base and subgrade layers. The cyclic test process uses a controlled load pulse duration similar to AASHTO TP62 and AASHTO T324 methods for asphalt and AASHTO T307 resilient modulus method for foundation layers. The advantage of cyclic tests is that the modulus measurements better represent the true field stiffness values because thousands of dynamic load pulses can be applied to the surface of pavement layers (Wayne, Kwon and White 2014).

Ingios was contracted by MnDOT to perform automated plate load testing on geogrid reinforced test sections in Bemidji District during 2016 (White and Vennapusa 2016). In addition, Ingios partnered with the National Road Research Alliance during the reconstruction of MnROAD during 2017 to perform both automated plate load testing and validated intelligent compaction on geogrid reinforced test sections (White and Vennapusa 2017).

The falling weight deflectometer (FWD) is a trailer-mounted pavement testing device designed to simulate the deflection of pavements due to truck loads. A large mass is dropped and the deflection basin measured using sensors at the pavement surface. FWDs are particularly useful for estimating the in situ layer moduli of asphalt, aggregate base, granular subbase, and engineered soil using backcalculation. The FWD includes a load cell, which measures the force delivered to the road surface, and several geophones, which measure velocities that are used to calculate deflections.

Braun Intertec was contracted by MnDOT to perform FWD testing on geosynthetic reinforced test sections in Bemidji District during the spring of 2013 just after the thaw was complete. Braun Intertec

concluded that properly placed geogrid can reduce pavement deflection. However, as noted in the report, these benefits were difficult to quantify due to several uncertainties at the tested locations. Braun Intertec also recommended further analyses be done using more advanced modeling such as layered elastic methods and distinct element methods (Oman 2013).

1.4 MECHANISTIC EMPIRICAL PAVEMENT DESIGN

MnPAVE-Flexible (Tanquist 2012) is MnDOT's mechanistic empirical flexible pavement design method that consists of three general inputs; climate, traffic, and structure, and three design levels; basic, intermediate, and advanced. MnPAVE-Flexible has been adopted as MnDOT's pavement design method because unlike other methods, MnPAVE-Flexible can better optimize materials (Skok et al 2003). The effect of traffic on the pavement structure is simulated in MnPAVE-Flexible using layered elastic analysis performed with the WESLEA software routine (Van Cauwelaert 1989). MnPAVE-Flexible assumes that the pavement layers are isotropic in all directions and infinite in the horizontal direction. The fifth layer is also assumed to be infinite in the vertical direction. MnPAVE-Flexible inputs include layer thickness, modulus, Poisson's ratio, and an index indicating the degree of slip between layers (currently zero slip). The estimated pavement life is calculated using a damage factor based on Miner's hypothesis. MnPAVE-Flexible's climate inputs include five seasons (fall, winter, early spring, late spring, and summer) based on FWD measured material properties. Spring is split into two seasons because of important differences in behavior between the aggregate base and subgrade soil during the spring thaw (Ovik et al 2000). Seasonal temperatures are determined using local weather data at specific locations. The advanced structure tab allows the moduli of the asphalt, aggregate base, granular subbase, engineered soil, and geogrid to be entered (MnPAVE-Flexible Beta 2018).

1.5 NUMERICAL MODELING

The modeling methodology described in this report is based on the approach used by the United States Bureau of Mines (Siekmeier and O'Connor 1993) and patterned after the guidelines outlined by Starfield and Cundall (1988), which encourage the application of numerical modeling to gain understanding of the mechanics that characterize the system and not to obtain unique values for specific parameters. Hart and Cundall (1992) explain that computer simulations can be used as a laboratory to perform experiments on the system resulting in improved understanding of mechanics, knowledge of parameter dependence, and a means to test hypotheses. Ultimately, this new knowledge leads to greater understanding and the ability to create simpler tools, which only contain the most significant parameters that significantly influence the system.

The distinct element method is a type of numerical modeling that computes the motion of individual particles and the forces between particles by applying Newton's laws of motion (Cundall and Strack 1979). This is different than the finite element method, which is intended for modeling continuum problems where simulating the interaction of distinct particles is not desired. The distinct element method was used for this project because it is important to better understand and quantify the interaction of the aggregate particles with the geogrid. This model provides an approach consistent with mechanistic pavement design and performance based construction testing. The geogrid reinforced

aggregate base layered system constructed in the field is simulated in the numerical model using the geostructural element methodology applied earlier to layered rock (Siekmeier and O'Connor 1993).

Itasca was contracted by MnDOT to develop a PFC3D numerical model capable of simulating compression testing of an aggregate base material containing geogrid. The model boundary conditions were determined using the FWD measurements and MnPAVE-Flexible analyses. Moisture was added to the model by implementing research funded by MnDOT completed by the University of Minnesota and geogrid was added by implementing research funded by Tensar International Corporation that had been completed by Itasca in Germany. The synthetic material created in a PFC3D model simulates the movement and interaction of thousands of particles, which may be spherical grains or arbitrarily shaped clumps of grains that both translate and rotate independently. Each particle interacts with adjacent particles at their contacts, which are controlled by interaction laws, and internal forces and moments, which are updated using a time evolution method to dynamically solve Newton's laws of motion (Potyondy and Cundall 2004).

CHAPTER 2: GEOGRID SIMULATIONS

2.1 PROJECT OVERVIEW

The research described in this report is the third phase of a research initiative sponsored by MnDOT and the Local Road Research Board to better understand and quantify the structural benefit of geogrid in the aggregate base layer of asphalt surfaced roadways. The initial phase of the investigation combined the analyses completed Oman (2013) with analyses using the mechanistic empirical flexible pavement design program MnPAVE-Flexible (Casanova and Siekmeier 2013).

Quantifying the structural benefit of geogrid was addressed in the second phase of the investigation, which began in 2014 when Itasca was contracted by MnDOT to develop a PFC3D numerical model capable of simulating the creation and triaxial testing of an unsaturated aggregate base material containing geogrid (Potyondy 2015, 2015a, 2015b, Potyondy et al 2016, Siekmeier and Casanova 2016). Modeling capabilities were delivered in three parts. The first part included development of a synthetic granular material and the ability to simulate triaxial testing of that material. The second part added moisture to the synthetic material by implementing research funded by MnDOT and the Local Road Research Board that had been completed by the University of Minnesota (Gupta et al 2007, 2005, Tan at al 2014, Yonannes et al 2009). The third part added geogrid to the synthetic material by implementing research funded by Tensar International that had been completed by Itasca Consultants GmbH (Jas et al 2015). During part three, Itasca completed development of the pavement design package that supports creation and triaxial testing of the synthetic system consisting of unsaturated granular material containing geogrid.

The current project described in the following pages utilizes the capabilities of the enhanced PFC3D pavement design package, which now includes geogrid geometry and construction quality assurance performance testing. This report summarizes that work, which is fully described in Potyondy (2018a, 2018b, and 2018c). The PFC3D pavement design package supports creation of a hill material (Potyondy, 2016) in which biaxial or triaxial geogrids may be embedded, testing of the geogrids to obtain their macroscopic properties, and testing of the simulated pavement foundation materials. The materials and geogrid are created in either a polyaxial or cylindrical vessel. The geogrid consists of identical flat biaxial or triaxial geogrids oriented perpendicular to the specimen axis and spaced evenly in the axial direction. The hill material behaves like an unsaturated granular material with spherical or general grain shapes. The geogrid is modeled as a string of spherical balls joined by either parallel bonded or beamed contacts. The parallel bonds or the beamed contacts provide the structural properties of the geogrid. The geogrid validation tests include single rib tensile, aperture stability modulus, and multiple aperture tensile. The simulated laboratory and construction quality assurance material tests include cyclic triaxial compression, dynamic cone penetrometer, and light weight deflectometer.

2.2 DISCUSSION

Initial analyses demonstrated that geogrid provides benefit by increasing the aggregate layer modulus and that the magnitude of this benefit is influenced by moisture content, friction between aggregate particles, and aggregate base layer confinement. The primary structural benefit of adding geogrid to the aggregate base layer is to restrain the aggregate. The resulting increased interlock and friction between the geogrid and the aggregate, and within the aggregate, increase the layer modulus. Under repeated loads, the base layer tends to spread laterally and some of the shear stress in the base layer is transferred to tensile stress in the geogrid. A stiff geogrid will act to restrain the lateral spreading and result in a stiffer aggregate base. The lateral restraint mechanism is well described as "restricting the ability of the aggregate particles to move by effectively fixing them into place via interaction with the geogrid. If particles cannot move, then the modulus of the matrix will be maintained and the rate of accumulation of plastic deformation via shear and consolidation will be reduced" (Bagshaw et al 2015). This mechanism has been investigated and other important knowledge gained using the distinct element method (Konietzky et al 2008, McDowell et al 2006, Qian et al 2015, Stahl and Konietzky, 2011, Tutumluer et al 2012).

For the PFC3D models with geogrid, a single layer of biaxial or triaxial geogrid is centered within the aggregate base. A hill material is created to represent a typical unsaturated aggregate base. The aggregate particles are modeled as spheres, and grain size distributions are chosen within the MnDOT Class 5Q aggregate base grading designation (MnDOT 2018, Tutumluer et al 2015, Xiao and Tutumluer 2012, Xiao et al 2012). During compaction, the simulated aggregate is near saturation, but free draining (moisture surface tension between particles equals zero) while being compacted at a stress between 100 and 200 kPa (Mooney and Rinehart 2009, Rinehart and Mooney 2009). Then moisture surface tension is added between the aggregate particles before performing the cyclic triaxial tests. Axial strains in the PFC3D model correspond with the vertical strains in the aggregate base layer calculated using MnPAVE-Flexible for the expected traffic loads (Tanquist 2012). The confining stresses are similar to those defined by resilient modulus laboratory protocols (NCHRP 1-28A).

2.3 GEOGRID GAIN FACTOR

The benefit of geogrid has been understood in Minnesota (Gale and Marti 2008, Leu and Tasa 2001, Skallman 2010), however MnPAVE-Flexible did not account for the presence of a geogrid within the aggregate base layer. The geogrid gain factor has been introduced as a means to modify the MnPAVE-Flexible design modulus to account for the presence of geogrid within the aggregate base layer (Siekmeier et al 2016). The geogrid gain factor is defined as the ratio of resilient modulus of the aggregate base with geogrid to resilient modulus of the aggregate base without geogrid. The pavement design package is used to estimate the geogrid gain factors for typical geogrid reinforced aggregate roadway configurations. The design modulus of the aggregate base with geogrid can be estimated by multiplying the design modulus of aggregate base without geogrid by the geogrid gain factor. MnPAVE-Flexible can then be used to quantify geogrid's ability to reduce asphalt fatigue and rutting, and thereby estimate the performance of geogrid reinforced flexible pavements. The pavement design package is

being used to estimate geogrid gain factors for typical geogrid reinforced aggregate roadway configurations in which the grain size distribution, initial specimen porosity, material moisture content and confining stress are varied.

During the initial simulation of cyclic triaxial tests, twelve load cycles were performed at axial strains of 0.02% (four cycles), 0.05% (four cycles), and 0.10% (four cycles) to estimate three strain-dependent resilient moduli. The estimated geogrid gain factors for biaxial geogrid resulting from these initial analyses at 0.05% strain are listed in Table 2.1. During the second set of numerical simulations, triaxial geogrid was modeled and example results shown in Tables 2.2 and 2.3. Note that moisture is defined in terms of moisture tension stress based on measurements of typical natural and recycled aggregates in Minnesota (Gupta et al 2007, 2005). These moisture tensions are in the range measured for aggregates at gravimetric moisture contents of about 5 to 10 percent. The (gap 10 mm) notation refers to test cases where moisture tension was extended to aggregate particles separated by a gap of up to 10 mm in order to simulate the inclusion of sand sized particles, which partially fill the gaps between the larger aggregate particles.

Table 2.1 Estimated Geogrid Gain Factors for Biaxial Geogrid

Case	Grain Size (mm)	Porosity	Moisture Tension Stress (kPa)	Confining	Strain (%)	Gain Factor
1	7-38	0.305	10	50	0.05	1.5
				100		1.7
				150		1.8
2	6-50	0.285	20	50	0.05	1.8
				100		2.1
				150		2.3
3	6-50	0.285	20	50	0.05	1.6
				100		1.7
				150		1.8
4	5-50	0.282	20	50	0.05	1.6
				100		1.8
				150		2.0

The dependence of the computed geogrid gain factors upon the system inputs is reasonable. The gain factors for an axial strain of 0.05% increase with increasing confinement, which means that the relative stiffness increase of the geogrid reinforced system is greater than that of the no grid system. An increase of confinement increases interlocking between the geogrid and aggregate, which in turn enhances lateral restraint and results in a stiffer aggregate base.

Table 2.22 Estimated Geogrid Gain Factors for Triaxial Geogrid (Porosity Approximately 0.32)

Case	Particle Roughness Friction Coefficient	Confining Stress	Moisture Tension Stress (gap 10mm)	Resilient Modulus at .1% Strain	Resilient Modulus Gain Factor	Deviator Stress at .1% Strain	Deviator Stress Gain Factor
		(kPa)	(kPa)	(MPa)		(kPa)	
no grid	1.2	25	30	122		43	
grid	1.2	25	30	156	1.28	72	1.70
no grid	1.2	25	60	132		60	
grid	1.2	25	60	194	1.47	103	1.71
no grid	1.2	25	90	136		70	
grid	1.2	25	90	214	1.57	122	1.74
no grid	1.2	50	30	142		57	
grid	1.2	50	30	190	1.34	98	1.71
no grid	1.2	50	60	162		81	
grid	1.2	50	60	222	1.37	131	1.63
no grid	1.2	50	90	166		98	
grid	1.2	50	90	248	1.49	157	1.61

Table 2.33 Estimated Geogrid Gain Factors for Triaxial Geogrid with Stiffer Ribs (Porosity Approximately 0.32)

Case	Particle Roughness Friction Coefficient	Confining Stress	Moisture Tension Stress (gap 10mm)	Resilient Modulus at .1% Strain	Resilient Modulus Gain Factor	Deviator Stress at .1% Strain	Deviator Stress Gain Factor
		(kPa)	(kPa)	(MPa)		(kPa)	
no grid	1.2	25	30	122		45	
grid	1.2	25	30	166	1.36	77	1.71
no grid	1.2	25	60	136		61	
grid	1.2	25	60	206	1.51	111	1.82
no grid	1.2	25	90	140		71	
grid	1.2	25	90	238	1.70	136	1.93
no grid	1.2	50	30	144		59	
grid	1.2	50	30	204	1.42	110	1.86
no grid	1.2	50	60	162		80	
grid	1.2	50	60	244	1.51	148	1.86
no grid	1.2	50	90	174		92	
grid	1.2	50	90	272	1.56	178	1.93

2.4 PARAMETER STUDY

2.4.1 Description

A parameter study was performed to evaluate the sensitivity of the geogrid gain factor to aggregate gradation, particle roughness, moisture content, and confining pressure. After each cyclic triaxial simulation is complete, the dynamic cone penetrometer and light weight deflectometer are simulated at several specified levels of deviator stress and permanent strain. The following section documents the file that calls specific driver files within a predefined folder structure to perform cyclic triaxial test simulations at various confining pressures for both no geogrid simulations and for geogrid reinforced aggregate simulations. This file is provided so that the simulations described in this report can be replicated by others. The enhanced software is now available to all PFC3D users to perform additional simulations and provide greater understanding of the influence of grain size distribution, moisture content, and geogrid depth within the aggregate base layer.

2.4.2 Driver File

```
;fname: MatGen&Test-RUN.p3dvr
set logfile MatGen&Test-RUN.p3log
set log on truncate
new
;
;create grid and no-grid compacted specimens
;
system clone timeout -1 MatGenGridjas.p3prj ...
   call MatGenGridjas.p3dvr
system clone timeout -1 MatGen.p3prj ...
   call MatGen.p3dvr
;
;perform cyclic triaxial tests on grid and no-grid specimens
;
system clone timeout -1 CompTest-DCP_LWD\CompTestGrid.p3prj ...
   call CompTestGrid.p3dvr
system clone timeout -1 CompTest-DCP_LWD\CompTest.p3prj ...
   call CompTest.p3dvr
;
;perform DCP tests on no grid specimens at various moisture conditions and permanent strains
;
system clone timeout -1 CompTest-DCP_LWD\Probe-DCP-s5g1-e.001\Probe.p3prj ...
   call Probe.p3dvr
system clone timeout -1 CompTest-DCP_LWD\Probe-DCP-s5g1-e.002\Probe.p3prj ...
   call Probe.p3dvr
system clone timeout -1 CompTest-DCP_LWD\Probe-DCP-s10g2-e.001\Probe.p3prj ...
   call Probe.p3dvr
;system clone timeout -1 CompTest-DCP_LWD\Probe-DCP-s10g2-e.002\Probe.p3prj ...
```

```
   call Probe.p3dvr
system clone timeout -1 CompTest-DCP_LWD\Probe-DCP-s20g4-e.001\Probe.p3prj ...
   call Probe.p3dvr
system clone timeout -1 CompTest-DCP_LWD\Probe-DCP-s20g4-e.002\Probe.p3prj ...
   call Probe.p3dvr
;
;perform DCP tests on grid specimens at various moisture conditions and permanent strains
;
system clone timeout -1 CompTest-DCP_LWD\Probe-DCP-s5g1-e.001\ProbeGrid.p3prj ...
   call ProbeGrid.p3dvr
system clone timeout -1 CompTest-DCP_LWD\Probe-DCP-s5g1-e.002\ProbeGrid.p3prj ...
   call ProbeGrid.p3dvr
system clone timeout -1 CompTest-DCP_LWD\Probe-DCP-s10g2-e.001\ProbeGrid.p3prj ...
   call ProbeGrid.p3dvr
system clone timeout -1 CompTest-DCP_LWD\Probe-DCP-s10g2-e.002\ProbeGrid.p3prj ...
   call ProbeGrid.p3dvr
system clone timeout -1 CompTest-DCP_LWD\Probe-DCP-s20g4-e.001\ProbeGrid.p3prj ...
   call ProbeGrid.p3dvr
system clone timeout -1 CompTest-DCP_LWD\Probe-DCP-s20g4-e.002\ProbeGrid.p3prj ...
   call ProbeGrid.p3dvr
;
;perform LWD tests on no grid specimens at various moisture conditions and permanent strains
;
system clone timeout -1 CompTest-DCP_LWD\Probe-LWD-s5g1-e.001\Probe.p3prj ...
   call Probe.p3dvr
system clone timeout -1 CompTest-DCP_LWD\Probe-LWD-s5g1-e.002\Probe.p3prj ...
   call Probe.p3dvr
system clone timeout -1 CompTest-DCP_LWD\Probe-LWD-s10g2-e.001\Probe.p3prj ...
   call Probe.p3dvr
system clone timeout -1 CompTest-DCP_LWD\Probe-LWD-s10g2-e.002\Probe.p3prj ...
   call Probe.p3dvr
system clone timeout -1 CompTest-DCP_LWD\Probe-LWD-s20g4-e.001\Probe.p3prj ...
   call Probe.p3dvr
system clone timeout -1 CompTest-DCP_LWD\Probe-LWD-s20g4-e.002\Probe.p3prj ...
   call Probe.p3dvr
;
;perform LWD tests on grid specimens at various moisture conditions and permanent strains
;
system clone timeout -1 CompTest-DCP_LWD\Probe-LWD-s5g1-e.001\ProbeGrid.p3prj ...
   call ProbeGrid.p3dvr
system clone timeout -1 CompTest-DCP_LWD\Probe-LWD-s5g1-e.002\ProbeGrid.p3prj ...
   call ProbeGrid.p3dvr
system clone timeout -1 CompTest-DCP_LWD\Probe-LWD-s10g2-e.001\ProbeGrid.p3prj ...
   call ProbeGrid.p3dvr
system clone timeout -1 CompTest-DCP_LWD\Probe-LWD-s10g2-e.002\ProbeGrid.p3prj ...
   call ProbeGrid.p3dvr
system clone timeout -1 CompTest-DCP_LWD\Probe-LWD-s20g4-e.001\ProbeGrid.p3prj ...
   call ProbeGrid.p3dvr
```

```
system clone timeout -1 CompTest-DCP_LWD\Probe-LWD-s20g4-e.002\ProbeGrid.p3prj ...
   call ProbeGrid.p3dvr
;
set log off
exit
return
;EOF: MatGen&Test-RUN.p3dvr
```

2.5 SUMMARY

The PFC3D pavement design package supports creation and triaxial testing of synthetic unsaturated aggregate base containing geogrid. The geogrid provides lateral restraint to the aggregate base as a result of interlocking and friction between the geogrid and the aggregate particles. The macroscopic system properties are affected by the microstructural system properties. Therefore the modeled system can be used to study and quantify the effect of microstructural properties on the macroscopic properties, which include the stress-strain curves produced during triaxial tests at different confinements. The microstructural properties of the aggregate base include: particle size, particle type (density, Young's modulus, and Poisson's ratio of each particle; and friction between particles), aggregate base moisture content (moisture tension and gap), and initial aggregate base porosity. The PFC3D pavement design package provides a mechanistically defensible model for aggregate-geogrid interaction. The package is being used to improve pavement design methodology in Minnesota by estimating geogrid gain factors for typical geogrid reinforced aggregate roadway configurations in which the particle distribution, initial specimen porosity, moisture content, and confining stress are varied. A simplified geogrid gain factor adjustment is being trialed for MnDOT pavement design on projects where geogrid is being considered (MnPAVE-Flexible Beta 2018).

CHAPTER 3: AGGREGATE CHARACTERIZATION

3.1 INTRODUCTION

The following data input files define the physical characteristics of the aggregate and compaction parameters during the simulations that do not include geogrid as well as simulations the do include geogrid. The compaction parameters are adjusted to achieve nearly equivalent aggregate porosity and density during simulations that include geogrid and simulations that do not include geogrid.

3.2 NUMERICAL SIMULATION

3.2.1 Data Input File Aggregate without Geogrid

The following data input file defines the physical characteristics of the aggregate and sample compaction parameters during the simulations that do not include geogrid. This file is provided so that the simulations described in this report can be replicated by others.

```
;fname: mpParams-C5Q.p3dat
;
; Specify the material properties:
;  common, packing and material groups.
;
;#######################################################
def mpSetCommonParams
; Set common parameters.
 cm_matName = 'C5Q'
; ** Typical aggregate base layer of an asphalt-surface roadway (Class 5Q GSD, no grid).
 cm_matType = 4
 cm_modName = 'hill'
 cm_localDampFac = 0.7
 cm_densityCode = 0
 cm_densityVal = 2650.0

; Grain shape and size distribution group:
  cm_nSD = 4
  cm_typeSD = array.create(cm_nSD)
  cm_ctName = array.create(cm_nSD)
  cm_Dlo = array.create(cm_nSD)
  cm_Dup = array.create(cm_nSD)
  cm_Vfrac = array.create(cm_nSD)
;
; Size distribution #1 and volume fraction (25-38 mm)
  cm_typeSD(1) = 0
  cm_Dlo(1) = 25e-3
  cm_Dup(1) = 38e-3
  cm_Vfrac(1) = 0.40
```

```
;
; Size distribution #2 and volume fraction (19-25 mm)
  cm_typeSD(2) = 0
  cm_Dlo(2) = 19e-3
  cm_Dup(2) = 25e-3
  cm_Vfrac(2) = 0.25
;
; Size distribution #3 and volume fraction (9.5-19 mm)
  cm_typeSD(3) = 0
  cm_Dlo(3) = 9.5e-3
  cm_Dup(3) = 19e-3
  cm_Vfrac(3) = 0.10
;
; Size distribution #4 and volume fraction (5-9.5 mm)
  cm_typeSD(4) = 0
  cm_Dlo(4) = 5e-3
  cm_Dup(4) = 9.5e-3
  cm_Vfrac(4) = 0.25
;
end
@mpSetCommonParams
def mpSetPackingParams
; Set packing parameters.
 pk_Pm = 200.0e3
 pk_procCode = 0
 pk_nc = 0.5;                    porosity of particle cloud prior to packing
 pk_ARatLimit = 1e-3
 ; Boundary-contraction group:
  pk_fricCA = 0.57;              particle friction during packing
  pk_vLimit = 1.0
end
@mpSetPackingParams

;#########################################################
def mpSetUdmParams
; Set hill material parameters.
 ; Common group (set in mpSetCommonParams)
 ; Packing group (set in mpSetPackingParams)
 ; Hill material group:
  hlm_youngMod = 29e9
  hlm_poisRatio = 0.15
  hlm_fricCoef = 0.6;            friction between particles to account for roughness and angularity
  hlm_dampCon = 0.0
  hlm_suction = 0;               suction is applied later prior to testing
end
@mpSetUdmParams
@_mpCheckAllParams
@mpListMicroProps
```

```
return
;EOF: mpParams-C5Q.p3dat
```

3.2.2 Data Input File Aggregate with Geogrid

The following data input file defines the physical characteristics of the aggregate and sample compaction parameters during the simulations that include geogrid. This file is provided so that the simulations described in this report can be replicated by others.

```
;fname: mpParams-C5Q_grid.p3dat
;
; Specify the material properties:
;  common, packing and material groups.
;
;#########################################################
def mpSetCommonParams
; Set common parameters.
 cm_matName = 'C5Q_grid'
; ** Typical aggregate base layer of an asphalt-surface roadway (Class 5Q GSD, grid).
 cm_matType = 4
 cm_modName = 'hill'
 cm_localDampFac = 0.7
 cm_densityCode = 0
 cm_densityVal = 2650.0

; Grain shape and size distribution group:
  cm_nSD = 4
  cm_typeSD = array.create(cm_nSD)
  cm_ctName = array.create(cm_nSD)
  cm_Dlo  = array.create(cm_nSD)
  cm_Dup  = array.create(cm_nSD)
  cm_Vfrac = array.create(cm_nSD)
;
; Size distribution #1 and volume fraction (25-38 mm)
  cm_typeSD(1) = 0
  cm_Dlo(1) = 25e-3
  cm_Dup(1) = 38e-3
  cm_Vfrac(1) = 0.40
;
; Size distribution #2 and volume fraction (19-25 mm)
  cm_typeSD(2) = 0
  cm_Dlo(2) = 19e-3
  cm_Dup(2) = 25e-3
  cm_Vfrac(2) = 0.25
;
; Size distribution #3 and volume fraction (9.5-19 mm)
  cm_typeSD(3) = 0
```

```
  cm_Dlo(3) = 9.5e-3
  cm_Dup(3) = 19e-3
  cm_Vfrac(3) = 0.10
;
; Size distribution #4 and volume fraction (5-9.5 mm)
  cm_typeSD(4) = 0
  cm_Dlo(4) = 5e-3
  cm_Dup(4) = 9.5e-3
  cm_Vfrac(4) = 0.25
;
end
@mpSetCommonParams
def mpSetPackingParams
; Set packing parameters:
 pk_seed = 10001
 pk_Pm = 200.0e3
 pk_procCode = 0
 pk_nc = 0.30;                          porosity of particle cloud prior to packing
 pk_ARatLimit = 1e-3
 ; Boundary-contraction group:
  pk_fricCA = 0.11;                     particle friction during packing
  pk_vLimit = 1.0
end
@mpSetPackingParams

;#########################################################
def mpSetUdmParams
; Set hill material parameters.
 ; Common group (set in mpSetCommonParams)
 ; Packing group (set in mpSetPackingParams)
 ; Hill material group:
  hlm_youngMod = 29e9
  hlm_poisRatio = 0.15
  hlm_fricCoef = 0.6;               friction between particles to account for roughness and angularity
  hlm_dampCon = 0.0
  hlm_suction = 0;                  suction is applied later prior to testing
end
@mpSetUdmParams
@_mpCheckAllParams
@mpListMicroProps
return
;EOF: mpParams-C5Q_grid.p3dat
```

3.3 SUMMARY

The aggregate particles are modeled as spheres with grain size distributions from 5 mm to 38 mm, which are within the MnDOT Class 5Q aggregate base grading designation. During compaction, the simulated aggregate is near saturation, but free draining. Then moisture surface tension is added between the aggregate particles before performing simulations of the cyclic triaxial compression test. The influence of moisture on the stiffness of the aggregate base is described in the next chapter.

CHAPTER 4: MOISTURE CHARACTERIZATION

4.1 EFFECT OF MOISTURE ON THE DESIGN MODULI

One of the features of MnPAVE-Flexible, MnDOT's mechanistic empirical pavement design software (Tanquist, 2012), is consideration of the effect of moisture on the design moduli. Pore suction resistance factors are used to incorporate variably saturated conditions during pavement design. These pore suction resistance factors are based on unsaturated pore suction and the ability of different aggregate bases and soils to draw water into the open pore spaces between the particles. The pore suction resistance factors are important because they are combined with seasonal moisture factors and used to estimate the design moduli for the range of soils and aggregate bases typically used in Minnesota. The current pore suction resistance factors are referenced to the MnROAD test sections, which are constructed on a sandy lean clay subgrade. These moisture factors quantitatively estimate the effect of moisture on the design moduli. The moisture factors are based on the difference between the laboratory percent saturation, near standard Proctor optimum moisture, and the in situ moisture expected beneath Minnesota pavements (Roberson and Siekmeier, 2002, Siekmeier, 2011, Tanquist et al, 2002). Three dimensional distinct element methods are being used to simulate moisture in the pavement system to estimate the effect of moisture suction stress on the stiffness and strength properties in order to improve mechanistic empirical pavement design in Minnesota (Garnica et al 2017).

The aggregate particles are modeled as spheres with grain size distributions from 5 mm to 38 mm, which are within the MnDOT Class 5Q aggregate base grading designation (MnDOT 2018, Tutumluer et al 2015, Xiao and Tutumluer 2012, Xiao et al 2012). A "hill" material has been created as a new option in PFC3D to represent a typical unsaturated aggregate base. During compaction, the simulated aggregate is near saturation, but free draining (moisture surface tension between particles equal to zero) while being compacted at a stress between 100 and 200 kPa (Mooney and Rinehart 2009, Rinehart and Mooney 2009). Then moisture surface tension is added between the aggregate particles at defined separation distances before performing the cyclic triaxial tests. Axial strains in the PFC3D model correspond with the vertical strains in the aggregate base layer calculated using MnPAVE-Flexible for the expected traffic loads (Tanquist 2012). The confining stresses are similar to those defined by resilient modulus laboratory protocols (NCHRP 1-28A).

During the cyclic triaxial tests simulated using the PFC3D distinct element model, twelve load cycles were performed at axial strains of 0.02% (four cycles), 0.05% (four cycles), and 0.10% (four cycles) to estimate three strain-dependent resilient moduli (Figure 4.1).

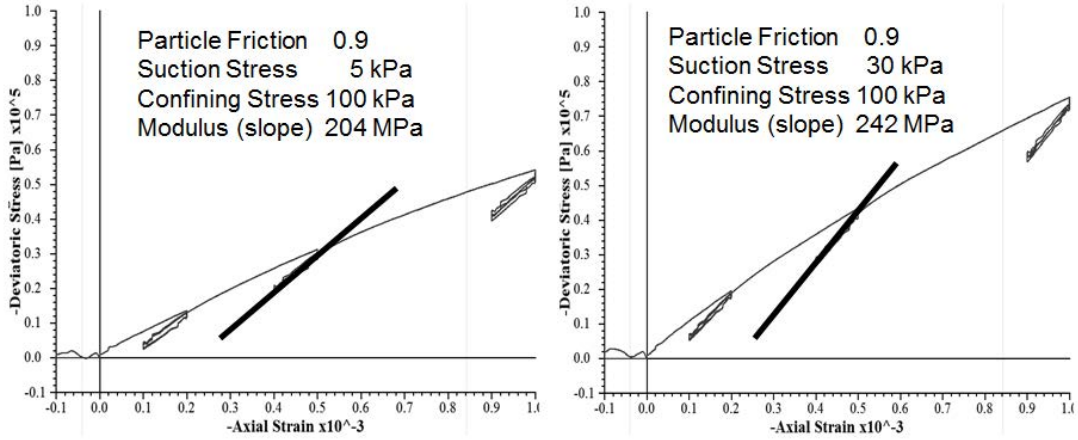

Figure 4.1 Cyclic Triaxial Simulations Showing Increased Modulus with Increased Suction.

4.2 UNSATURATED GAIN FACTOR

As discussed earlier, the geogrid gain factor has been introduced as a means to modify the MnPAVE-Flexible design moduli to account for the presence of geogrid within the aggregate base layer. Similarly, the unsaturated gain factor has been introduced as a means to modify the MnPAVE-Flexible design modulus to account for variable moisture/suction conditions within the aggregate base layer. Please recall that the geogrid gain factor is defined as the ratio of resilient modulus of the aggregate base with geogrid to resilient modulus of the aggregate base without geogrid. Similarly, the unsaturated gain factor is defined as the ratio of resilient modulus of the aggregate base at in situ moisture/suction conditions to resilient modulus of the aggregate base near saturation (very low suction). The PFC3D pavement design package is being used to estimate unsaturated gain factors for typical roadway configurations in which the grain size distribution, initial aggregate base porosity, moisture content and confining stress are varied.

The estimated unsaturated gain factors resulting from these initial analyses at 0.05% strain are listed in Table 4.1 and Table 4.2 for porosities of 0.30 and 0.32 respectively. Please note that moisture is defined in terms of moisture tension stress based on suction measurements of typical natural and recycled aggregates in Minnesota (Gupta et al 2007, 2005). These moisture tensions are in the range measured for aggregates at gravimetric moisture contents of about 5 to 10 percent. The moisture contact gap notation refers to distinct element model test cases where moisture tension was extended to aggregate particles separated by a gap of 1 mm or 10 mm in order to simulate the inclusion of sand sized particles, which partially fill the gaps between the larger aggregate particles in the in situ aggregate layer being simulated. Sand sized particles (less than 5 mm) are not currently included in the distinct element model due to computer processor speed limitations.

Table 4.1 Estimated Unsaturated Material Gain Factors (Porosity Approximately 0.30)

Case	Particle Roughness Friction	Moisture Contact Gap (mm)	Moisture Tension Stress (kPa)	Resilient Modulus .05% Strain (MPa)	Resilient Modulus Gain Factor	Deviator Stress .05% Strain (kPa)	Deviator Stress Gain Factor
1	0.9	1	1	120	1	26	1
2	0.9	1	5	140	1.17	32	1.23
3	0.9	1	30	172	1.43	45	1.74
4	0.9	1	60	190	1.58	56	2.18
5	0.9	10	1	118	1	25	1
6	0.9	10	5	140	1.19	33	1.32
7	0.9	10	30	182	1.54	55	2.19
8	0.9	10	60	206	1.75	69	2.73
9	1.2	1	1	122	1	29	1
10	1.2	1	5	142	1.16	35	1.21
11	1.2	1	30	172	1.41	49	1.69
12	1.2	1	60	190	1.56	60	2.06
13	1.2	10	1	124	1	29	1
14	1.2	10	5	142	1.15	37	1.29
15	1.2	10	30	182	1.47	58	2.03
16	1.2	10	60	208	1.68	70	2.46

Table 4.22 Estimated Unsaturated Material Gain Factors (Porosity Approximately 0.32)

Case	Particle Roughness Friction	Moisture Contact Gap (mm)	Moisture Tension Stress (kPa)	Resilient Modulus .05% Strain (MPa)	Resilient Modulus Gain Factor	Deviator Stress .05% Strain (kPa)	Deviator Stress Gain Factor
1	0.9	1	1	82	1	14	1
2	0.9	1	5	96	1.17	16	1.18
3	0.9	1	30	120	1.46	25	1.86
4	0.9	1	60	134	1.63	35	2.57
5	0.9	10	1	76	1	12	1
6	0.9	10	5	100	1.32	18	1.54
7	0.9	10	30	132	1.74	33	2.77
8	0.9	10	60	138	1.82	37	3.13
9	1.2	1	1	82	1	16	1
10	1.2	1	5	102	1.24	20	1.29
11	1.2	1	30	120	1.46	29	1.82
12	1.2	1	60	134	1.63	37	2.34
13	1.2	10	1	82	1	14	1
14	1.2	10	5	100	1.22	19	1.42
15	1.2	10	30	124	1.51	33	2.39
16	1.2	10	60	132	1.61	40	2.93

4.3 PARAMETER STUDY

4.3.1 Description

A parameter study was performed to evaluate the sensitivity of the unsaturated gain factor to aggregate gradation, particle roughness, moisture content, and aggregate separation distance. The following file calls specific files within a predefined folder structure to perform cyclic triaxial test simulations at various moisture contents (suction and separation distance). This file is provided so that the simulations described in this report can be replicated by others.

4.3.2 Driver File

```
;fname: CompTest.p3dvr
;
; IN: ctParams.p3dat
;    Saved State (with corresponding model title):
;    <cm_matName>-matV : specimen in material vessel
; OUT: CompTest.p3log
;    Saved States (with corresponding model titles):
;     <cm_matName>-ctN : end of loading stage N (N = 0,1,2,...)
;                                  (loading stage 0 is seating phase)
set logfile CompTest.p3log
set log    on truncate
set echo  on

;############################################################

;Test material at first moisture content. Restore compacted specimen, adjust moisture content, and
then perform cyclic triaxial compression tests.
restore ..\C5Q-matV.p3sav

;Add 5 kPa suction between aggregate particles within 1 mm of one another.
[cm_matName = cm_matName + '_suc5kPa_gap1mm']
@hlm_makeWet( 5.0e3, 1.0e-3 )

call ..\..\fistSrc\ct.fis   suppress
call ctParams.p3dat    suppress

@msOff
@ctSeatingPhase
@ft_ZeroGrainDisplacement
@ctLoadingPhase

;############################################################

;Test material at second moisture content. Restore compacted specimen, adjust moisture content, and
```

```
then perform cyclic triaxial compression tests.
restore ..\C5Q-matV.p3sav

;Add 10 kPa suction between aggregate particles within 2 mm of one another.
[cm_matName = cm_matName + '_suc10kPa_gap2mm']
@hlm_makeWet( 10.0e3, 2.0e-3 )

call ..\..\fistSrc\ct.fis   suppress
call ctParams.p3dat    suppress

@msOff
@ctSeatingPhase
@ft_ZeroGrainDisplacement
@ctLoadingPhase

;#########################################################

;Test material at third moisture content. Restore compacted specimen, adjust moisture content, and
then perform cyclic triaxial compression tests.
restore ..\C5Q-matV.p3sav

;Add 20 kPa suction between aggregate particles within 4 mm of one another.
[cm_matName = cm_matName + '_suc20kPa_gap4mm']
@hlm_makeWet( 20.0e3, 4.0e-3 )

call ..\..\fistSrc\ct.fis   suppress
call ctParams.p3dat    suppress

@msOff
@ctSeatingPhase
@ft_ZeroGrainDisplacement
@ctLoadingPhase

;#########################################################
set log off
gui project save
exit
return
;EOF: CompTest.p3dvr
```

4.4 SUMMARY

The dependence of the computed unsaturated gain factors upon the system inputs is reasonable. All gain factors are greater than one, which confirms that the suction is increasing the stiffness and strength. Additional simulations are being performed to help interpret these initial results as well as provide greater understanding of the influence of grain size distribution, moisture content, and porosity of the aggregate base layer. The PFC3D pavement design package supports creation and triaxial testing

of synthetic unsaturated aggregate base and can be used to study and quantify the effect of microstructural properties on the macroscopic properties, which include the stress-strain curves produced during cyclic triaxial compression tests at different moisture contents. The enhanced software is now available to all PFC3D users to perform additional simulations and provide greater understanding of the influence of moisture content on aggregate base layers.

CHAPTER 5: DYNAMIC CONE PENETROMETER SIMULATIONS

5.1 DESCRIPTION OF THE DEVICE

MnDOT implemented an aggregate base construction quality assurance specification for the DCP in 1998. The DCP's falling mass drops from a specified height and drives the pointed cone into the pavement foundation material. The DCP penetration distance per drop is known as the DCP penetration index (DPI), which is used to estimate the shear strength of pavement foundation materials using empirical relationships. The original DCP specification implemented by MnDOT was intended to be used for aggregate base. That specification was later modified to account for gradation and moisture effects in order to increase its accuracy and expand its applications to other granular materials. Both the grading number and moisture content have a strong influence on the DPI, and therefore target DPI values are determined according the grading number and moisture content (Oman 2004).

The DCP is shown in figure 5.1 and consists of two vertical shafts connected at the anvil (ASTM D 6951-03). The upper shaft is used to provide a standard drop height of 575 mm for the hammer as well as a handle to hold the DCP vertical. The hammer is 8 kg and provides a constant impact force. The lower shaft has an anvil at the top and a pointed cone on the bottom. During operation, the hammer is dropped, hits the anvil, and drives the cone into the ground.

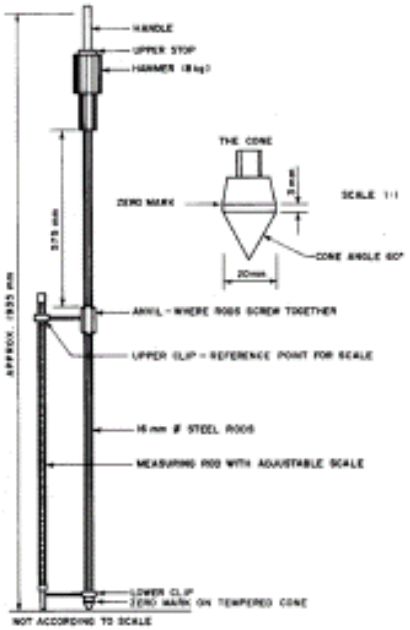

Figure 5.1 Dynamic Cone Penetrometer.

There are a few options available for the DCP, which include hammer mass, cone style and angle, and recording method. The standard hammer mass is 8 kg and there is also a 4.6 kg alternative. For pavement applications, the 8 kg mass is used due to the highly compacted materials. The DCP cone can be either replaceable or disposable. The replaceable cone stays on the DCP until damaged or worn

beyond a defined tolerance and then replaced. The disposable cone remains in the ground after every test, making it easier to remove the DCP lower shaft from the ground. A new disposable cone must be placed on the DCP before the next test. Manual or automated methods are available to gather penetration measurements. An automated ruler allows for a single operator instead of two and electronically records the data, making it more practical to record the penetration for each hammer drop and transfer the data.

5.2 DCP TEST PROCEDURE

The DCP test procedure is currently standardized by both ASTM D 6951-03 and the MnDOT Grading and Base Manual. The following is a brief description of the test procedure as described in Siekmeier et al 2009. First, the DCP should be inspected for fatigue, damaged parts, and that all connections are securely tightened. The operator holds the device vertical by the handle on the top shaft. A second person records the height at the bottom of the anvil in reference to the ground. The operator lifts the hammer from the anvil to the handle and then releases the hammer. The second person records the new height at the bottom of the anvil. In general, this process is repeated until twelve drops are preformed, two for the seating, five for the first DPI calculation, and another five for the second DPI calculation. Small penetrations represent better compaction. Because the material close to the surface is less confined by overlying material, the DCP typically measures greater resistance to penetration and greater strength at greater depths when the pavement foundation material is well compacted.

5.3 NUMERICAL SIMULATION OF DCP

5.3.1 Description

The following data input file defines the physical characteristics of the DCP and its dynamic properties (Chua and Lytton 1988, Nazarian et al 2000, Tan et al 2014, Yohannes et al 2009). This file is provided so that the simulations described in this report can be replicated by others.

5.3.2 Data Input File

```
;fname: dlParams.p3dat
; ** Dynamic cone penetrometer probe.
def dlSetParams
; Set DCP & LWD probe parameters:
 dl_probeType = 0;                0 selects DCP as the probe type
; Geometry group:
  dcp_coneAng = 60.0;             MnDOT standard is 60 degree cone tip angle
  dcp_coneBaseDiam = 20e-3;       MnDOT standard is 2 cm cone base diameter
  dcp_rodDiam = 16e-3;            MnDOT standard is 1.6 cm rod diameter
  dcp_rodLen = 240e-3;            rod length of 24 cm used in simulation
  dcp_nc = 8
  dcp_nr = 48
  dcp_Dt = 4e-3
```

```
; Material properties group:
  dl_massTot = 13.0
  dl_massHam = 8.0
  dl_semod = 1e9
  dl_skrat = 2.0
  dl_sfric = 0.6
; Boundary conditions group:
  dl_BCcode = 0
  dl_BCPaTop = 0.0;          vertical stress in pascals applied to aggregate surface
  dl_BCPl = 5e3;          horizontal stress in pascals during all hammer drops (0 or 5 kPa)
  dl_fPen = 25e-3;          forced penetration depth in meters prior to first hammer drop (25 mm)
  dl_fPenRate = 2.0;          penetration rate in meters per second
  dl_localDampFac = 0.08;          originally 0.02
  dl_hillDampCon = 0.28;          originally 0.07
  dl_grav = 9.81
  dl_plRad = 0.0
  dl_plAng = 0.0
  dl_conLat = 0
  dl_Fh = 105e3;          peak force in newtons (105 kN, Tan et al 2014)
;                          (35 kN, Chua and Lytton 1988) (80 kN, Nazarian et al 2000)
  dl_th = 0.1e-3;          duration of force pulse in seconds (Tan et al 2014)
  dl_nh = 1000;          originally 2000
  dl_nhi = 300;          originally 10
; Servo-control group:
  dl_ARatLimit = 3e-2;          originally 2e-5
  dl_stepLimit = 500000
end
@dlSetParams
@_dlCheckParams
@dlListProps
; Specify histories to be monitored during the test.
 history add id=600 fish dl_eTime;      elapsed time since rod or plate creation
 history add id=601 fish dl_pen;      rod or plate penetration
 history add id=602 fish dl_penV;      rod or plate penetration velocity
 history add id=603 fish dl_rF;      resisting force from material
 history add id=604 fish dl_aF;      externally applied force acting on rod or plate
 history add id=605 fish dl_PaTop;      axial pressure acting on top wall
 history add id=606 fish dl_Pl;      lateral pressure acting on side walls
return
```

5.4 RESULTS OF NUMERICAL SIMULATIONS

Figure 5.2 is an example of the simulation results and shows DCP penetration for four successive hammer drops. The top three plots are for cases without geogrid and moisture decreasing from left to right. The bottom three plots are for cases that include geogrid at the same moisture as the top cases. . These plots show that the DCP penetration is reduced in the geogrid reinforced aggregate simulations

compared to the cases that are not reinforced. This reduction in penetration is reflected in the performance specification described in Chapter 7.

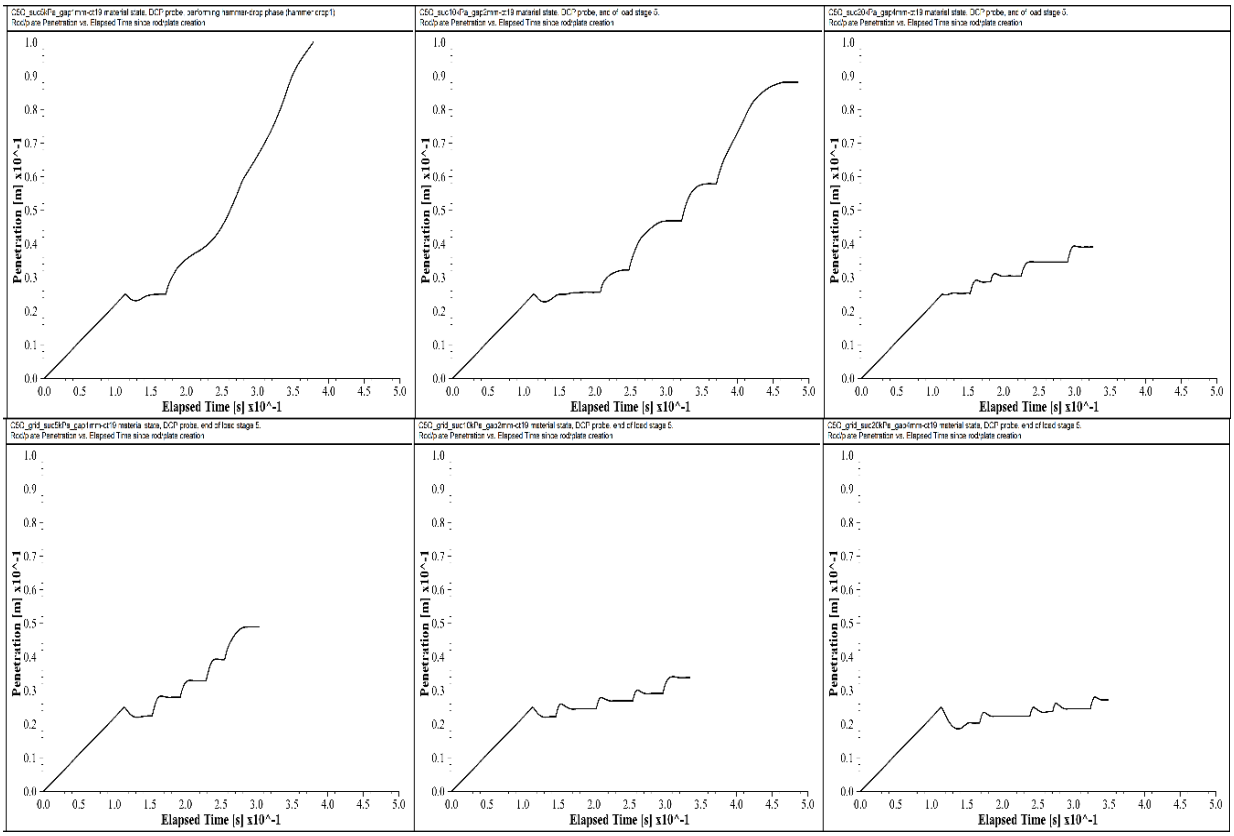

Figure 5.22 DCP Penetration per Hammer Drop.

CHAPTER 6: LIGHT WEIGHT DEFLECTOMETER SIMULATIONS

6.1 DESCRIPTION OF THE DEVICE

The light weight deflectometer (LWD) (ASTM E 2583-07 and ASTM E2835-11), consists of a mass (typically 10 kg), an accelerometer or geophone, and a data collection unit. LWDs are designed to be light enough to be moved and operated by one person. LWDs are often used for quality assurance of unbound material compaction in parts of Europe (Fleming et al., 2007), and are beginning to be used in the United States (Indiana DOT 2018, Mooney et al 2008, Petersen and Hartman 2010, Siekmeier et al 2009, Steinert et al 2005, and White et al 2007, 2009).

MnDOT purchased several dozen LWDs and has distributed some of these LWDs to local agencies and other state DOTs (LRRB 2018 and NRRA 2018). An important issue that has arisen during the implementation of LWD technology is whether or not it is necessary to measure, or if it is acceptable to estimate, the load generated by the falling weight. Load estimation is not necessary for all LWD models because some include a load cell that measures the load as a function of time during impact (ASTM E 2583-07). Other LWDs use one fixed peak load estimate, which is determined during trial testing in the laboratory (ASTM E2835-11).

LWD quality assurance offers several advantages over the specified density method. On a practical level, LWD tests take less time, have greater precision, and are able to accurately test more material types (Indiana DOT 2018). For example, large aggregate creates problems for other tests. In addition, LWD testing is safer because the construction inspector is able to remain standing and visible during most of the testing process (Davich et al 2006).

Seven LWD models have been used in Minnesota and there are a variety of differences between these devices. The following is a general description of common characteristics of the LWD. From top to bottom, the handle is used to keep the shaft vertical. Next along the shaft is a release trigger, which holds the mass in place prior to dropping ensuring a standard drop height, which provides the impact force. Buffers, which are either rubber pads or steel springs, catch the falling mass and transfer the force to the loading plate. At the bottom is the loading plate, which must be in full contact with the pavement foundation material to be tested, and a sensor used for deflection measurement. An LWD can have a fixed drop height or have an adjustable drop height. Some LWDs measure deflection using an accelerometer fixed inside the load plate, while other LWDs use a geophone that passes through a hole on the bottom of the plate to directly contact the surface. Some LWDs assume a peak load established during trial testing, while others include a load cell. Finally, the buffer and plate stiffness affect how the energy of the falling mass is transferred to the ground (Mooney and Miller 2009, Vennapusa and White 2009).

6.2 LWD PROCEDURE

LWD devices are configured and used differently depending on the model and testing agency. ASTM has published a national standard for LWDs with load cells (ASTM E2583-07) and a national standard for LWDs without load cells (ASTM E2835-11). In the case of E2835 LWDs, the applied force from the falling mass is measured at the factory and used for all future modulus calculations for that particular LWD. Other LWDs include a load cell to measure the load and then combine this load with the deflection to estimate the modulus for each drop. Previous studies have found that E2583 moduli were about 1.75 times greater than E2835 moduli when the drop height, mass, and plate size were constant (White et al 2007).

A previous study completed by MnDOT recommended standardizing the LWD mass at 10 kg, the drop height at 50 cm, and the plate diameter at 20 cm for ease of use and in order to have an appropriate influence depth to test one lift of compacted pavement foundation material (Davich et al., 2006). Plate size affects the measurement depth, confinement, and stress level applied to stress dependent materials. Standardizing the LWD plate size to 20 cm reduces these variables and allows the target deflection to be estimated. Because the buffer type affects the force delivered to the ground, MnDOT specifies that a force of 6.28 kN be delivered to the ground. This equates to a stress of 0.2 MPa for a 20 cm diameter plate. LWD tests in Minnesota are currently conducted using that configuration, along with the following test guidelines and advice contained in the manufacturer's literature (Siekmeier et al 2009).

The surface is leveled prior to placing the LWD on the material to be tested. Three seating drops are performed prior to data collection to ensure that plastic deformation of the surface material does not affect the measurements. Once the LWD has been seated, data collection should consist of three measurement drops. The three values resulting from these measurement drops are averaged to create one mean value for that test location. The operator will often notice that the modulus values increase slightly during the three measurement drops from a fixed height. If this increase exceeds 5 percent, it is probable that the material has not been adequately compacted. Reliable measurement values cannot be obtained until the material has been adequately compacted.

LWD devices should not be used when the temperature falls below 5 degrees Celsius to ensure that the device's components, particularly the rubber buffers, work as intended. There is no practical upper limit on the temperature. While most LWDs will work in the rain, it should be noted that moisture greatly affects the strength and stiffness characteristics of the unbound pavement foundation materials. It is necessary to measure the moisture content for every test using an in situ moisture testing device or by removing a sample for an oven dry test.

It is important that the layer structure be considered because deeper layers within the pavement foundation can affect LWD measurements even though the primary depth of influence is approximately one to 1.5 plate diameters. Analysis methods and testing specifications have been developed to account for layer effects and moisture content to estimate target values (Indiana DOT 2018, Nazarian et al 2014, Schwartz et al 2017, Steinert et al 2005, and Tirado et al 2017).

6.3 NUMERICAL SIMULATION OF LWD

6.3.1 Description

The following data input file defines the physical characteristics of the LWD and its dynamic properties. This file is provided so that the simulations described in this report can be replicated by others.

6.3.2 Data Input File

```
;fname: dlParams.p3dat
; ** Lightweight Deflectometer probe.
def dlSetParams
; Set DCP & LWD Probe Parameters:
 dl_probeType = 1;              1 selects LWD as the probe type
; Geometry group:
  lwd_plateDiam = 150e-3;       MnDOT standard is 20 cm plate diameter
  lwd_nr = 3
; Material properties group:
  dl_massTot = 30.0;            ZFG 3000-200 30kg (10+5+15)
  dl_massHam = 10.0;            ZFG 3000-200 10kg
  dl_semod = 1e9
  dl_skrat = 2.0
  dl_sfric = 0.6
; Boundary conditions group:
  dl_BCcode = 0
  dl_BCPaTop = 0.0;             vertical stress in pascals applied to aggregate surface
  dl_BCPl = 5.0e3;              horizontal stress in pascals during all hammer drops (0 or 5 kPa)
  dl_fPen = 0.0;                allow LWD to settle under self-weight before first hammer drop
  dl_fPenRate = 0.0
  dl_localDampFac = 0.08;       originally 0.02
  dl_hillDampCon = 0.28;        originally 0.07
  dl_grav = 9.81
  dl_plRad = 0.0
  dl_plAng = 0.0
  dl_conLat = 0
  dl_Fh = 3.53e3;               modified force = 3.53 kN for a 15 cm diameter plate (200 kPa)
;                               MnDOT standard force = 6.28 kN for a 20 cm diameter plate (200 kPa)
  dl_th = 15.5e-3;              duration of force pulse in seconds ZFG 3000-200 (15.5ms)
  dl_nh = 500;                  originally 2000
  dl_nhi = 3;                   originally 10
; Servo-control group:
  dl_ARatLimit = 3e-2;          originally 2e-5
  dl_stepLimit = 500000
end
@dlSetParams
@_dlCheckParams
```

```
@dlListProps
; Specify histories to be monitored during the test.
 history add id=600 fish dl_eTime;      elapsed time since rod/plate creation
 history add id=601 fish dl_pen;        rod or plate penetration
 history add id=602 fish dl_penV;       rod or plate penetration velocity
 history add id=603 fish dl_rF;         resisting force from material
 history add id=604 fish dl_aF;         externally applied force acting on rod or plate
 history add id=605 fish dl_PaTop;      axial pressure acting on top wall
 history add id=606 fish dl_Pl;         lateral pressure acting on side walls
return
;EOF: dlParams.p3dat
```

6.4 RESULTS OF NUMERICAL SIMULATIONS

Figure 6.1 is an example of the simulation results and shows LWD plate displacement for four successive hammer drops. The top three plots are for cases that no not include geogrid and have moisture decreasing from left to right. The bottom three plots are for cases that include geogrid at the same moisture as the top cases. These plots show that the plate displacement is reduced in the geogrid reinforced aggregate simulations compared to the cases that are not reinforced. It is also interesting to note that the plate displacement is more elastic for the geogrid reinforced aggregate simulations compared to the cases that are not reinforced. The geogrid is providing a mechanistically quantified benefit and it is well understood that better long term pavement performance occurs when the underlying pavement layers behave elastically. This reduction in displacement is reflected in the performance specification described in Chapter 7.

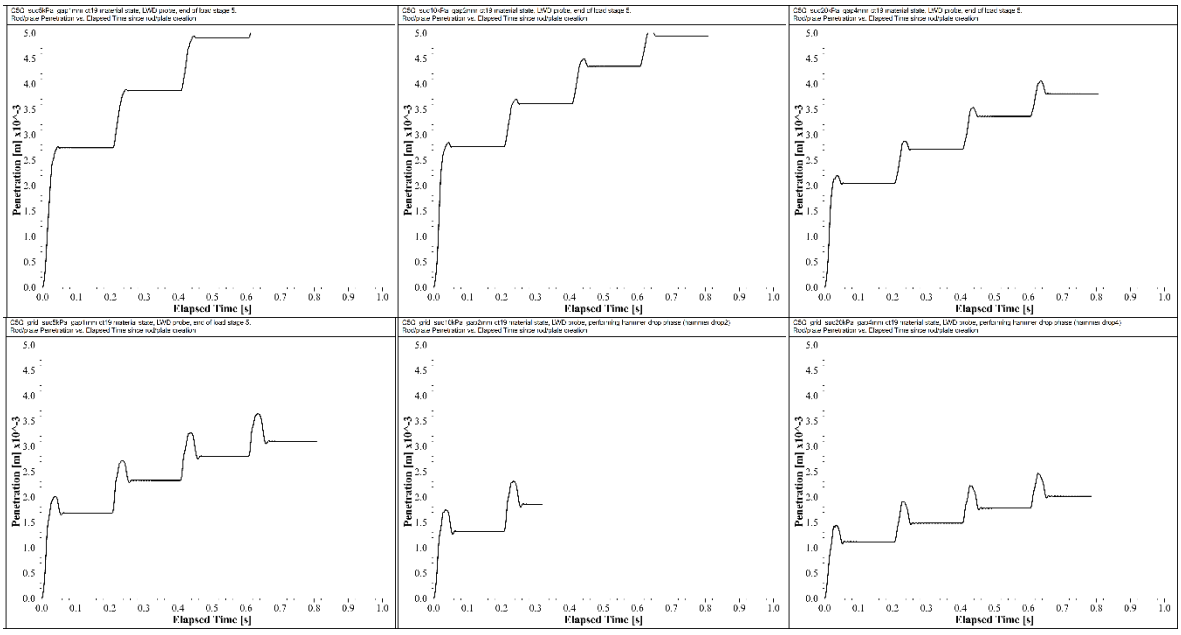

Figure 6.11 LWD Penetration per Hammer Drop.

CHAPTER 7: PERFORMANCE BASED SPECIFICATION

The procedure for using the dynamic cone penetrometer (DCP) and light weight deflectometer (LWD) to test aggregate base reinforced with geogrid is similar to testing unreinforced aggregate base. The test location is selected to accurately represent the constructed aggregate base layer and the DCP or LWD is placed at the appropriately prepared test location. For both the DCP and LWD, the weight is raised and released to deliver a predetermined number of drops.

The DCP is used to estimate the aggregate base strength by measuring the penetration of the lower shaft into the aggregate base. The DCP device is described in the MnDOT Grading and Base Manual and ASTM D6951 "Standard Test Method for Use of the Dynamic Cone Penetrometer in Shallow Pavement Applications." The strength of geogrid reinforced aggregate base has been measured using the DCP (Wayne, Kwon and White 2014).

The LWD is used to estimate the aggregate base stiffness by measuring the displacement of the plate that rests on the surface of the aggregate base. The LWD device is described in the MnDOT Grading and Base Manual, ASTM E2835 "Standard Test Method for Measuring Deflections using a Portable Impulse Plate Load Test Device" and ASTM E2583-07, "Standard Test Method for Measuring Deflections with a Light Weight Deflectometer." The stiffness of geogrid reinforced aggregate base has been measured using the LWD (Bagshaw 2016).

When using the DCP, drop the weight two times to seat the DCP tip into the surface of the aggregate base and record the penetration measurement to the nearest mm. Then drop the weight ten more times and record the penetration measurement to the nearest mm. Finally, drop the weight three more times and record the penetration measurement to the nearest mm. Note that the total number of drops is fifteen. The DCP penetration index (DPI) is reported in millimeters per drop for both the ten-drop increment and the final three-drop increment. The DPI target value (DPI-TV) is the maximum allowable penetration per drop and is measured in mm per drop.

When using the LWD, drop the weight three times to assure good contact between the plate and the surface of the aggregate base. These first three seating drops are not recorded. The LWD measurement value (LWD-MV) is the average plate displacement calculated using the fourth, fifth, and sixth drops recorded to the nearest 1/100th mm. LWD Target Value (LWD-TV) is the maximum allowable plate displacement and is measured to the nearest 1/100th mm.

Compact the geogrid reinforced aggregate base to achieve the target values in the following table. Note that the grading number and moisture content must be known in order to determine the appropriate target value. The DCP and LWD target values in the following table are for specific DCP and LWD models because different models may use different weights and sensors. The target values in the following table apply to the DCP and LWD described in the MnDOT Grading and Base Manual.

Table 7.1 DCP and LWD Target Values for Geogrid Reinforced Aggregate Base

Grading Number	Moisture Content	DPI-TV with Geogrid			LWD-TV with Geogrid
GN	%	mm / drop	mm / 10 drops	mm / 3 drops	mm
3.1-3.5	5 - 7	7	65	20	0.33
	7 - 9	8	79	24	0.40
	9 - 11	11	108	32	0.53
3.6-4.0	5 - 7	7	65	20	0.33
	7 - 9	10	101	30	0.50
	9 - 11	13	129	39	0.63
4.1-4.5	5 - 7	9	86	26	0.43
	7 - 9	11	115	34	0.57
	9 - 11	14	144	43	0.70

Note: LWD-TV calculated using Poisson Ratio = 0.5, Plate Rigidity = 1.0, and Peak Force = 6.28 kN (Peak Stress = 200 kPa for 200 mm diameter plate.)

CHAPTER 8: CONCLUSIONS

A performance specification has been developed for geogrid reinforced aggregate base, which utilizes the dynamic cone penetrometer (DCP) and light weight deflectometer (LWD) to test the aggregate base reinforced with geogrid. These quality assurance devices, in particular the DCP, are very familiar to construction inspection staff in Minnesota, and therefore this performance specification is expected to be readily implemented. In summary, the construction quality assurance test locations are selected to accurately represent the constructed aggregate base layer and the DCP or LWD is placed at the appropriately prepared test location. For both the DCP and LWD, the weight is raised and released to deliver a predetermined number of drops that result in a measured penetration (DCP-MV) or plate displacement (LWD-MV), which is then compared to a predetermined target value (DCP-TV or LWD-TV).

These construction quality assurance target values are based on the required pavement foundation strength and stiffness determined during design. MnDOT's flexible pavement design method, MnPAVE-Flexible, links the design inputs to these construction measurements and estimates pavement life. MnPAVE-Flexible has been enhanced using the pavement design package added to the PFC3D distinct element software to support creation and cyclic triaxial compression testing of an unsaturated aggregate base containing geogrid. The geogrid provides lateral restraint to the aggregate base as a result of interlocking and friction between the geogrid and the aggregate particles. The macroscopic system properties are affected by the microstructural properties. Therefore, the modeled system can be used to study and quantify the effect of the microstructural properties on the macroscopic system such as the stress-strain relationship produced during cyclic triaxial tests at different confining stresses. The macrostructural properties specific to the geogrid include aperture shape and structural stiffness. The microstructural properties of the geogrid include rib dimensions, rib stiffness, and rib surface friction. The microstructural properties of the aggregate base include particle size, particle type (density, Young's modulus, Poisson's ratio, and surface friction), moisture content (tensile stress and separation distance), and initial aggregate base porosity.

The pavement design package provides a mechanistically defensible model for aggregate-geogrid interaction. The package is being used to improve pavement design methodology in Minnesota by estimating geogrid gain factors and unsaturated gain factors for typical roadway configurations in which the aggregate size distribution, initial porosity, moisture content, and confining stress are varied. A simplified geogrid gain factor adjustment is being trialed for MnDOT pavement design on projects where geogrid is being considered (MnPAVE-Flexible Beta 2018). The current work builds on previous studies and specifically addresses the benefits of geogrid reinforced aggregate base at lower strains by applying the distinct element method to better understand the aggregate-geogrid interaction. In addition, the importance of moisture is quantified mechanistically by applying suction (tensile stress) between aggregate particles at defined separation distances.

REFERENCES

Al-Qadi, I., S. Dessouky, J. Kwon, and E. Tutumluer. (2012). Geogrid-Reinforced Low-Volume Flexible Pavements: Pavement Response and Geogrid Optimal Location, Journal of Transportation Engineering, 139(9):1083-1090, American Society of Civil Engineers, Washington, D.C.

ASTM D6951-09. (2015). Standard Test Method for Use of the Dynamic Cone Penetrometer in Shallow Pavement Applications, ASTM International, West Conshohocken, Pennsylvania.

ASTM E2583-07. (2007). Standard Test Method for Measuring Deflections with a Light Weight Deflectometer, ASTM International, West Conshohocken, Pennsylvania.

ASTM E2835-11. (2011). Standard Test Method for Measuring Deflections using a Portable Impulse Plate Load Test Device, ASTM International, West Conshohocken, Pennsylvania.

Bagshaw, S. (2016). Basecourse Modulus Improvement by Inclusion of Geogrid, Contract Report 521231, Opus International Consultants, New Zealand.

Bagshaw, S., P. Herrington, P. Kathirgamanathan, and S. Cook. (2015). Geosynthetics in Basecourse Reinforcement, Research Report 574, New Zealand Transport Agency, Wellington, New Zealand.

Casanova, J. and J. Siekmeier. (2013). Trunk Highway 72 Geogrid Analysis, Office of Materials and Road Research, Minnesota Department of Transportation, Saint Paul, Minnesota.

Chua, K. and R. Lytton. (1988). Dynamic Analysis Using the Portable Pavement Cone Penetrometer, Transportation Research Record 1192, Transportation Research Board of the National Academics, Washington, D.C.

Clyne, T. (2011). Monitoring Geosynthetics in Local Roadways (LRRB 768) 10-Year Performance Summary, MnDOT 2011-20, Minnesota Department of Transportation, Saint Paul, Minnesota.

Cundall, P. and O. Strack. (1979). A Discrete Numerical Model for Granular Assemblies, Geotechnique, 29(1):47-55.

Davich, P., F. Camargo, B. Larsen, R. Roberson, and J. Siekmeier. (2006). Validation of DCP and LWD Moisture Specifications for Granular Materials, MnDOT 2006-20, Minnesota Department of Transportation, Saint Paul, Minnesota.

Edil, T., J. Tinjum, and C. Benson. (2012). Recycled Unbound Materials, MnDOT 2012-35, Minnesota Department of Transportation, Saint Paul, Minnesota.

ELMOD. (2012). Evaluation of Layer Moduli and Overlay Design, Dynatest International, Glastrup, Denmark.

Erickson, H. and A. Drescher. (2001). Use of Geosynthetics to Reinforce Low Volume Roads, MnDOT 2001-15, Minnesota Department of Transportation, Saint Paul, Minnesota.

Fleming, P., M. Frost, and J. Lambert. (2007). Review of Lightweight Deflectometer for Routine In Situ Assessment of Pavement Material Stiffness, Transportation Research Record 2004, Transportation Research Board of the National Academics, Washington, D.C.

Gale, S. and M. Marti. (2008). Putting Research into Practice: Training Module for Designing and Constructing with Geosynthetics, MnDOT Technical Summary PP07GEO-TS, Minnesota Department of Transportation, Saint Paul, Minnesota.

Garcia-Rojo, R., S. McNamara, and H. Herrmann. (2008). Influence of Contact Modeling on the Macroscopic Plastic Response of Granular Soils under Cyclic Loading, Mathematical Models of Granular Matter, 1937:109-123, Springer, Berlin, Germany.

Garnica, P., N. Perez, J. Siekmeier, R. Roberson, and B. Tanquist. (2018). State of the Practice in Mexico and Minnesota to Estimate the Effect of Water Content and Suction in Subgrade Soils and Granular Materials, PanAm-UNSAT 2017, Geotechnical Special Publication, American Society of Civil Engineers, Washington D.C.

Grading and Base Manual. (2015). Office of Materials and Road Research, Minnesota Department of Transportation, Saint Paul, Minnesota.

Gupta, S., and W. Larson. (1979). Estimating Soil Water Retention Characteristics from Particle Size Distribution, Organic Matter Percent, and Bulk Density, Water Resources Research, 15:1633-1635.

Gupta, S., A. Ranaivoson, T. Edil, C. Benson, and A. Sawangsuriya. (2007). Pavement Design Using Unsaturated Soil Technology, MnDOT 2007-11, Minnesota Department of Transportation, Saint Paul, Minnesota.

Gupta, S., A. Singh, and A. Ranaivoson. (2005). Moisture Retention Characteristics of Base and Sub-base Materials, MnDOT 2005-06, Minnesota Department of Transportation, Saint Paul, Minnesota.

Hart, D. and P. Cundall. (1992). Microcomputer Programs for Explicit Numerical Analysis in Geotechnical Engineering, International Seminar on Numerical Methods in Geomechanics, Moscow, Russia.

Indiana 508-12T. (2018). Field Determination of Deflection using Light Weight Deflectometer, Indiana Department of Transportation Office of Materials Management, Indianapolis, Indiana.

Indiana 509-15P. (2015). Field Determination of Strength using Dynamic Cone Penetrometer, Indiana Department of Transportation Office of Materials Management, Indianapolis, Indiana.

Itasca Consulting Group, Inc. (2015). PFC3D 5.0, Particle Flow Code, Itasca Consulting Group, Inc., Minneapolis, Minnesota.

Jas, H., M. Stahl, H. Konietzky, L. teKamp, and T. Oliver. (2015). Discrete Element Modeling of a Trafficked Sub-Base Stabilized with Biaxial and Multi-Axial Geogrids to Compare Stabilization Mechanisms, Geosynthetics, Portland, Oregon.

Konietky, H., L. teKamp, T. Groeger, and C. Jenner. (2004). Use of DEM to Model the Interlocking Effect of Geogrids Under Static and Cyclic Loading, Numerical Modeling in Micromechanics via Particle Methods, Taylor and Francis, London, England.

Konietzky, H., J. Kwon, and E. Tutumluer. (2008). Aggregate Base Residual Stresses Affecting Geogrid Reinforced Flexible Pavement Response, International Journal of Pavement Engineering, 9(4):275-285.

Lekarp, F., U. Isacsson, and A. Dawson. (2000). State of the Art. I: Resilient Response of Unbound Aggregates, Journal of Transportation Engineering, 126(1):66-75.

Lekarp, F., U. Isacsson, and A. Dawson. (2000). State of the Art. II: Permanent Strain Response of Unbound Aggregates, Journal of Transportation Engineering, 126(1):76-83.

Lemos, J. (2011). Recent Developments and Future Trends in Distinct Element Methods UDEC/3DEC and PFC Codes, 10th International Conference Discontinuous Deformation Analysis, Hawaii.

Leu, W. and L. Tasa. (2001). Applications of Geotextiles, Geogrids, and Geocells in Northern Minnesota, Geosynthetics Conference, Portland, Oregon.

LRRB. (2018). Local Road Research Board. Retrieved August 1, 2018 from https://lrrb.org.

Luo, R., F. Gu, X. Luo, R. Lytton, E. Hajj, R. Siddharthan, S. Elfass, M. Piratheepan, and S. Pournoman. (2017). Quantifying the Influence of Geosynthetics on Pavement Performance, National Cooperative Highway Research Program, Transportation Research Board of the National Academics, Washington, D.C.

McDowell, G., O. Harireche, H. Konietzky, S. Brown, and N. Tho. (2006). Discrete Element Modeling of Geogrid-Reinforced Aggregates, Geotechnical Engineering, 1(159):35-48.

McDowell, G. M. and Lu. (2006). The Importance of Modelling Ballast Particle Shape in the Discrete Element Method, Granular Matter, doi: 10.1007/s10035-006-0021-3.

MnDOT Grading and Base Manual. (2018). Minnesota Department of Transportation, Saint Paul, Minnesota.

MnDOT Standard Specification for Construction. (2018). Minnesota Department of Transportation, Saint Paul, Minnesota.

MnPAVE-Flexible Beta. (2018). Minnesota Department of Transportation, Saint Paul, Minnesota.

Mooney, M., C. Nocks, K. Selden, G. Bee, and C. Senseney. (2009). Improving Quality Assurance of MSE Wall and Bridge Approach Earthwork Compaction, Report No. CDOT-2008-11, Colorado Department of Transportation, Denver, Colorado.

Mooney, M. and P. Miller. (2009). Analysis of Light Weight Deflectometer Test Based on In Situ Stress and Strain Response, Journal of Geotechnical and Geoenvironmental Engineering, 135(2):199-208, American Society of Civil Engineers, Washington, D.C.

Mooney, M. and R. Rinehart. (2009). In Situ Soil Response to Vibratory Loading and its Relationship to Roller Measured Soil Stiffness, Journal of Geotechnical and Geoenvironmental Engineering, 135(8):1022-1031, American Society of Civil Engineers, Washington, D.C.

Nazarian, S., M. Mazari, I. Abdallah, A. Puppala, L. Mohammad, and M. Abu-Farsakh. (2014). Modulus-Based Construction Specification for Compaction of Earthwork and Unbound Aggregate, National Cooperative Highway Research Program, Transportation Research Board of the National Academics, Washington, D.C.

Nazarian, S., V. Tandon, K. Crain, and D. Yuan. (2000). Use of Instrumented Dynamic Cone Penetrometer in Pavement Characterization, ASTM STP 1375, American Society for Testing and Materials, West Conshohocken, Pennsylvania.

Nazzal, M. (2007). Laboratory Characterization and Numerical Modeling of Geogrid Reinforced Bases in Flexible Pavements, PhD Thesis, Department of Civil and Environmental Engineering, Louisiana State University.

NCHRP. (2003). Harmonized Test Methods for Laboratory Determination of Resilient Modulus for Flexible Pavement Design, National Cooperative Highway Research Program, Transportation Research Board, Washington, D.C.

Ng, T. and R. Dobry. (1992). A Numerical Simulation of Monotonic and Cyclic Loading of Granular Soil, Journal of Geotechnical Engineering, 120(2):388-403.

NRRA. (2018). National Road Research Alliance. Retrieved August 1, 2018 from https://www.dot.state.mn.us/mnroad/nrra/index.html.

Oman, M, (2004) Advancement of Grading and Base Material Testing, Office of Materials and Road Research, Minnesota Department of Transportation, Maplewood, Minnesota.

Oman, M. (2013). Pavement Deflection Testing and Analysis, MnDOT Contract 03375, Braun Intertec Corporation, Saint Paul, Minnesota.

Ovik, J., B. Birgisson, and D. Newcomb. (2000). Characterizing Seasonal Variations in Pavement Material Properties for Use in a Mechanistic Empirical Design Procedure, MnDOT 2000-35, Minnesota Department of Transportation, Saint Paul, Minnesota.

Perkins, S. and M. Ismeik. (1997). A Synthesis and Evaluation of Geosynthetic-Reinforced Base Layers in Flexible Pavements: Part I, Geosynthetics International, 4(6):549-605.

Perkins, S. and M. Ismeik. (1997). A Synthesis and Evaluation of Geosynthetic-Reinforced Base Layers in flexible Pavements: Part II, Geosynthetics International, 4(6):605-621.

Petersen, L. and M. Hartman. (2010). 2008 MnROAD Unbound Quality Control Construction Report, MnDOT 2010-32, Minnesota Department of Transportation, Saint Paul, Minnesota.

Potyondy, D. (2018a). Pavement-Design Package for PFC3D [pdPkg14], Itasca Consulting Group, Inc., Technical Memorandum ICG16-8528-15TM (June 22, 2018), Minneapolis, Minnesota.

Potyondy, D. (2018b). Model-Validation Tests, Itasca Consulting Group, Inc., Technical Memorandum 2-3558-01:17TM52 (June 22, 2018), Minneapolis, Minnesota.

Potyondy, D. (2018c). Beam Contact Model [version 1], Itasca Consulting Group, Inc., Technical Memorandum 2-3558-01:17TM07 (June 22, 2018), Minneapolis, Minnesota.

Potyondy, D. (2016a). Pavement Design Package for PFC3D, Technical Memorandum ICG16-8528-15TM, Itasca Consulting Group, Minneapolis, MN.

Potyondy, D. (2016b). Hill Contact Model, Technical Memorandum ICG7795-L, Itasca Consulting Group, Minneapolis, MN.

Potyondy, D. (2015). The Bonded-Particle Model as a Tool for Rock Mechanics Research and Application: Current Trends and Future Directions, Geosystem Engineering, 18(1):1–28.

Potyondy, D., J. Siekmeier, and L. Petersen. (2016). Aggregate-Geogrid Interaction Model Incorporating Moisture Effects, Proceedings, Transportation Research Board Annual Meeting, Washington, D.C.

Potyondy, D. and P. Cundall. (2004). A Bonded Particle Model for Rock, International Journal of Rock Mechanics and Mining Sciences, 41(8):1329-1364, Elsevier.

Qian, Y., D. Mishra, E. Tutumluer, and H. Kazmee. (2015). Characterization of Geogrid Reinforced Ballast Behavior at Different Levels of Degradation through Triaxial Shear Strength Test and Discrete Element Modeling, Geotextiles and Geomembranes, 43(5):393-402.

Qian Y., D. Mishra, E. Tutumluer, and J. Kwon. (2013). Comparative Evaluation of Different Aperture Geogrids for Ballast Reinforcement through Triaxial Testing and Discrete Element Modeling, Proceedings, Geosynthetics 2013, Long Beach, California.

Rinehart, R. and M. Mooney. (2009). Measurement Depth of Vibratory Roller Measured Soil Stiffness, Geotechnique, 59(7):609-619.

Roberson, R. and Siekmeier, J. (2002). Determining Material Moisture Characteristics for Pavement Drainage and Mechanistic Empirical Design, Research Bulletin 2002 M&RR 09, Minnesota Department of Transportation, Saint Paul, Minnesota.

Schwartz, C., Z. Afsharikia, and S. Khosravifar. (2017). Standardizing Lightweight Deflectometer Modulus Measurements for Compaction Quality Assurance, MD-17-SHA/UM/3-20, Maryland Department of Transportation State Highway Administration, Baltimore, Maryland.

Siekmeier, J. and K. O'Connor. (1993). Modeling Overburden Response to Longwall Mining, First International Symposium on Numerical Modeling Applications in Mining and Geotechniques, Montreal, Quebec, Canada.

Siekmeier, J., J. Bittmann, D. Potyondy, and L. Petersen. (2016). Introducing a Geogrid Gain Factor for Flexible Pavement Design, Proceedings, 64th Annual Geotechnical Conference, University of Minnesota, Minneapolis, Minnesota.

Siekmeier, J. and J. Casanova. (2016). Geogrid Reinforced Aggregate Base Stiffness for Mechanistic Pavement Design, MnDOT 2016-24, Minnesota Department of Transportation, Saint Paul, Minnesota.

Siekmeier, J. (2011). Unsaturated Soil Mechanics Implementation during Pavement Construction Quality Assurance, Proceedings, 59th Annual Geotechnical Conference, University of Minnesota, Minneapolis, Minnesota.

Siekmeier, J., C. Pinta, S. Merth, J. Jensen, P. Davich, F. Camargo, and M. Beyer. (2009). Using the Dynamic Cone Penetrometer and Light Weight Deflectometer for Construction Quality Assurance, MnDOT 2009-12, Minnesota Department of Transportation, Saint Paul, Minnesota.

Skallman, J. (2010). Geogrids on CSAH and MSAS Routes General Specification, Granular Equivalent and Design Guidelines, Technical Memorandum 10-SA-03, Minnesota Department of Transportation, Saint Paul, Minnesota.

Skok, E., E. Johnson, and M. Brown. (2003). Special Practices for Design and Construction of Subgrades in Poor, Wet and/or Saturated Soil Conditions, MnDOT 2003-39, Minnesota Department of Transportation, Saint Paul, Minnesota.

Skok, E., D. Timm, M. Brown, T. Clyne, and E. Johnson. (2003). Best Practices for the Design and Construction of Low Volume Roads, MnDOT 2002-17REV, Minnesota Department of Transportation, Saint Paul, Minnesota.

Stahl, M., H. Konietzky, L. teKamp, and H. Jas. (2013). Discrete Element Simulation of Geogrid-Stabilized Soil, Acta Geotechnica., doi: 10.1007/s11440-013-0265-0.

Stahl, M. and H. Konietzky. (2010). Discrete Element Simulation of Ballast and Gravel under Special Consideration of Grain-Shape, Grain-Size, and Relative Density, Granular Matter, 13(4):417-428.

Starfield, A. and P. Cundall. (1988). Towards a Methodology for Rock Mechanics Modeling, International Journal of Rock Mechanics and Mining Sciences, 25(3):99-106.

Steinert, B., D. Humphrey, and M. Kestler. (2005). Portable Falling Weight Deflectometer Study, New England Transportation Consortium, University of Connecticut, Storrs, Connecticut.

Tan, D., K. Hill, and L. Khazanovich. (2014). Quantifying Moisture Effects in DCP and LWD Tests Using Unsaturated Mechanics, MnDOT 2014-13, Minnesota Department of Transportation, Saint Paul, Minnesota.

Tanquist, B. (2012). MnPAVE User's Guide, Office of Materials and Road Research, Minnesota Department of Transportation, Saint Paul, Minnesota.

Tanquist, B., S. Dai, P. Davich, J. Siekmeier, and D. VanDeusen. (2002). Pavement Designer's Guide MnDOT Flexible Pavement Design MnPAVE Beta Version 5.1, Office of Materials and Road Research, Minnesota Department of Transportation, Saint Paul, Minnesota.

Tirado, C., K. Gamez-Rios, A. Fathi, M. Mazari, and S. Nazarian. (2017). Simulation of Lightweight Deflectometer Measurements Considering Nonlinear Behavior of Geomaterials, Transportation Research Record 2641, Transportation Research Board of the National Academics, Washington, D.C.

Tutumluer, E., Y. Xiao, and W. Wilde. (2015). Cost Effective Base Type and Thickness for Long Life Concrete Pavements, MnDOT 2015-42, Minnesota Department of Transportation, Saint Paul, Minnesota.

Tutumluer, E., Y. Qian, Y. Hashash, J. Ghaboussi, and D. Davis. (2013). Discrete Element Modelling of Ballasted Track Deformation Behavior, International Journal of Rail Transportation, 1(1-2):57-73.

Tutumluer, E., H. Huang and X. Bian. (2012). Geogrid Aggregate Interlock Mechanism Investigated through Aggregate Imaging Based Discrete Element Modeling Approach, International Journal Of Geomechanics, 12(4):391-398, American Society of Civil Engineers, Washington, D.C.

Van Cauwelaert, F., D. Alexander, T. White, and W. Barker. (1989). Multilayer Elastic Program for Backcalculating Layer Moduli in Pavement Evaluation (WESLEA), Nondestructive Testing of Pavements and Backcalculation of Moduli, ASTM STP1026, American Society for Testing and Materials, West Conshohocken, Pennsylvania.

Vennapusa, P and D. White. (2009). Comparison of Light Weight Deflectometer Measurements for Pavement Foundation Materials, Geotechnical Testing Journal, 32(3), American Society for Testing and Materials, West Conshohocken, Pennsylvania.

Wayne, M., J. Kwon, and D. White. (2014). Assessment of Pavement Foundation Stiffness using Cyclic Plate Load Test, German Geotechnical Society, Berlin, Germany.

White, D., M. Thompson, and P. Vennapusa. (2007). Field Validation of Intelligent Compaction Monitoring Technology for Unbound Materials, MnDOT 2007-10, Minnesota Department of Transportation, Saint Paul, Minnesota.

White, D. and P. Vennapusa. (2017). MnROAD Unbound Layer Evaluation using Intelligent Compaction: Ingios Validated Intelligent Compaction Results, Report to the National Road Research Alliance, Ingios Geotechniques.

White, D. and P. Vennapusa. (2016). Automated Plate Load Testing Report: TH72 Geogrid Reinforced Base and Control Test Sections, Report to the Minnesota Department of Transportation, Ingios Geotechniques.

White, D., P. Vennapusa, J. Zhang, and H. Gieselman. (2009). Implementation of Intelligent Compaction Performance Based Specifications in Minnesota, MnDOT 2009-14, Minnesota Department of Transportation, Saint Paul, Minnesota.

Xiao, Y. (2014). Performance Based Evaluation of Unbound Aggregates Affecting Mechanistic Response and Performance of Flexible Pavements, PhD Dissertation, University of Illinois, Urbana-Champaign, Illinois.

Xiao, Y., E. Tutumluer, Y. Qian, and J. Siekmeier. (2012). Gradation Effects Influencing Mechanical Properties of Aggregate Base and Granular Subbase Materials in Minnesota, Transportation Research Record 2267, Transportation Research Board of the National Academics, Washington, D.C.

Xiao, Y., E. Tutumluer, and J. Siekmeier. (2011). Mechanistic Empirical Evaluation Aggregate Base and Granular Subbase Quality Affecting Flexible Pavement Performance in Minnesota, Transportation Research Record 2227, Transportation Research Board of the National Academics, Washington, D.C.

Xiao, Y. and E. Tutumluer. (2012). Best Value Granular Material for Road Foundations, MnDOT 2012-01, Minnesota Department of Transportation, Saint Paul, Minnesota.

Yohannes, B., K. Hill, and L. Khazanovich. (2009). Mechanistic Modeling of Unbound Granular Materials, MnDOT 2009-21, Minnesota Department of Transportation, Saint Paul, Minnesota.

Zeghal, M., (2005). Discrete Element Method Investigation of the Resilient Behavior of Granular Materials, Journal of Transportation Engineering, 130(10):503-509.

APPENDIX A:
INTRODUCTION TO PFC PAVEMENT DESIGN

Introduction to PFC Pavement Design

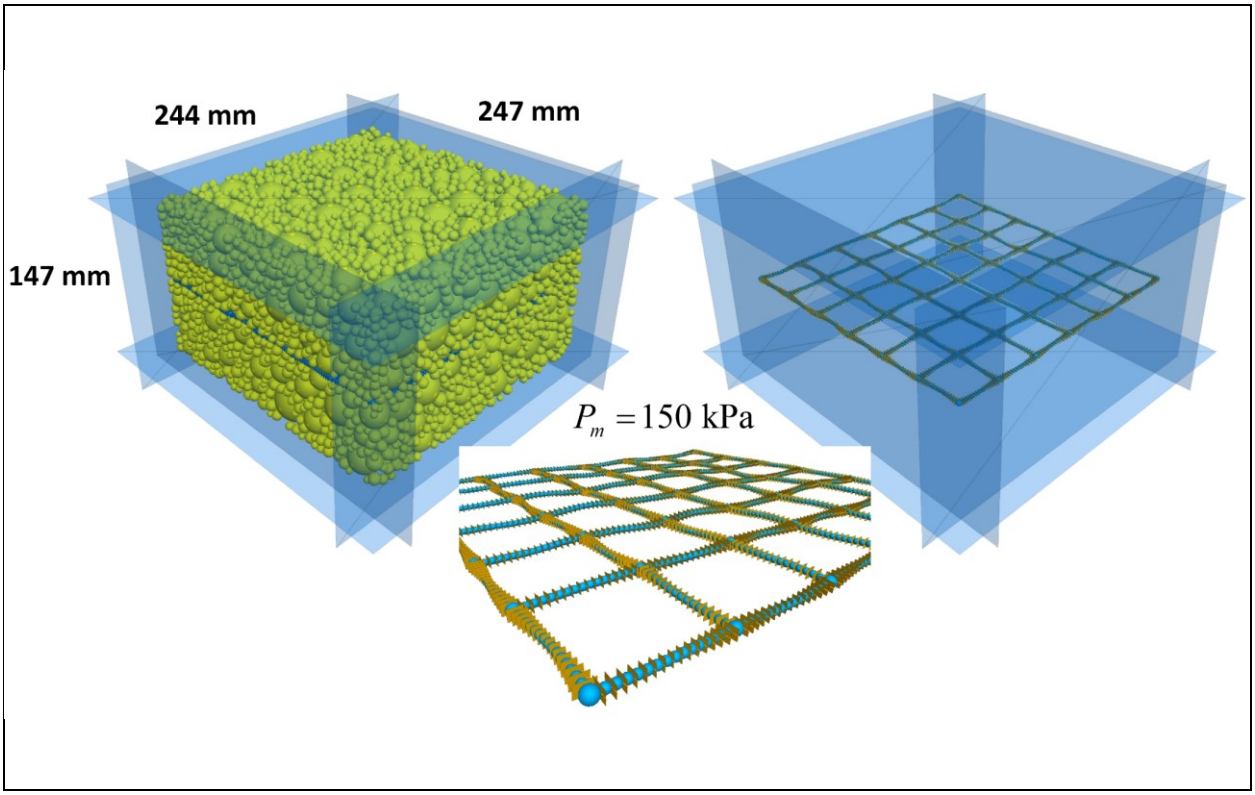

June 22, 2018
2-3558-01:18R14

Prepared For:
John Siekmeier
MN Dept. of Transportation
Prepared By:
David Potyondy

ITASCA
Consulting Group, Inc.

111 Third Ave South, Suite 450
Minneapolis, MN 55401
phone: 1 612 371-4711 fax: 1 612 371-4711
email: icg@itascacg.com
web: www.itascacg.com

Itasca Consulting Group (Itasca) has developed a pavement-design package for the Minnesota Department of Transportation (MnDOT). The package has been developed in two phases. The work performed during the first phase is summarized in Potyondy (2015). This report summarizes the work performed during the second phase, which is part of the MnDOT project "Geogrid Specification for Aggregate Base Reinforcement." The entire body of work is described in Potyondy (2018a, 2018b, and 2018c).

The pavement-design package (Potyondy, 2018a) for the *Particle Flow Code in Three Dimensions* (*PFC3D*, Itasca [2018]) supports creation of a hill material (Potyondy, 2016) in which biaxial and triaxial geogrids may be embedded, testing of the grids to obtain their macroscopic properties, and testing of the material. The material and grid set are created in either a polyaxial or cylindrical vessel. The grid set consists of identical flat biaxial or triaxial geogrids oriented perpendicular to the specimen axis and spaced evenly in the axial direction. The hill material behaves like an unsaturated granular material, with spherical and general grain shapes via clumps (collections of overlapping spherical pebbles). The grid is modeled as a string of spherical balls joined by either parallel-bonded or beamed contacts. The parallel bonds or the beamed contacts provide the structural properties of the grid, and the spherical balls provide the surface for grid-object interaction. The grid tests include: Single Rib Tensile (SRT), Aperture Stability Modulus (ASM), and Multiple Aperture Tensile (MAT). The material tests include: triaxial, Dynamic Cone Penetrometer (DCP), and Light Weight Deflectometer (LWD).

The following tasks were completed during the second phase of work.

1. The geogrid representation has been extended to allow different geogrid types to be modeled by creating a *PFC3D* beam contact model (see Potyondy [2018c] for model description and verification problem). A string of spherical balls for which the beam contact model exists at all ball-ball contacts is called a pebbled beam (P-beam). A P-beam provides the structural behavior of a prismatic and bisymmetrical beam composed of isotropic, linear elastic material. The P-beam is defined by the dimensions of its rectangular cross-section (which may vary along the beam length), and the Young's modulus and Poisson's ratio. The P-beam matches the response (within 3%) of a tip-loaded cantilever beam subjected to axial, flexural, and twisting deformations.
2. Grid generation has been enhanced to provide biaxial and triaxial beamed grids in addition to existing biaxial parallel-bonded grids (Potyondy, 2018a). Each grid rib behaves either as an elastic beam of circular cross-section with varying radius along its length (parallel-bonded contacts) or as a prismatic and bisymmetrical elastic beam with varying width and height along its length (beamed contacts). The biaxial beamed grid has been calibrated to match SRT and ASM tests on Tensar SS20 geogrid. The triaxial beamed grid has been calibrated to match SRT and ASM tests on Tensar TX160 geogrid.
3. Grid tensile stiffness can now be measured by performing a Multiple Aperture Tensile test on the biaxial and triaxial grids (Potyondy, 2018a).
4. The material-genesis procedure has been extended to include general grain shapes in which grains are modeled as clumps, which are collections of overlapping spherical

pebbles that behave as rigid bodies (Potyondy, 2017). An example of a material with non-spherical grains is given in Potyondy (2018b, Figure 5).

5. A typical roadway model has been created, and various instances of this model are used to demonstrate the general modulus-porosity-grid-grain shape relation (Potyondy, 2018b).
6. The capability to perform Dynamic Cone Penetrometer (DCP) and Light Weight Deflectometer (LWD) tests on the synthetic material, both with and without grid, has been developed (Potyondy, 2018b).

The pavement-design package is being used to improve pavement-design methodology in Minnesota by estimating geogrid gain factors (defined as the ratio of resilient modulus of the aggregate base with geogrid to resilient modulus of the aggregate base without geogrid) for typical geogrid-reinforced aggregate roadway configurations in which grain-size distribution, initial specimen porosity, moisture content, and confining stress are varied (Potyondy et al., 2016; Siekmeier et al., 2016; Siekmeier and Casanova, 2016). The package is also being used to study the effect of geogrid inclusion on resilient modulus of railway ballast (Mahmud et al., 2018).

The behavior of the synthetic material during large-strain triaxial tests (up to 10% strain) was not investigated during the second phase of work, because typical geogrid-reinforced aggregate roadway configurations experience only small-deformation loading; however, *PFC3D* modeling of railway ballast by Mahmud (2017) suggests that matching the triaxial shear strength (maximum deviator stress that can be sustained by the material) requires polyhedral grains, because clumps are not sufficiently angular. Further study of this issue is warranted.

References

Itasca Consulting Group, Inc. (2018) *PFC — Particle Flow Code in 2 and 3 Dimensions*, Version 5.0, Documentation Set of version 5.00.35 [March 21, 2018]. Minneapolis: Itasca.

Mahmud, S.M.N. (2017) ***Effect of Particle Size Distribution and Packing Characteristics on Railroad Ballast Shear Strength: A Numerical Study using the Discrete Element Method***, M.S. Thesis, Boise State University.

Mahmud, S.M.N., D. Mishra, and D.O. Potyondy (2018) "Effect of Geogrid Inclusion on Ballast Resilient Modulus: The Concept of Geogrid Gain Factor," in ***Proceedings, 2018 Joint Rail Conference (JRC 2018, Pittsburgh, April 2018)***, paper JRC2018-6126.

Potyondy, D. (2018a) "Pavement-Design Package for *PFC3D* [pdPkg14]," Itasca Consulting Group, Inc., Technical Memorandum ICG16-8528-15TM (June 22, 2018), Minneapolis, Minnesota.

Potyondy, D. (2018b) "Model-Validation Tests," Itasca Consulting Group, Inc., Technical Memorandum 2-3558-01:17TM52 (June 22, 2018), Minneapolis, Minnesota.

Potyondy, D. (2018c) “Beam Contact Model [version 1],” Itasca Consulting Group, Inc., Technical Memorandum 2-3558-01:17TM07 (June 22, 2018), Minneapolis, Minnesota.

Potyondy, D. (2017) “Material-Modeling Support in *PFC* [fistPkg25],” Itasca Consulting Group, Inc., Technical Memorandum ICG7766-L (March 16, 2017), Minneapolis, MN.

Potyondy, D. (2016) “Hill Contact Model [version 4],” Itasca Consulting Group, Inc., Technical Memorandum ICG7795-L (October 12, 2016), Minneapolis, MN.

Potyondy, D. (2015) “PFC Pavement Design,” Itasca Consulting Group, Inc., Report to Minnesota Department of Transportation (MnDOT) Office of Materials, Maplewood, MN, ICG15-2845-42, July 21, 2015.

Potyondy, D., J. Siekmeier and L. Petersen. (2016) “Aggregate-Geogrid Interaction Model Incorporating Moisture Effects,” in ***Proceedings, Transportation Research Board 2016 Annual Meeting (Washington, D.C., January 2016)***, 16–6085. Washington, D.C.: National Academy of Sciences.

Siekmeier, J., J. Bittmann, D. Potyondy and L. Petersen. (2016) “Introducing a Geogrid Gain Factor for Flexible Pavement Design,” in ***Proceedings, University of Minnesota 64th Annual Geotechnical Engineering Conference (Minneapolis, March 2016)***, J. F. Labuz and A. B. Carney, Eds. Minneapolis: University of Minnesota.

Siekmeier, J., and J. Casanova. (2016) “Geogrid Reinforced Aggregate Base Stiffness for Mechanistic Pavement Design,” Saint Paul, Minnesota, Minnesota Department of Transportation Research Report 2016-24, MN/RC 2016-24, July 2016.

APPENDIX B:
PAVEMENT DESIGN PACKAGE

Technical Memorandum

ITASCA
Consulting Group, Inc.

Date: June 22, 2018

To: PFC 5 Documentation Set

From: David Potyondy

Re: Pavement-Design Package for PFC3D [pdPkg14]

Ref: ICG16-8528-15TM

This memo describes the pavement-design package for the Particle Flow Code in 3 Dimensions (*PFC3D*, Itasca [2018]).[1] The package supports creation and triaxial testing of a synthetic unsaturated granular material containing geogrid (see Figure 3).[2] The geogrid provides lateral restraint to the granular material as a result of interlocking and friction between the geogrid and the granular material, and this is believed to be the primary structural benefit of adding geogrid to the aggregate base layer of a pavement structure. The package can be used to study and quantify the effect of microstructural properties on macroscopic response, which includes the stress-strain curves produced during triaxial tests. The microstructural properties of the granular material include: grain size distribution of spherical or clumped grains, grain material type, moisture content and initial specimen porosity. The microstructural properties of the geogrid include: geometry, structural stiffness and grid-surface behavior. The package is being used to improve pavement-design methodology in Minnesota by estimating geogrid gain factors (defined as the ratio of resilient modulus of the aggregate base with geogrid to resilient modulus of the aggregate base without geogrid) for typical geogrid-reinforced aggregate roadway configurations in which the grain-size distribution, initial specimen porosity, moisture content and confining stress are varied (Potyondy et al., 2016; Siekmeier et al., 2016; Siekmeier and Casanova, 2016). The package could be extended to investigate the behavior of other aggregate-geogrid systems such as a geogrid pull-out or wheel-load test.

[1] The pavement-design package is provided in the form of a consistent set of FISH functions that operate within *PFC3D* version 5.0. FISH is a programming language embedded within *PFC3D*. The *PFC3D* code can be obtained from http://www.itascacg.com/pfc, and the pavement-design package can be obtained from http://www.itascacg.com/pavement-design-package.

[2] The package also supports Dynamic Cone Penetrometer (DCP) and Light Weight Deflectometer (LWD) tests on the synthetic material (Potyondy, 2018a).

Pavement-design methodology is summarized in the first major section. The pavement-design package is described in the second major section, with an emphasis on the geogrid-modeling methodology. Pavement-design examples are given in the third major section. A typical aggregate base layer of an asphalt-surface roadway is modeled. The resilient modulus is measured, for dry and wet conditions both with and without a geogrid, by performing triaxial tests on the modeled systems.

TABLE OF CONTENTS

1.0 PAVEMENT-DESIGN METHODOLOGY

The first subsection outlines the layered elastic analysis that is used to support pavement design via *MnPAVE* (Tanquist, 2012). The second subsection introduces the geogrid gain factor as a means to modify the *MnPAVE* design modulus to account for the presence of geogrid within the aggregate base layer. And the final subsection discusses the unsaturated condition of pavement materials.

1.1 Layered Elastic Analysis

The mechanistic-empirical flexible pavement design program *MnPAVE* embodies an accepted procedure for the design of flexible pavements in Minnesota. *MnPAVE* simulates traffic loads on a pavement using a layered elastic analysis (LEA). The LEA is an axisymmetric, isotropic, elastic-layer model with bottom and sides at infinity, wheel load at the top, parameterized by thickness, Young's modulus and Poisson's ratio for each of the five layers, and allowing full to zero slip interface conditions. *MnPAVE* enforces the zero-slip condition to compute normal and shear stress, normal strain and displacement within the system shown in Figure 1. Of particular importance is the horizontal tensile strain at the bottom of the asphalt layer (ε_h), and the vertical compressive strain at the top of the compacted soil layer (ε_v). An excessive value of ε_h can result in a fatigue crack forming and continuing upwards to the pavement surface, and an excessive vertical stress associated with ε_v can result in permanent deformation in the compacted soil layer, which over time will be visible at the pavement surface as rutting. Estimates of fatigue and rutting life are obtained via empirical relations that employ these quantities (ε_h for fatigue and ε_v for rutting). Both life estimates must be greater than twenty years for the design to be acceptable. The inputs to *MnPAVE* include the thickness and material type of each layer, climate and traffic. The parameters are tied to one another via empirical relations. For example, life predictions require integrating the damage effects of wheel loading over time, and the climate dictates moisture conditions, which affect the elastic constants.

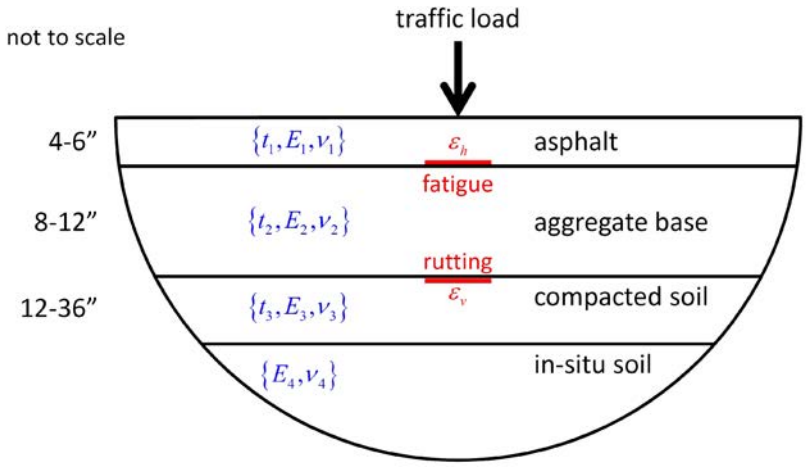

Figure 1 ***Layered elastic analysis showing inputs (blue), typical layer names and thicknesses, and outputs (red) used to estimate fatigue and rutting life of flexible pavements.***

Traffic loading in pavement analysis is conventionally simplified as a cyclic deviator stress (σ_d). The repeated application of the deviator stress results in permanent strain (ε_p) and resilient strain (ε_r) within pavement materials, as shown in Figure 2. The resilient modulus (M_R) is defined as the ratio of applied deviator stress to recoverable or "resilient" strain. It is a granular material characterization parameter that is stress dependent. The resilient modulus is used as the design modulus for the layered elastic analysis shown in Figure 1. LEA is utilized extensively for pavement system evaluation and is a means of calculating pavement response under loading. Each pavement layer is defined by its resilient modulus and Poisson's ratio, even though granular bases exhibit nonlinear elastoplastic behavior in laboratory and field applications. LEA is used because it is a relatively simple analysis procedure and, more importantly, pavement loading is generally of low enough magnitude that a linear-elastic approximation of pavement material behavior is deemed suitable. According to Han and Vanapalli (2016), the resilient modulus is "…the key soil property in the mechanistic pavement design methods to rationally characterize the resilient behavior of the pavement materials, analyze the fatigue failure of the surface layer, and dimension the multi-layer system of the pavement structure."

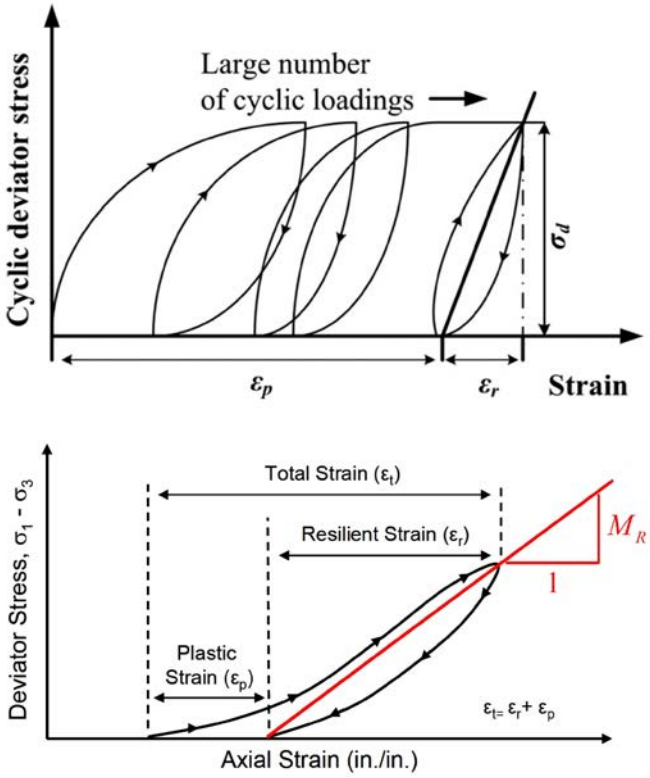

Figure 2 ***Response of granular material to cyclic deviator stress (top), and measurement of resilient modulus (bottom).*** (From Fig. 2 of Han and Vanapalli [2016], and Fig. 1 of Buchanan [2007].)

1.2 Geogrid Gain Factor

The material in this subsection is a summary of the more extensive presentation in Potyondy et al. (2016). The traditional reason to use geogrid in Minnesota has been to provide a more stable construction platform by improving the strength of the pavement foundation when weak soils are present (Clyne, 2001). A more recent reason to use geogrid has been to provide additional stiffness to the aggregate base layer. Geogrid use is known to increase aggregate compaction during construction, thereby allowing the aggregate base to more effectively protect the underlying soil layers from traffic loads. Geogrid use is also expected to improve both the short- and long-term performance of roadways; however, greater justification and quantification of this expectation is desired.

The primary structural benefit of adding geogrid to the aggregate base layer of a flexible pavement is to provide lateral restraint. Lateral restraint is provided for the base layer as the result of interlocking and friction between the geogrid and the aggregate. Under repeated loads, the base layer tends to spread laterally, and some of the shear stress in the base layer can be transferred to tensile stress in the geogrid. A stiff geogrid will act to restrain the lateral spreading and result in a stiffer aggregate base. The lateral-restraint mechanism (as summarized in Bagshaw et al. [2015]) ". . .is that by

restricting the ability of the aggregate particles to move, and by effectively fixing them into place via interaction with the geogrid, mass transfer through the pavement will be restricted. If particles cannot move, then the modulus of the matrix will be maintained, and the rate of accumulation of plastic deformation via shear and/or consolidation will be reduced."

It is understood that the use of geogrids in roadway aggregate base layer construction is beneficial (Skallman, 2010); however, *MnPAVE* does not account for the presence of a geogrid within the aggregate base layer. The geogrid gain factor is introduced as a means to modify the *MnPAVE* design modulus to account for the presence of geogrid within the aggregate base layer. The geogrid gain factor is defined as the ratio of resilient modulus of the aggregate base with geogrid to resilient modulus of the aggregate base without geogrid. The pavement-design package is used to estimate the geogrid gain factors for typical aggregate-geogrid roadway configurations (Siekmeier et al, 2016). Triaxial tests of an aggregate base, both with and without geogrid, are modeled, and the resilient moduli are measured in these tests to estimate the geogrid gain factor. The *MnPAVE* design modulus for the aggregate base with geogrid is found by multiplying the design modulus for the aggregate base without geogrid by the gain factor.

1.3 Unsaturated Condition of Pavement Materials

Han and Vanapalli (2016) describe the unsaturated condition of pavement materials, and argue for the use of soil suction to predict their mechanical behavior.

> Compacted pavement base/subbase materials and subgrade soils stay in an unsaturated condition and are subjected to environmental influences. Environmental factors contribute to moisture regime and soil suction (ψ) variations within the pavement structure which, in turn, influence strength and stiffness of pavement materials. Several research studies in recent years have demonstrated the strong correlations between the mechanical properties of unsaturated soils and the ψ. It is therefore recommended to use ψ as a key parameter to interpret and predict the response of the mechanical behavior of unsaturated soils to the soil moisture regime fluctuations. (Han and Vanapalli, 2016, p. 1)

The pavement-design package provides a means to predict the $M_R - \psi$ correlations for typical pavement materials both with and without geogrid.

2.0 PAVEMENT-DESIGN PACKAGE

The pavement-design package supports creation and triaxial testing of a synthetic unsaturated granular material containing geogrid (see Figure 3). The mechanical behavior of this discrete system is simulated by the three-dimensional discrete-element program *PFC3D*. The model can simulate the movement and interaction of hundreds of thousands of finite-sized particles. The particles are rigid bodies with finite mass that move independently of one another and can both translate and rotate. Particles interact at pair-wise contacts by means of an internal force and moment. Contact mechanics is embodied in particle-interaction laws (called contact models) that update the internal forces and moments. The time evolution of this system is computed via the distinct-element method, which provides an explicit dynamic solution to Newton's laws of motion. The PFC model can be envisioned as a synthetic material that encompasses a vast microstructural space spanning from the granular material described here to the rich variety of solid materials provided by the bonded-particle modeling methodology (Potyondy, 2015). The synthetic system described here consists of unsaturated granular material and geogrid. The unsaturated granular material is modeled as spherical or clumped grains that interact with one another via the hill contact model. The synthetic material is denoted as a hill material and described in Potyondy (2016). The geogrid is modeled as strings of overlapping spherical balls joined by either parallel bonds or beamed contacts. The parallel bonds or beamed contacts provide the structural properties of the grid, and the spherical balls provide the surface for grid-object interaction.

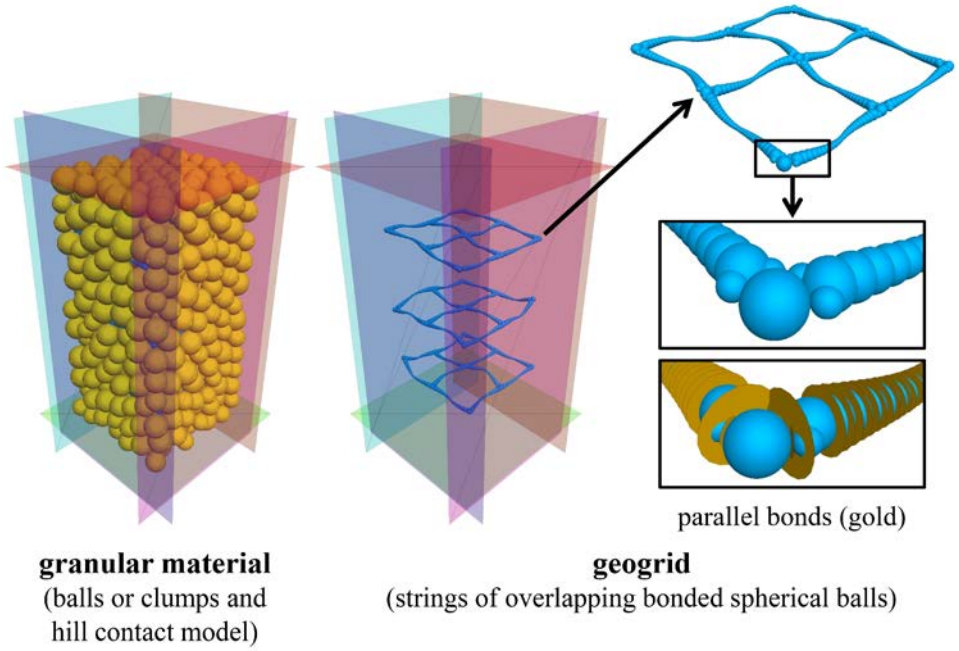

Figure 3 Pavement-design package supports creation and triaxial testing of synthetic unsaturated granular material containing geogrid, and measurement of resilient modulus for grid and no grid.

The grid-modeling methodology is described in the first subsection. The geogrids are specified as a grid set consisting of identical flat geogrids oriented perpendicular to the specimen axis and spaced evenly in the axial direction (see Figure 4). The grid-set description includes a definition of the grid-set parameters as well as the closed-form expressions defining the sizes and locations of the balls and either the radii of the parallel bonds for the parallel-bonded grid or the width and height of the rib cross section for the beamed grid. The grid-set properties are chosen to match the geogrid geometry, the rib tensile stiffness from a Single Rib Tensile test, and the junction torsional stiffness from an Aperture Stability Modulus test. These two grid-calibration tests are described in the next two subsections. The descriptions include demonstrations that the Tensar SS20 biaxial geogrid used in the pavement-design example matches the laboratory-test responses. The grid tensile stiffness is measured by the Multiple Aperture Tensile test that is described in the next subsection. The material-genesis procedure to embed a geogrid within the granular material is described in the final subsection.

2.1 Grid-Modeling Methodology: Grid Set

The grid-modeling methodology that uses parallel-bonded contacts draws upon the work of Stahl and co-workers (Jas et al. [2015a, 2015b]; Stahl and te Kamp [2013, 2012]; Stahl et al. [2014]; Stahl and Konietzky [2011]; Stahl [2011]; Konietzky et al. [2004]), with the primary contribution being the closed-form expressions defining the sizes and locations of the balls and the radii of the parallel bonds as summarized by Stille (2015).[3] The grid-modeling methodology that uses beamed contacts was developed for MnDOT and is described in this document. McDowell and co-workers (McDowell et al. [2006]; Chen et al. [2013]) describe a similar grid-modeling methodology in which the geogrid consists of spherical balls joined by parallel bonds. Qian and co-workers (Qian et al. [2015]) describe the modeling of granular material as discrete polyhedral grains in which rigid geogrids may be embedded, with the mechanical behavior of the discrete system being simulated by the three-dimensional discrete-element program BLOKS3D.

The grid-modeling methodology is summarized as follows. The grid consists of strings of overlapping spherical balls joined by either parallel bonds or beamed contacts. The parallel bonds or beamed contacts provide the structural properties of the grid, and the spherical balls provide the surface for grid-object interaction, which occurs at the grid-grain and grid-grid contacts. Each biaxial grid junction consists of two intersecting ribs, and for the parallel-bonded system, additional material in the form of join balls that increases the junction stiffness. Each triaxial grid junction consists of three intersecting ribs.

[3] Tensar International Limited is acknowledged for its research efforts modeling geogrids and granular soils, and in particular, for granting access to the grid-modeling methodology developed on its behalf by Itasca Consultants GmbH. Tensar is commended for its willingness to grant this access, fostering development of these models to benefit the wider industry.

There are five types of contacts in the modeled system: grain-grain, grid-grid, grid-grain, grid-wall and grain-wall. The grain-grain contacts employ the hill contact model, the grid-grid contacts employ either the linear parallel bond contact model or the beam contact model, and the remaining three contact types employ the linear contact model. The hill contact model provides the behavior of an infinitesimal, nonlinear elastic (no tension) and frictional interface that carries a compressive surface-interaction force and may carry a tensile moisture force. The parallel-bond and beam contact models provide the behavior of a finite-size, linear elastic and bonded interface that carries a force and moment. The interface of the parallel-bonded contact model has a circular cross section, while the interface of the beam contact model has a rectangular cross section. The linear contact model provides the behavior of an infinitesimal, linear elastic (no tension) and frictional interface that carries a force. The hill contact model is described in Potyondy (2016), the parallel-bond and linear contact models are described in Itasca (2018), and the beam contact model is described in Potyondy (2018b).

Each grid rib behaves either as an elastic beam of circular cross section with varying radius along its length (parallel-bonded contacts), or as a prismatic and bisymmetrical elastic beam with varying width and height along its length (beamed contacts). The grid behaves as an elastic body; it will not break, and it will return to its original shape when unloaded. The grid methodology of Stahl and te Kamp (2013) employed a parallel-bond radius and stiffness decreasing law to allow the grid to exhibit nonlinear and plastic behavior. The stiffness decreasing law is excluded from the present methodology, which is believed to be sufficient for cases in which the grid experiences small-deformation loading for which rib tensile strains remain less than three percent and junction rotations remain less than two degrees.

The geogrids are specified as a grid set that consists of identical flat geogrids oriented perpendicular to the global *z*-axis, and spaced evenly in the *z*-direction. When embedding the grid set within a granular material, the grid set is aligned with the specimen axis and positioned within either a polyaxial or cylindrical cell. The grid-set parameters are listed in Table 1, and the modeled system is shown in Figure 4. Grid deformation causes strain energy to be stored in the contacts that join the grid balls to one another — expressions for the strain energy in the parallel-bonded and beamed contacts are given in Itasca (2018)[4] and Potyondy (2018b), respectively. The strain energy stored in the grid set (E_g, $E_g \geq 0$) is given by the FISH variable **`gd_Estr`**, and provides a scalar index of the load being carried by the grid.

[4] In documentation set at PFC Model Components: Contacts and Contact Models: Contact Models: Built-in Contact Models: Linear Parallel Bond Model: Energy Partitions.

Table 1 Grid Set Parameters

Parameter	Type	Range	Default	Description
Grid set group:				
n_g , **gd_ng**	INT	$[1,\infty)$	1	number of grids
s_z , **gd_sz**	FLT	$(0.0,\infty)$	NA	grid spacing (in *z*-direc.)
$\{n_x,n_y\}$, **gd_n{x,y}**	INT	$[1,\infty)$	$\{1,1\}$	number of cross elements in *x* and *y* direcs.
$\mathbf{c}$, **gd_c**	VEC	$[\mathbb{R},\mathbb{R},\mathbb{R}]$	$\mathbf{0}$	position of node ball of bottom back left cross element (see Figure 4)
C_t , **gd_tips**	INT	$\{0,1\}$	0	grid-tip code $\begin{cases} 0, & \text{remove grid tips} \\ 1, & \text{keep grid tips} \end{cases}$
C_g , **gd_beamed**	INT	$\{0,1,2\}$	0	grid-type code $\begin{cases} 0, & \text{biaxial with parallel-bonded contacts} \\ 1, & \text{biaxial with beamed contacts} \\ 2, & \text{triaxial with beamed contacts} \end{cases}$
D_n , **gd_Dn**	FLT	$(0.0,\infty)$	NA	diameter of node ball
l_r , **gd_lr**	FLT	$(0.0,\infty)$	NA	length of rib
κ_r , **gd_Drat**	FLT	$(0.0,1.0)$	0.9	diameter ratio of first rib ball $\left(\kappa_r = D_c^{(1)}/D_n,\ C_g = 0\right)$
n_c , **gd_nc**	INT	$[1,\infty)$	7	core balls per half rib $\left(C_g = 0\right)$
D_m , **gd_Dm**	FLT	$(0.0,\infty)$	NA	diameter of mid-rib ball $\left(C_g \neq 0\right)$
$\bar{R}_n$, **gd_pbRadNd**	FLT	$(0.0,\infty)$	NA	parallel-bond radius at node ball $\left(C_g = 0\right)$
$\bar{R}_m$, **gd_pbRadMid**	FLT	$(0.0,\infty)$	NA	parallel-bond radius at mid rib $\left(\bar{R}_m \le \bar{R}_n,\ C_g = 0\right)$
$\bar{\lambda}_j$, **gd_pbRmulJn**	FLT	$(0.0,\infty)$	1.0	parallel-bond radius multiplier of join balls $\left(C_g = 0\right)$
b_n, **gd_XCbNd**	FLT	$(0.0,\infty)$	NA	rib cross-sectional width (aligned with xy-plane) at node ball $\left(C_g \neq 0\right)$
h_n , **gd_XChNd**	FLT	$(0.0,\infty)$	NA	rib cross-sectional height (aligned with z-axis) at node ball $\left(C_g \neq 0\right)$
b_m , **gd_XCbMid**	FLT	$(0.0,\infty)$	NA	rib cross-sectional width (aligned with xy-plane) at mid rib $\left(b_m \le b_n,\ C_g \neq 0\right)$

h_m, **gd_XChMid**	FLT	$(0.0,\infty)$	NA	rib cross-sectional height (aligned with z-axis) at mid rib $(h_m \le h_n,\ C_g \ne 0)$
C_e, **gd_latExtent**	INT	$\{0,1\}$	0	exclusion region lateral-extent existence code $\begin{cases} 0, & \text{exists} \\ 1, & \text{does not exist} \end{cases}$
Material properties group:				
α_g, **gd_dampFac**	FLT	$[0.0,0.7]$	0.0	local-damping factor
ρ_g, **gd_density**	FLT	$(0.0,\infty)$	NA	density (set grid-ball density: $\rho_b = \rho_g$, does not account for grid-ball overlap)
E_g^*, **gd_emod**	FLT	$[0.0,\infty)$	0.0	effective modulus $(C_g = 0)$
κ_g^*, **gd_krat**	FLT	$[0.0,\infty)$	0.0	stiffness ratio $(C_g = 0)$
E_g, **gd_E**	FLT	$[0.0,\infty)$	0.0	Young's modulus $(C_g \ne 0)$
ν_g, **gd_nu**	FLT	$(-1.0,0.5]$	0.0	Poisson's ratio $(C_g \ne 0)$
E_{gs}^*, **gd_gsemod**	FLT	$[0.0,\infty)$	0.0	grid-surface effective modulus
κ_{gs}^*, **gd_gskrat**	FLT	$[0.0,\infty)$	0.0	grid-surface stiffness ratio
μ_{gs}, **gd_gsfric**	FLT	$[0.0,\infty)$	0.0	grid-surface friction coefficient

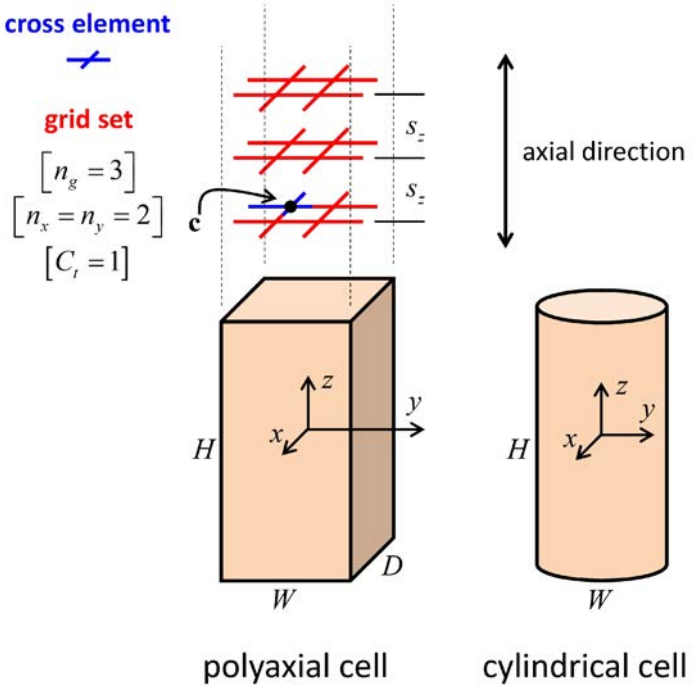

Figure 4 ***Material vessels and grid set consisting of three biaxial grids, each of which has four cross elements shown in Figures 5 and 10.***

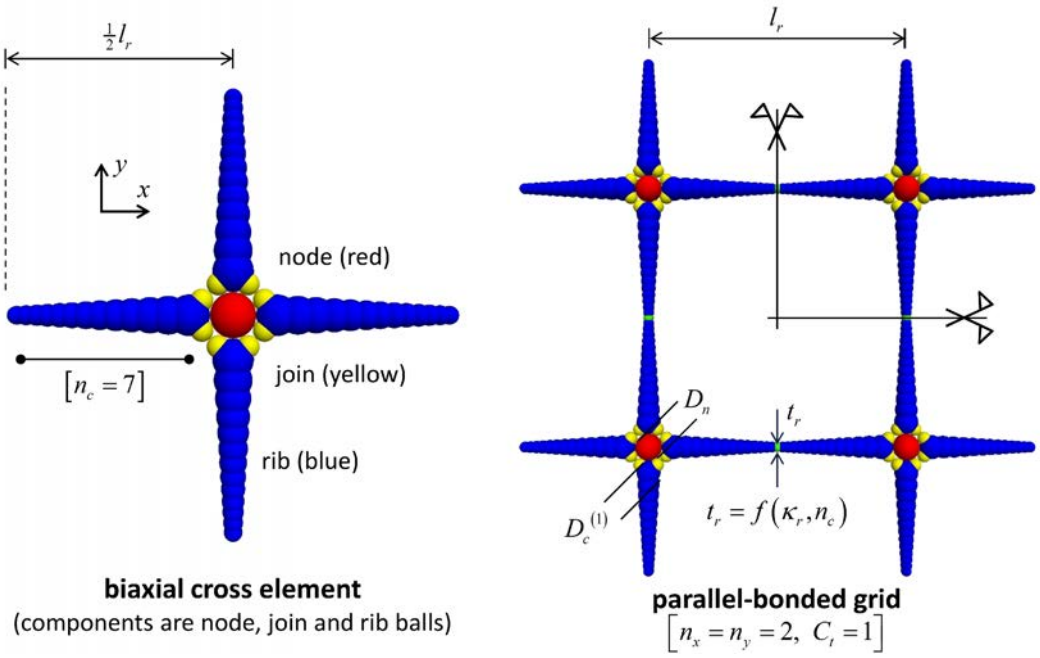

Figure 5 ***Cross element and biaxial parallel-bonded grid consisting of four cross elements.***

The grid set consists of n_g identical grids. Each grid is flat and lies in the *xy*-plane, and the grids are spaced evenly along the *z*-axis at a distance of s_z. A grid consists of identical cross elements, with n_x and n_y cross elements in the *x*- and *y*-directions, respectively. A biaxial cross element consists of one node ball with a half rib in both directions (see Figures 5 and 10), while a triaxial cross element consists of one node ball with a half rib in three directions (see Figure 11)[5]. The bottom back left cross element of the grid set is centered at $\mathbf{c}$. The presence of cross-element tips at the outside edge of the grid set is controlled by the grid-tip code C_t.

The grids that consist of either parallel-bonded contacts or beamed contacts are described in their own sections that follow.

2.1.1 Parallel-bonded grid

The geometry of a cross element is defined by the node-ball diameter $\left(D_n\right)$, the diameter ratio of the first rib ball $\left(\kappa_r = D_c^{(1)}/D_n\right)$, the rib length $\left(l_r\right)$, and the number of core balls per half rib $\left(n_c\right)$. The minimum rib thickness $\left(t_r\right)$ is a function of κ_r and n_c. The parallel-bond radii in the grid are defined by the parallel-bond radii at the node and mid rib ($\bar{R}_n$ and $\bar{R}_m$ along with an exponential variation along each half rib) and the parallel-bond radius multiplier of the join balls $\left(\bar{\lambda}_j\right)$. The material properties of the grid are defined by the local-damping factor, density, effective modulus and stiffness ratio (α_g, ρ_g, E_g^* and κ_g^*). The material properties of the grid surface are defined by the grid-surface effective modulus, stiffness ratio and friction coefficient (E_{gs}^*, κ_{gs}^* and μ_{gs}).[6]

[5] Each cross element is symmetric; thus, there is no differentiation between the transverse (TD) and longitudinal (LD) directions. Such a differentiation was employed by Stahl and te Kamp (2013). The pavement-design package can be modified to account for this by making the TD and LD directions correspond with the *x*- and *y*-directions, and replacing l_r and n_c with $\left\{l_{rx}, l_{ry}\right\}$ and $\left\{n_{cx}, n_{cy}\right\}$, respectively.

[6] The linear contact model is installed at the grid-grain and grid-grid contacts that may form after grid creation; the stiffness and friction coefficient of these contacts are set based on the specified deformability and friction coefficient. The linear contact model is also installed at the grid-wall contacts that may form after grid creation; the walls are frictionless, and the normal stiffness of these contacts is set based on the effective modulus of the material vessel. [The linear contact bond model is installed at grid-grain and grid-grid contacts to facilitate visual inspection of these contacts via the contact plot item (using Color By: Text Val: model name). The linear contact bond model is unbonded, and thus, its behavior is identical to that of the linear contact model.]

The parallel bonds in the grid are assigned infinite strengths to preclude bond breakage, the parallel-bond stiffnesses are set based on E_g^* and κ_g^*, the parallel-bond radii at each join ball are set based on $\bar{\lambda}_j$ and join-ball diameter, and the parallel-bond radii along each half rib are set via Eq. (6).[7]

The closed-form expressions defining the sizes and locations of the balls and the radii of the parallel bonds are provided in the remainder of this subsection. The balls of a cross element half rib are shown in Figure 6. The half rib consists of one node ball, two join balls, and a string of rib balls, with the rib balls being divided into core-rib balls, mid-rib balls and a tip-rib ball. The sizes of the core-rib balls satisfy the relation:

$$\tfrac{1}{2} l_r = \tfrac{1}{2} D_n + \sum_{b=1}^{n_c} \alpha^{(b-1)} \kappa_r D_n. \tag{1}$$

This relation is rewritten in the form:

$$f(\alpha) = \frac{D_n - l_r}{2\kappa_r D_n} + \sum_{b=1}^{n_c} \alpha^{(b-1)} = 0. \tag{2}$$

The constant, α, is found by solving the above expression via Newton-Raphson iteration. The diameters and positions of the rib balls are expressed in terms of alpha as follows. The diameters and positions of the core-rib balls:

$$\begin{aligned} D_c^{(b)} &= \alpha^{(b-1)} \kappa_r D_n, \;\; b \in \{1, 2, \ldots, n_c\} \\ s_c^{(b)} &= s_c^{(b-1)} + \tfrac{1}{2} D_c^{(b-1)} + \tfrac{1}{2} D_c^{(b)}, \;\; D_c^{(0)} = D_n, \;\; s_c^{(0)} = 0, \;\; b \in \{1, 2, \ldots, n_c\}. \end{aligned} \tag{3}$$

The diameters and positions of the mid-rib balls:

$$\begin{aligned} D_m^{(b)} &= \frac{2\alpha}{(1+\alpha)^2} \left(D_c^{(b)} + D_c^{(b+1)} \right), \quad D_m^{(n_c)} = 2 D_c^{(n_c)} - D_m^{(n_c-1)}, \quad b \in \{1, 2, \ldots, n_c - 1\} \\ s_m^{(b)} &= s_c^{(b)} + \tfrac{1}{2} D_c^{(b)}, \;\; b \in \{1, 2, \ldots, n_c\}. \end{aligned} \tag{4}$$

[7] The stiffnesses of the linear component of the linear parallel bond contact model are set to zero such that all load is carried in the bond — i.e., the linear force arising from ball-ball overlap always remains equal to zero.

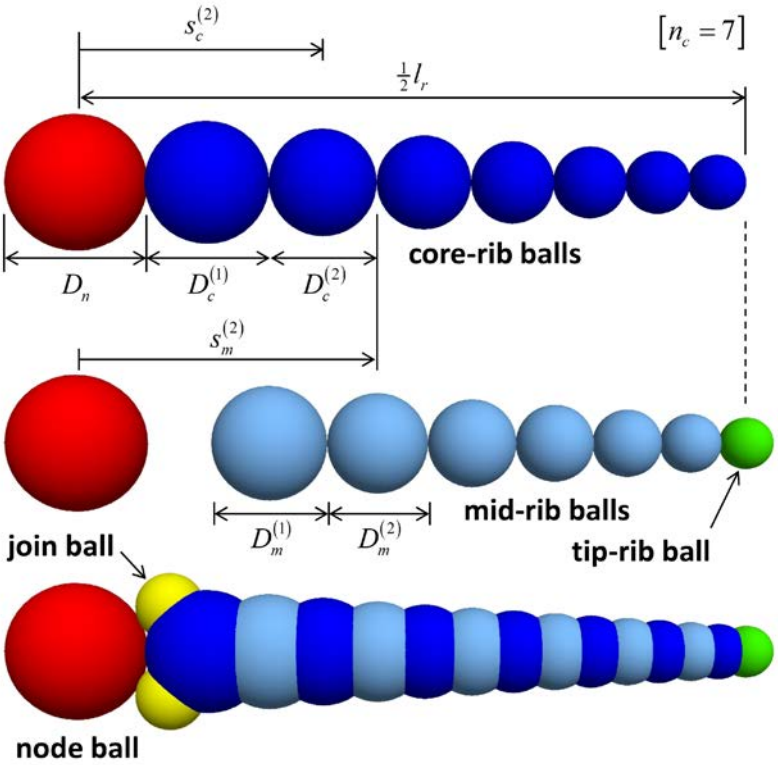

Figure 6 Cross element half rib showing node ball, join balls and rib balls.

There is also a tip-rib ball that lies between adjoining cross elements, and its diameter and position are obtained by treating it as a mid-rib ball. The diameters and positions of the join balls (with reference to Figure 7):

$$D_j = \tfrac{1}{2} D_n$$
$$\beta = \frac{\pi}{4} - \varphi, \quad \varphi = \sin^{-1}\left(\frac{D_j}{D_n + D_j}\right). \tag{5}$$

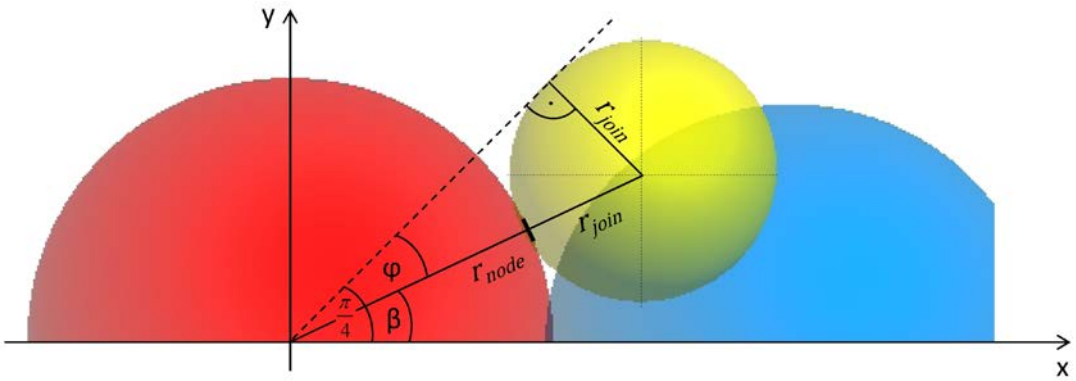

Figure 7 Cross element half rib showing location of the top join ball.

The parallel-bond radii in the geogrid vary exponentially along each half rib (see Figure 8):

$$\begin{aligned} &\overline{R} = ae^{bs}, \quad \tfrac{1}{2}D_n \le s \le \tfrac{1}{2}l_r \\ &\text{with} \quad a = \overline{R}_n \exp\left(\frac{-bD_n}{2}\right) \\ &\qquad b = \ln\left(\frac{\overline{R}_n}{\overline{R}_m}\right)\frac{2}{D_n - l_r} \end{aligned} \tag{6}$$

where s is measured from the node-ball center. Each join ball has four parallel bonds joining it to the node ball, the adjacent join ball, and the first two rib balls (see Figure 9).

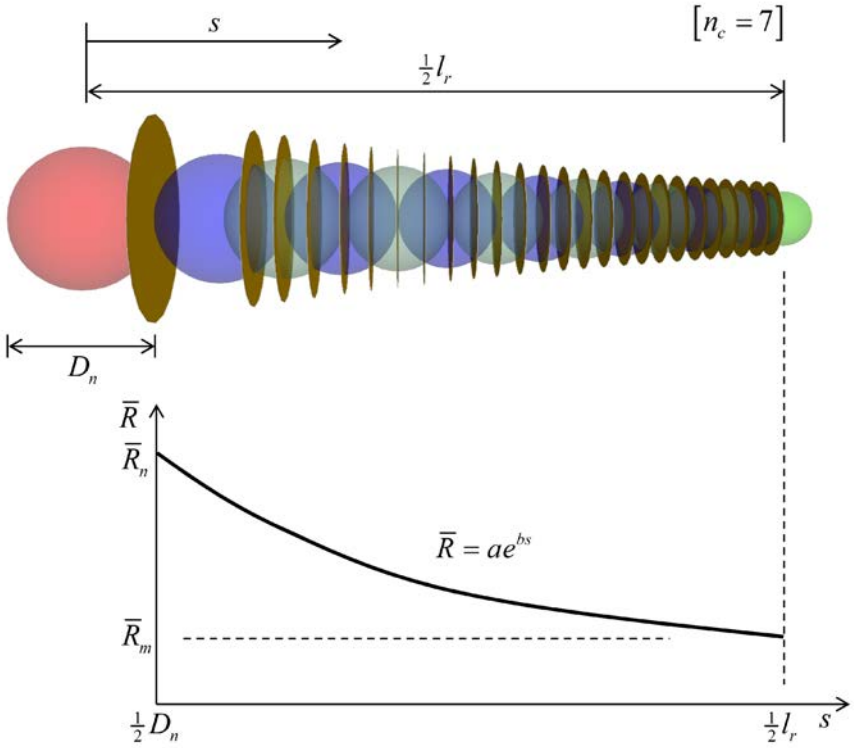

Figure 8 ***Cross-element half rib showing variation of parallel-bond radius from node ball to mid rib. Each parallel-bonded interface is drawn as a disk with radius equal to parallel-bond radius.***

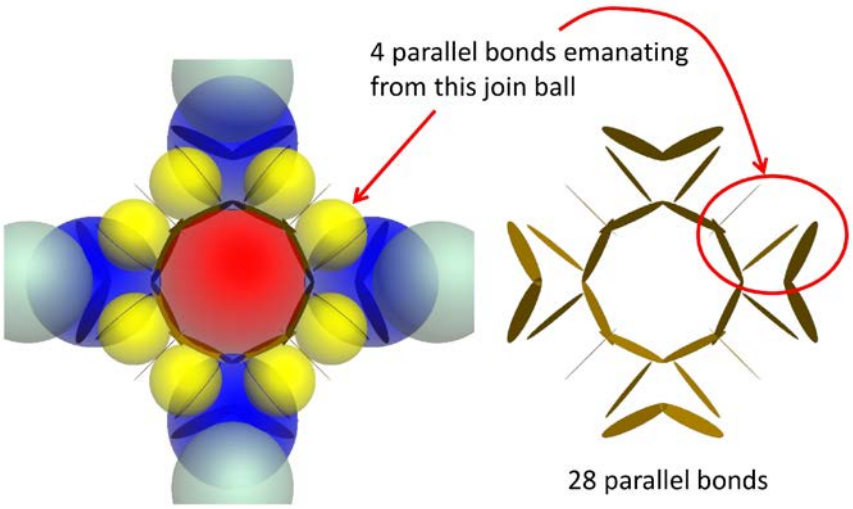

Figure 9 Parallel bonds emanating from the join balls at a cross-element node.

2.1.2 Beamed grid

The geometry of both biaxial and triaxial beamed grid cross elements is defined by the node-ball diameter (D_n), the rib length (l_r) and the mid-rib ball diameter (D_m) as shown in Figures 10 and 11. A string of balls with diameter D_m are created between the node and mid-rib balls, with the overlap being distributed equally among all contacts in the string. The width and height of the rib cross section are defined by the width and height at the node (b_n and h_n) and mid rib (b_m and h_m), along with an exponential variation along each half rib. The exponential variations are given by Eq. (6), with the width and height replacing the parallel-bond radius in this expression. The material properties of the beamed grid are defined by the local-damping factor and density (α_g, ρ_g) as well as the Young's modulus and Poison's ratio of the grid material $(E_g \text{ and } \nu_g)$. The material properties of the grid surface are defined by the grid-surface effective modulus, stiffness ratio and friction coefficient (E_{gs}^*, κ_{gs}^* and μ_{gs}).[8]

[8] The linear contact model is installed at the grid-grain and grid-grid contacts that may form after grid creation; the stiffness and friction coefficient of these contacts are set based on the specified deformability and friction coefficient. The linear contact model is also installed at the grid-wall contacts that may form after grid creation; the walls are frictionless, and the normal stiffness of these contacts is set based on the effective modulus of the material vessel. [The linear contact bond model is installed at grid-grain and grid-grid contacts to facilitate visual inspection of these contacts via the contact plot item (using Color By: Text Val: model name). The linear contact bond model is unbonded, and thus, its behavior is identical to that of the linear model.]

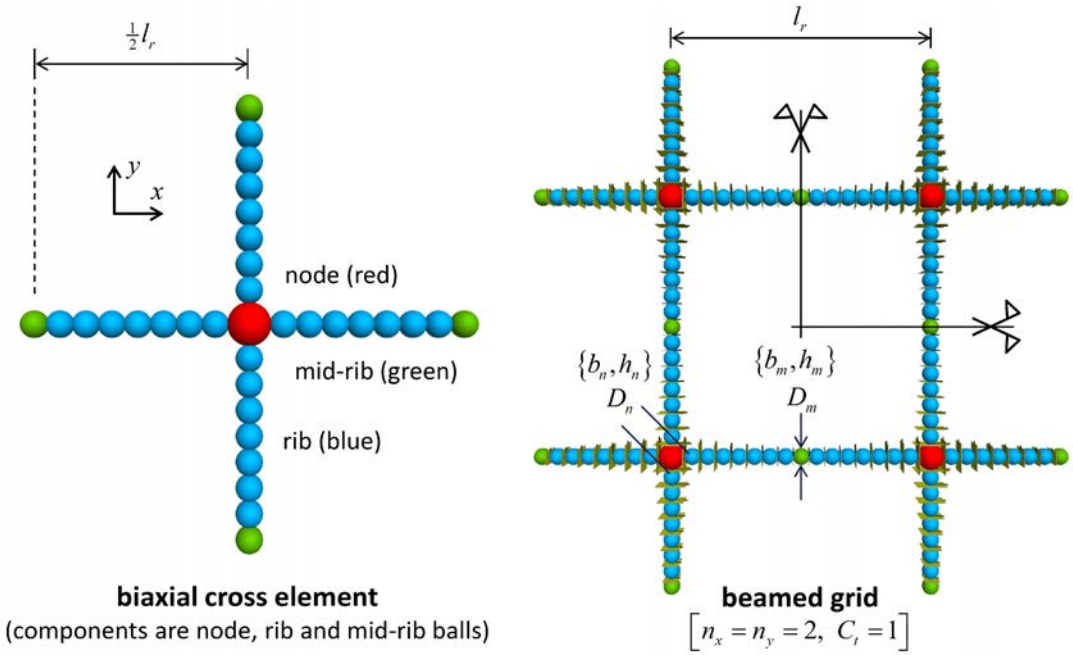

Figure 10 Cross element and biaxial beamed grid consisting of four cross elements.

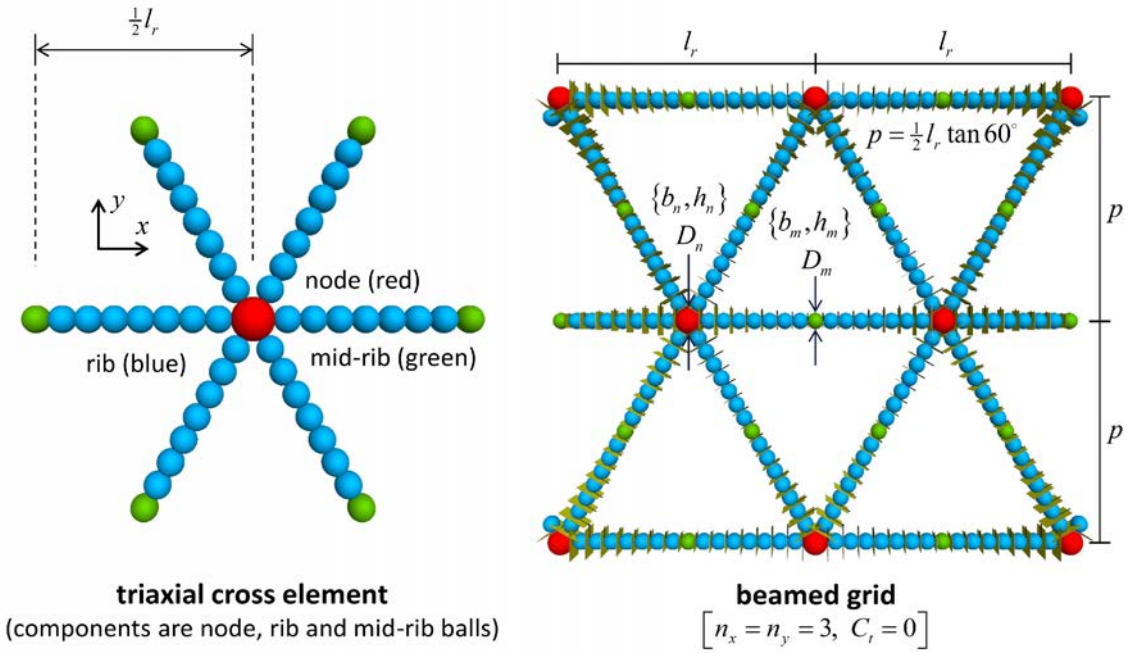

Figure 11 Cross element and triaxial beamed grid with tips removed.

2.2 Grid Calibration: Single Rib Tensile Tests

The rib tensile stiffnesses of a biaxial geogrid are measured by performing Single Rib Tensile (SRT) tests in the transverse (TD) and longitudinal (LD) directions. The two ribs emanating from a grid junction and aligned in the desired direction are clamped at the junctions at their ends (as shown in Figure 12). One end is fixed, and a constant velocity is applied to the other end while monitoring the applied displacement and associated force. The displacement is expressed as a strain using the length between clamps as the gauge length. The force-extension curves for a Tensar SS20 biaxial geogrid are shown in Figure 13, in which the black line is the average curve from five laboratory tests. The force-extension behaviors are similar in the TD and LD directions. The force-extension curve is linear for extension of less than three percent, at which point the slope begins to decrease. The slope of the force-extension curve is a measure of stiffness. The stiffness decrease indicates material softening, perhaps as the result of plastic yielding of the material at the rib center. A permanent rib extension would be associated with plastic yielding — it is not known to the author if a permanent rib extension has occurred.

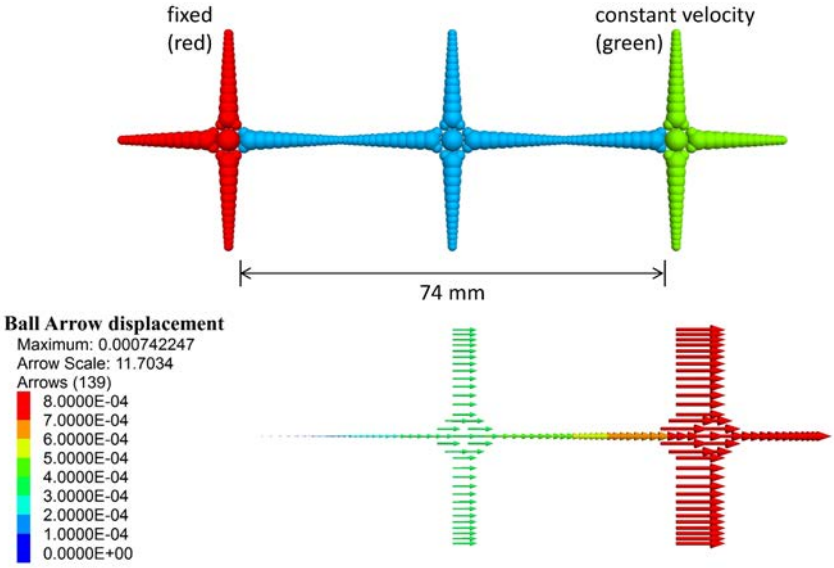

Figure 12 The undeformed SS20 parallel-bonded grid at the start of the SRT test (above), and the grid displacement field at the end of the SRT test (below).

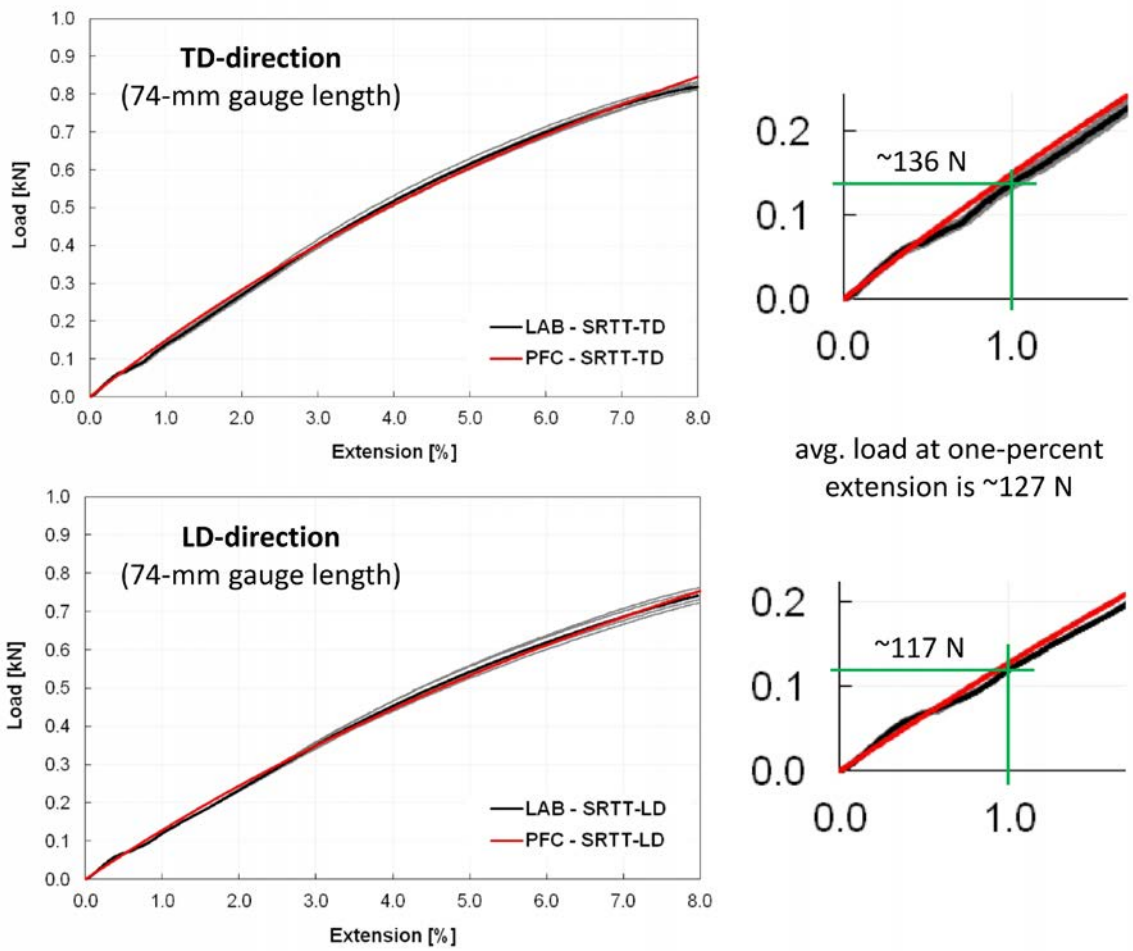

Figure 13 Force versus extension for a Tensar SS20 biaxial geogrid loaded in the TD and LD directions during SRT tests. (From Figs. 8 and 9 of Stahl and te Kamp [2013] in which force is denoted as load.)

The rib tensile stiffnesses of a triaxial geogrid are measured by performing Single Rib Tensile (SRT) tests in the three rib directions (30, 90 and 150 degrees). The two ribs emanating from a grid junction and aligned in the desired direction are clamped at the junctions at their ends (as shown in Figure 14). One end is fixed, and a constant velocity is applied to the other end while monitoring the applied displacement and associated force. The displacement is expressed as a strain using the length between clamps as the gauge length. The force-extension curves for a Tensar TX160 triaxial geogrid are shown in Figures 15 and 16, in which the black line is the average curve from five laboratory tests. The force-extension behaviors differ in the three directions, with the 90 degree rib direction that is aligned with the transverse/cross machine direction (TD) being the stiffest. The force-extension curves are linear for extension of less than three percent, at which point the slopes begin to decrease.

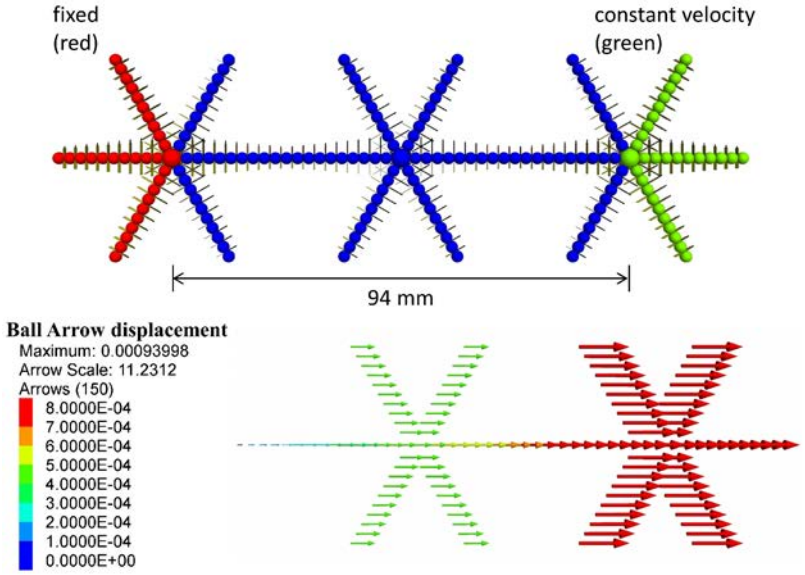

Figure 14 The undeformed TX160 beamed grid at the start of the SRT test (above), and the grid displacement field at the end of the SRT test (below).

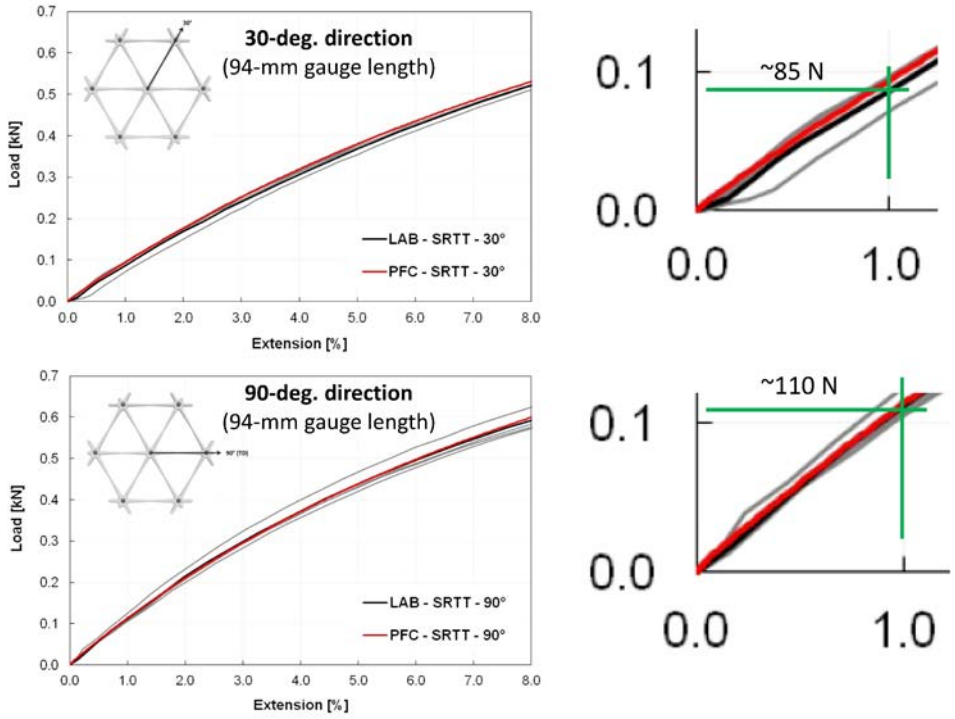

Figure 15 Force versus extension for a Tensar TX160 triaxial geogrid loaded in the 30 and 90 degree directions during SRT tests. (From Figs. 11 and 12 of Stahl and te Kamp [2012] in which force is denoted as load.)

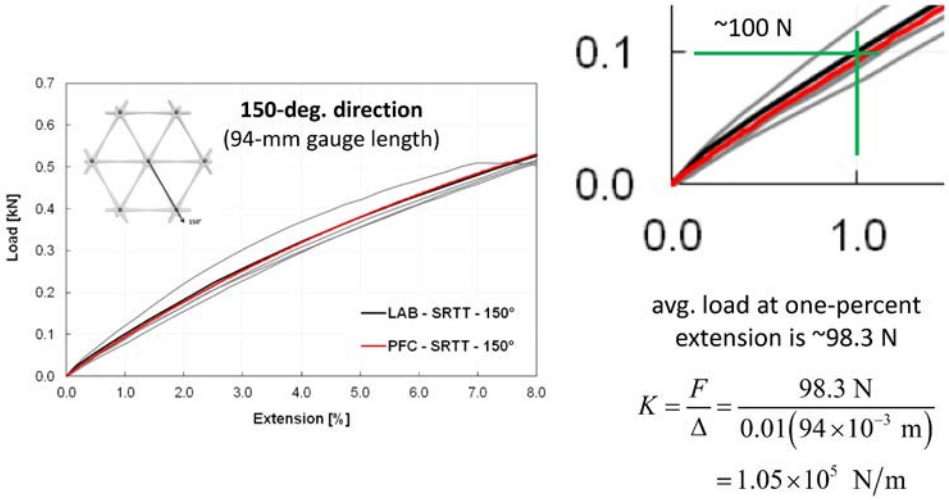

Figure 16 ***Force versus extension for a Tensar TX160 triaxial geogrid loaded in the 150 degree direction during SRT tests.*** (From Fig. 13 of Stahl and te Kamp [2012] in which force is denoted as load.)

2.2.1 Parallel-bonded grid (biaxial)

The Tensar SS20 biaxial geogrid is modeled in the pavement-design example using the grid-set properties in Table 5. The synthetic geogrid is symmetric, with no differentiation between the TD and LD directions; therefore, the grid-set properties are chosen to match the average stiffness for extension less than three percent. The modeled system at the start and end of the SRT test is shown in Figure 12. The applied force is obtained by summing the out-of-balance forces of the balls that are assigned a constant velocity. The force-extension curve for quasi-static loading is shown in Figure 17. The modeled system matches the average force of 127 N at one-percent extension.

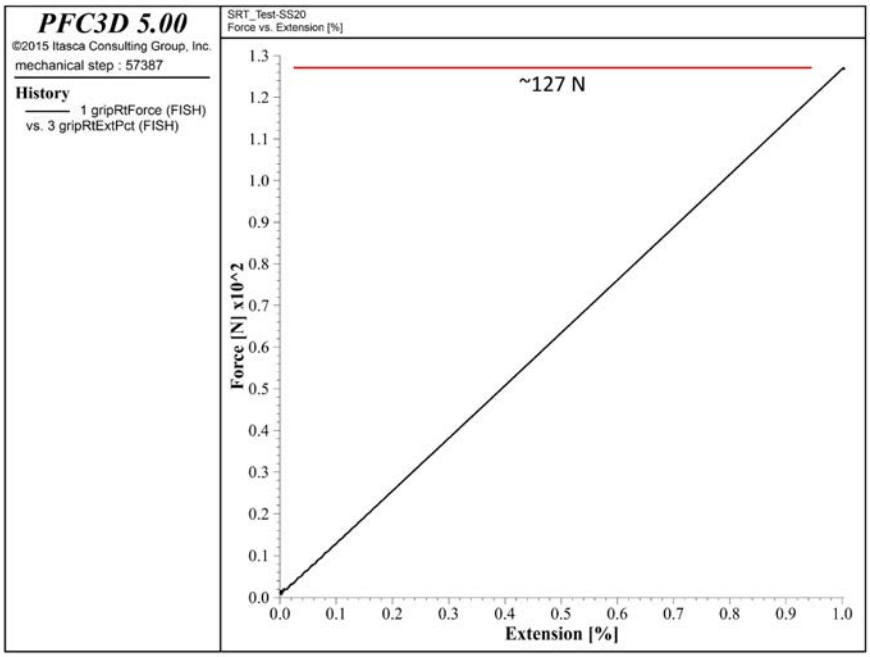

Figure 17 Force versus extension for the SS20 parallel-bonded grid during the SRT test, and measurement of force for a one-percent extension.

2.2.2 Beamed grid (biaxial)

The Tensar SS20 biaxial geogrid is modeled using the grid-set properties in Table 2. The synthetic geogrid is symmetric, with no differentiation between the TD and LD directions; therefore, the grid-set properties are chosen to match the average stiffness for extension less than three percent. The modeled system at the start and end of the SRT test is shown in Figure 18. The modeled system matches the average force of 127 N at one-percent extension. Reducing the mid-rib ball diameter from 2.5 to 1.5 mm has a negligible effect on system stiffness.

Table 2 Grid Set Properties of SS20 Beamed Grid*

Property	Value
Grid set group:	
$n_g,\ s_z\,[\text{mm}],\ \{n_x,n_y\},\ \mathbf{c}\,[\text{mm}],\ C_t$	$1,\ \text{NA},\ \begin{cases}\{3,1\},\ \text{SRT test}\\ \{7,7\},\ \text{ASM test}\end{cases},\ (0,0,0),\ 1$
$C_g,\ D_n\,[\text{mm}],\ l_r\,[\text{mm}],\ D_m\,[\text{mm}]$	1, 4.0, 39.0, 2.5
$b_n\,[\text{mm}],\ b_m\,[\text{mm}],\ h_n\,[\text{mm}],\ h_m\,[\text{mm}],\ C_e$	5.0, 2.0, 3.5, 3.5, 0
Material properties group:	
$\alpha_g,\ \rho_g\,[\text{kg/m}^3],\ E_g\,[\text{GPa}],\ \nu_g$	0.7, 950, 1.2, 0.42
$E_{gs}^*\,[\text{MPa}],\ \kappa_{gs}^*,\ \mu_{gs}$	500, 2.0, 0.5

* Grid-set parameters are defined in Table 1.

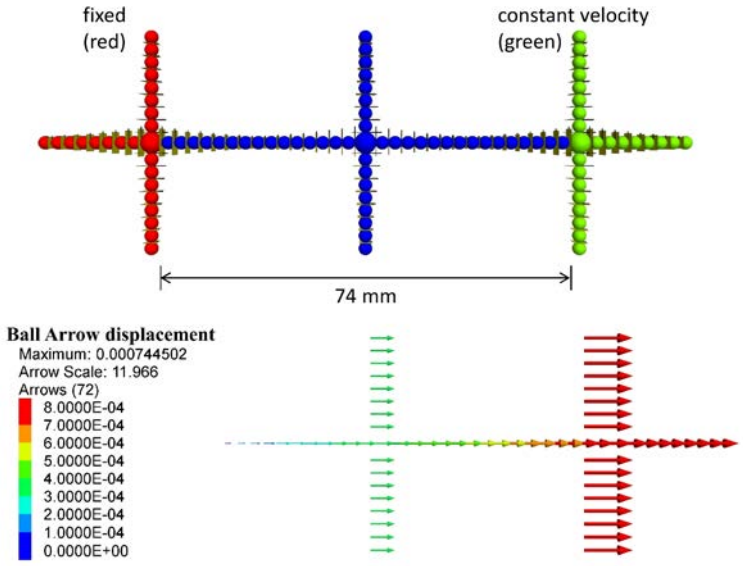

Figure 18 The undeformed SS20 beamed grid at the start of the SRT test (above), and the grid displacement field at the end of the SRT test (below).

2.2.3 Beamed grid (triaxial)

The Tensar TX160 triaxial geogrid is modeled using the grid-set properties in Table 3. The synthetic geogrid is symmetric, with no differentiation between the three rib directions; therefore, the grid-set properties are chosen to match the average stiffness for extension less than three percent. The modeled system at the start and end of the SRT test is shown in Figure 14. The modeled system has a stiffness of 1.05×10^{5} N/m, which matches the average stiffness of the TX160 triaxial geogrid shown in Figure 16. Reducing the mid-rib ball diameter from 2.5 to 1.5 mm has a negligible effect on system stiffness.

Table 3 Grid Set Properties of TX160 Beamed Grid*

Property	Value
Grid set group:	
$n_g,\ s_z\,[\text{mm}],\ \{n_x,n_y\},\ \mathbf{c}\,[\text{mm}],\ C_t$	$1,\ \text{NA},\ \begin{cases}\{3,1\},\ \text{SRT test}\\ \{7,9\},\ \text{ASM test}\end{cases},\ (0,0,0),\ 1$
$C_g,\ D_n\,[\text{mm}],\ l_r\,[\text{mm}],\ D_m\,[\text{mm}]$	2, 4.0, 47.0, 2.5
$b_n\,[\text{mm}],\ b_m\,[\text{mm}],\ h_n\,[\text{mm}],\ h_m\,[\text{mm}],\ C_e$	8.0, 4.0, 1.4, 1.4, 0
Material properties group:	

$\alpha_g,\ \rho_g\ [\mathrm{kg/m^3}],\ E_g\ [\mathrm{GPa}],\ \nu_g$	0.7, 950, 1.2, 0.42
$E_{gs}^*\ [\mathrm{MPa}],\ \kappa_{gs}^*,\ \mu_{gs}$	500, 2.0, 0.5

* Grid-set parameters are defined in Table 1.

2.3 Grid Calibration: Aperture Stability Modulus Tests

The junction torsional stiffness of a biaxial geogrid is measured by performing an Aperture Stability Modulus (ASM) test. A grid consisting of six by six apertures is clamped along its boundary as shown in Figure 19. The central junction is subjected to a twisting moment (M_t) by applying a force (F) to each of the four ribs emanating from the junction. The force is applied orthogonal to each rib at a fixed radial distance (r) such that $M_t = 4rF$. The rotation of the central junction (θ_t) is measured. The torsional stiffness of the junction is given by

$$k_t = \frac{M_t}{\theta_t}. \tag{7}$$

The concept of torsional stiffness is embodied in the following structural system. The torsional stiffness of a twisted elastic shaft of length L loaded at its ends by equal and opposite twisting moments is given by Crandall et al. (1978, Eq. 6.10):

$$M_t = k_t\theta_t, \quad k_t = \frac{GJ}{L} \tag{8}$$

where G is the shear modulus, and J is the polar moment of inertia of the cross-sectional area about the axis of the shaft.

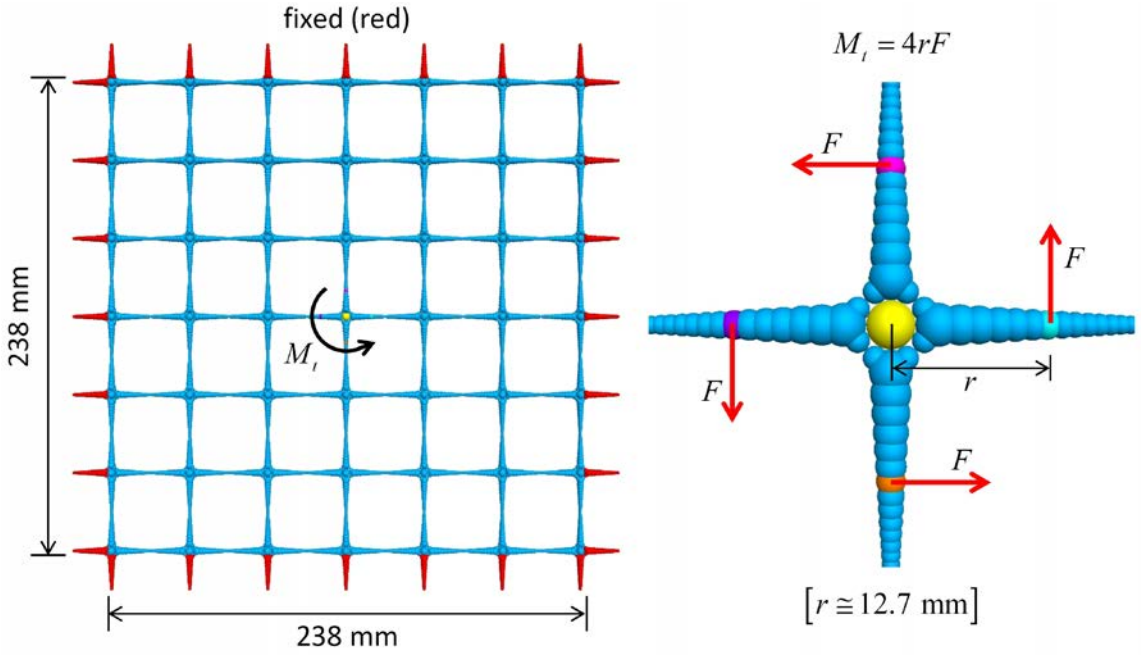

Figure 19 The SS20 parallel-bonded grid showing the boundary conditions for the ASM test.

The moment-rotation curve for a Tensar SS20 biaxial geogrid is shown in Figure 20, in which the black line is the average curve from three laboratory tests. The moment-rotation curve is linear for rotation of less than two degrees, at which point the slope begins to increase. The slope of the moment-rotation curve is the torsional stiffness. The torsional stiffness increases with increasing rotation. This is a geometrically nonlinear effect denoted as stress stiffening.[9]

[9] The effect whereby the tensile membrane forces in a shell effectively increase the bending stiffness of the shell is called stress stiffening (Cook et al., 1989, p. 429). The tensile forces in the grid are similar to membrane forces in a shell. As the tensile forces in the grid are increased, the bending *and* torsional stiffnesses of the grid increase. The increase in torsional stiffness is described in the following analogous fashion. The geogrid provides a torsional elastic resistance to the deformation induced by the twisting moment, which aids in supporting the moment. The elastic resistance increases with increasing applied rotation.

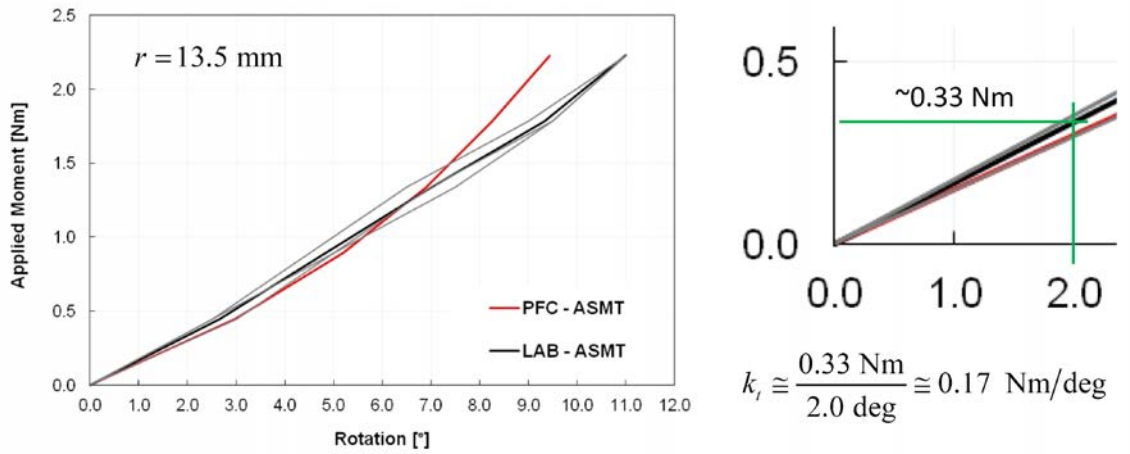

Figure 20 Moment versus rotation for a Tensar SS20 biaxial geogrid during an ASM test. (From Fig. 12 of Stahl and te Kamp [2013].)

The junction torsional stiffness of a triaxial geogrid is measured by performing an Aperture Stability Modulus (ASM) test. A grid consisting of six pitches by five nodes is clamped along its boundary as shown in Figure 21. The central junction is subjected to a twisting moment (M_t) by applying a force (F) to each of the six ribs emanating from the junction. The force is applied orthogonal to each rib at a fixed radial distance (r) such that $M_t = 6rF$. The rotation of the central junction (θ_t) is measured. The torsional stiffness of the junction is given by Eq. (7).

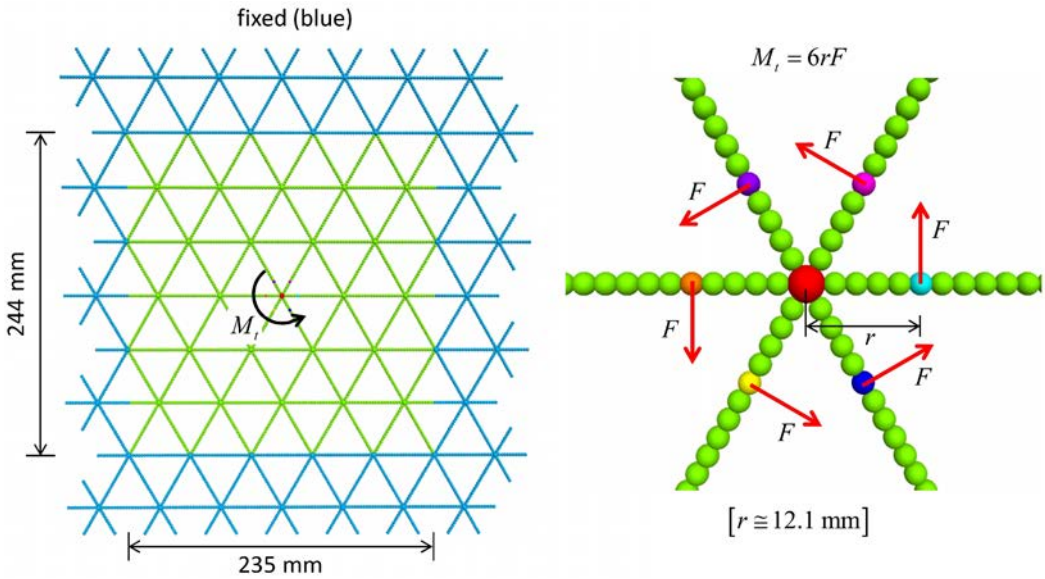

Figure 21 The TX160 beamed grid showing the boundary conditions for the ASM test.

The moment-rotation curve for a Tensar TX160 triaxial geogrid is shown in Figure 22, in which the black line is the average curve from four laboratory tests. The moment-rotation curve is linear. The slope of the moment-rotation curve is the torsional stiffness. The average torsional stiffness of the four curves is 0.48 Nm/deg.

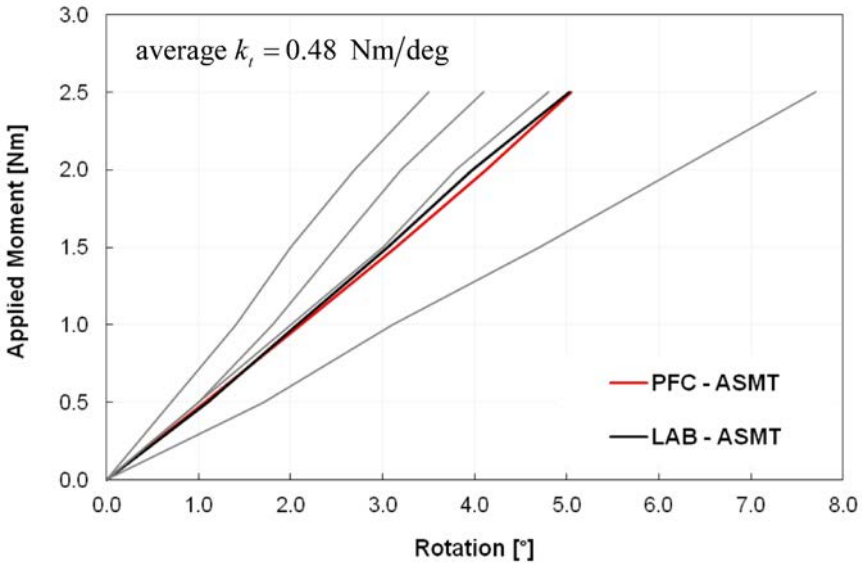

Figure 22 Moment versus rotation for a Tensar TX160 triaxial geogrid during an ASM test. (From Fig. 23 of Stahl and te Kamp [2012].)

2.3.1 Parallel-bonded grid (biaxial)

The Tensar SS20 biaxial geogrid is modeled in the pavement-design example using the grid-set properties in Table 5. The modeled system is shown in Figure 19. A force of 5.9 N is applied to four grid balls, each of which is 12.7 mm from the central junction, such that the twisting moment is 0.30 Nm. Each force remains oriented in its initial global direction throughout the test. The model is run until the state of static equilibrium shown in Figure 23 has been obtained. The rotation is given by

$$\theta = \tan^{-1}\left(\frac{\Delta_y}{r}\right), \quad \text{valid for small-deformation} \tag{9}$$

where Δ_y is the y-displacement of the loaded ball to the right of the central junction. The rotational stiffness is found to be 0.15 Nm/deg, which is 12 percent less than the experimental data. This match is deemed to be sufficient for the purposes of this study. It should be possible to obtain a better match, without sacrificing the match of the rib tensile stiffness, by adjusting the parallel-bond radius multiplier of the join balls ($\overline{\lambda}_j$). Additional runs with applied forces of 20 and 40 N give

rotations of 5.9 and 9.5 deg, respectively, and rotational stiffnesses of 0.17 and 0.22 Nm/deg, respectively, which demonstrate that the model is exhibiting a stress-stiffening effect similar to that of the physical grid (see Figure 24).

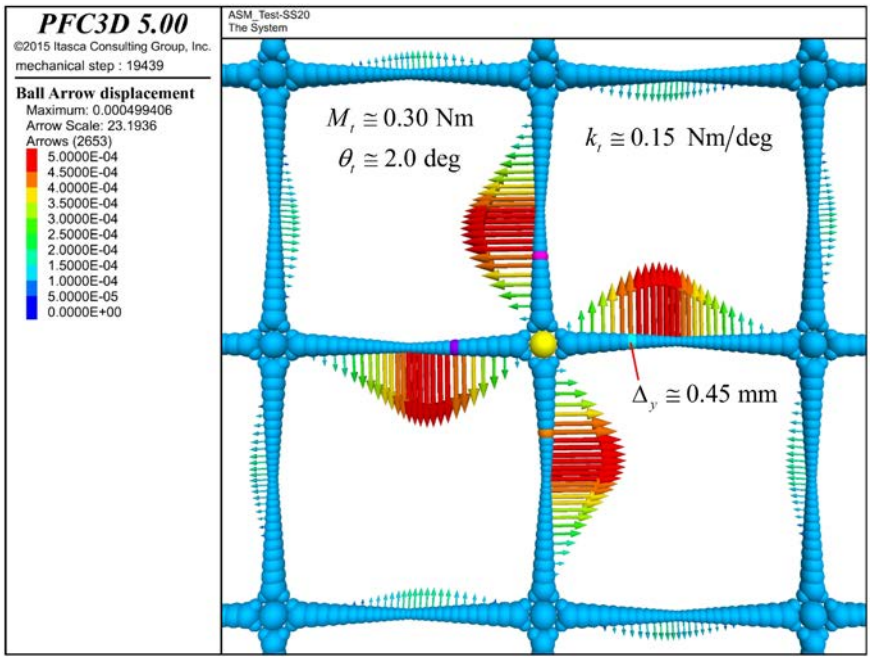

Figure 23 Deformed grid and displacement field near the central junction of the SS20 parallel-bonded grid at the end of the ASM test with applied moment of 0.30 Nm.

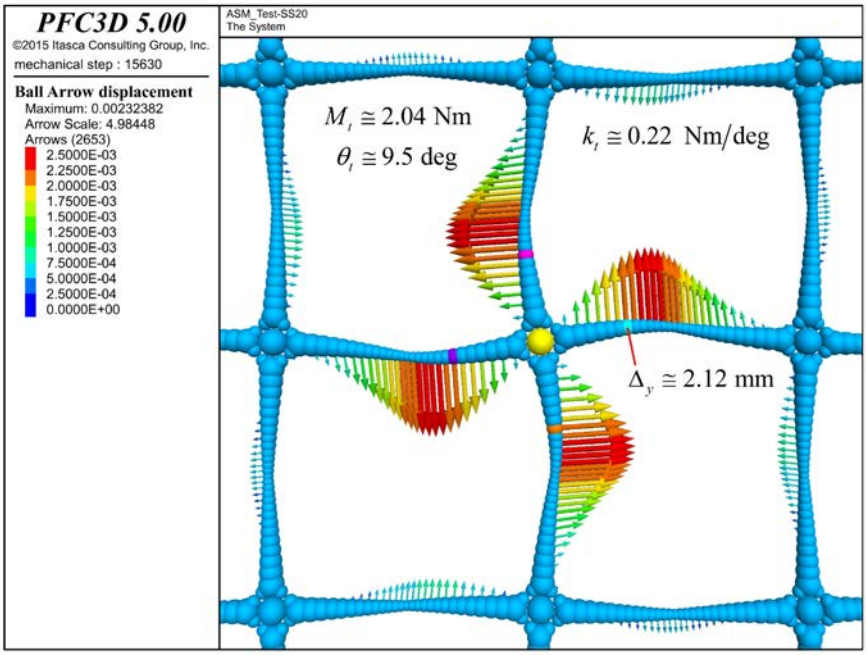

Figure 24 Deformed grid and displacement field near the central junction of the SS20 parallel-bonded grid at the end of the ASM test with applied moment of 2.04 Nm.

2.3.2 Beamed grid (biaxial)

The Tensar SS20 biaxial geogrid is modeled using the grid-set properties in Table 2. The modeled system is similar to the system shown in Figure 19. A force of 5.9 N is applied to four grid balls, each of which is approximately 12.5 mm from the central junction, such that the twisting moment is 0.29 Nm. Each force remains oriented in its initial global direction throughout the test. The model is run until the state of static equilibrium shown in Figure 25 has been obtained. The rotation is given by Eq. (9). The rotational stiffness is found to be 0.17 Nm/deg, which matches the experimental data. Reducing the mid-rib ball diameter from 2.5 to 1.5 mm has a negligible effect on rotational stiffness.

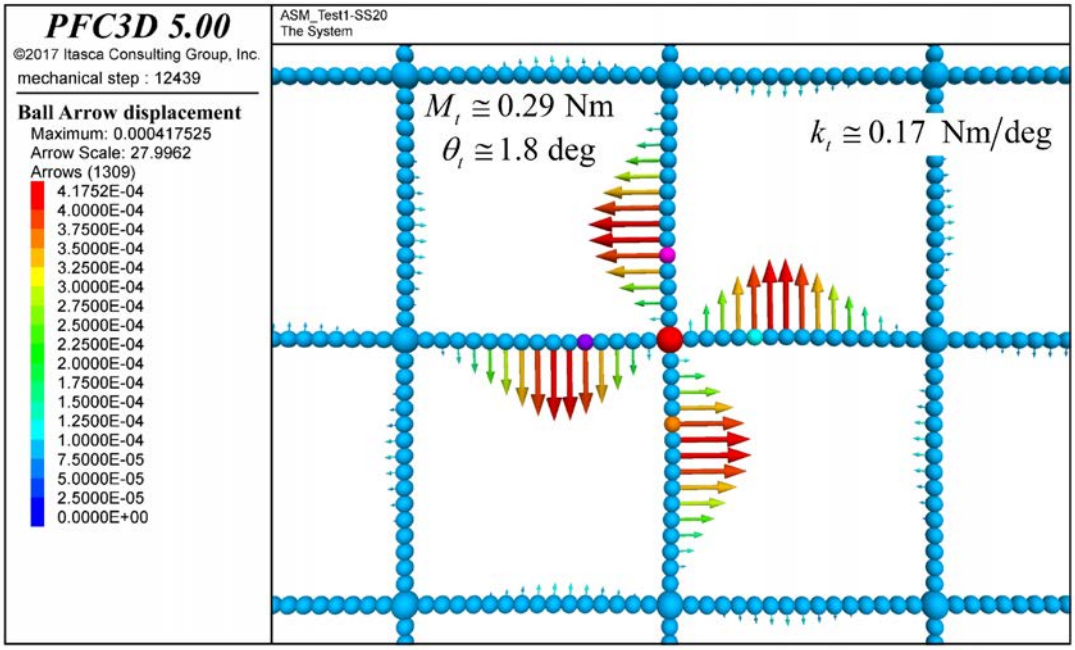

Figure 25 Deformed grid and displacement field near the central junction of the SS20 beamed grid at the end of the ASM test.

2.3.3 Beamed grid (triaxial)

The Tensar TX160 triaxial geogrid is modeled using the grid-set properties in Table 3. The modeled system is shown in Figure 21. A force of 12.8 N is applied to six grid balls, each of which is approximately 12.1 mm from the central junction, such that the twisting moment is 0.93 Nm. Each force remains oriented in its initial global direction throughout the test. The model is run until the state of static equilibrium shown in Figure 26 has been obtained. The rotation is given by Eq. (9). The rotational stiffness is found to be 0.47 Nm/deg, which effectively matches the experimental data. Reducing the mid-rib ball diameter from 2.5 to 1.5 mm reduces the rotational stiffness by 8.5% to 0.43 Nm/deg.

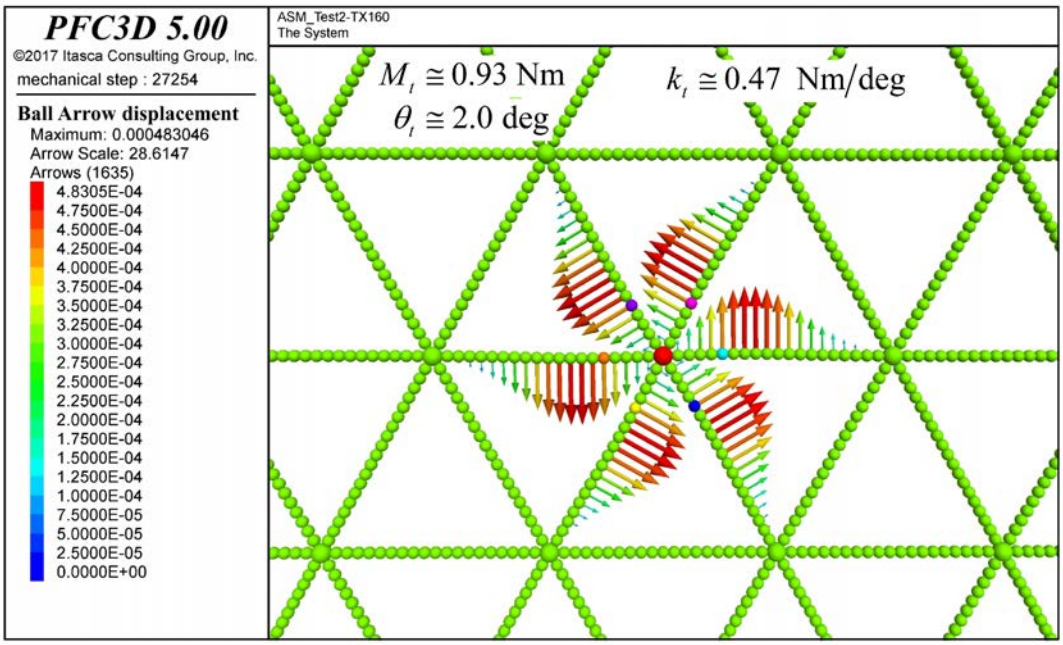

Figure 26 Deformed grid and displacement field near the central junction of the TX160 beamed grid at the end of the ASM test.

2.4 Grid Calibration: Multiple Aperture Tensile Tests

The tensile stiffness of the geogrid is measured by performing a Multiple Aperture Tensile (MAT) test. A grid consisting of multiple apertures is clamped along its left and right edges as shown in Figure 27. The left edge is fixed, and a constant velocity is applied to the right edge while monitoring the applied displacement (Δ) and associated force (F). The tensile stiffness is given by

$$k = \frac{F}{\Delta}. \tag{1.10}$$

The tensile stiffness is not constant, but varies as the number of apertures changes. An alternative stiffness measure that is independent of the number of apertures is the effective modulus given by

$$E' = \frac{kL}{A'} = \frac{kL}{D_n W} \tag{1.11}$$

where L is the horizontal distance between the clamps, A' is the effective area of the grid cross section, D_n is the diameter of the spherical node at each grid junction, and W is the effective width of the cross section — W extends beyond the clamped region by one-half aperture on each side.

2.4.1 Parallel-bonded grid (biaxial)

The Tensar SS20 biaxial geogrid is modeled in the pavement-design example using the grid-set properties in Table 5. A grid section consisting of four by four apertures is clamped along its right and left edges as shown in Figure 27. The grid is subjected to a one-percent extension, and the displacement field is shown in Figure 28. The grid effective modulus is 85.4 MPa .

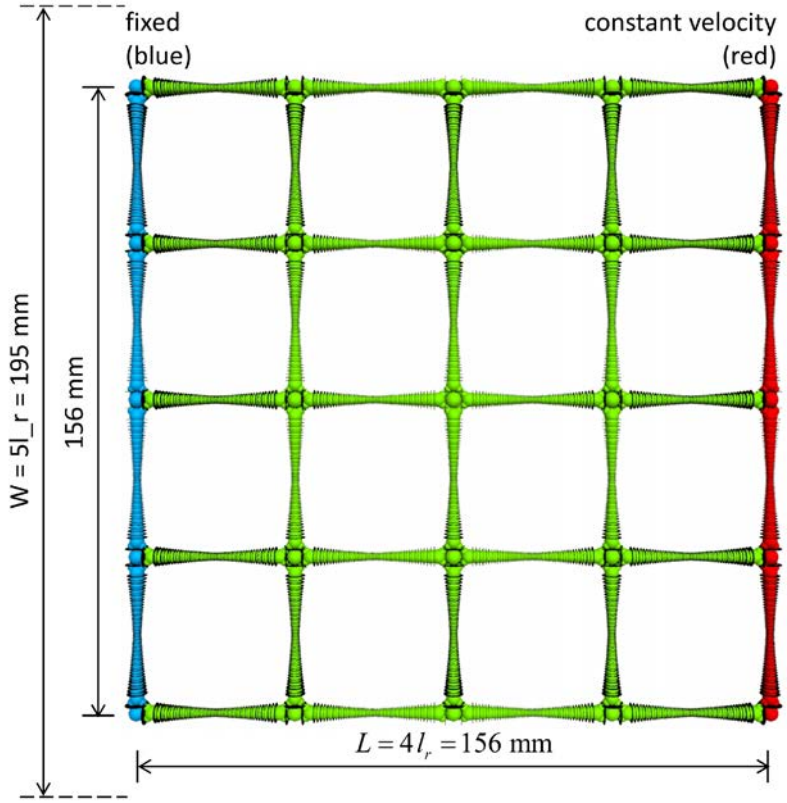

Figure 27 The SS20 parallel-bonded grid showing the boundary conditions for the MAT test.

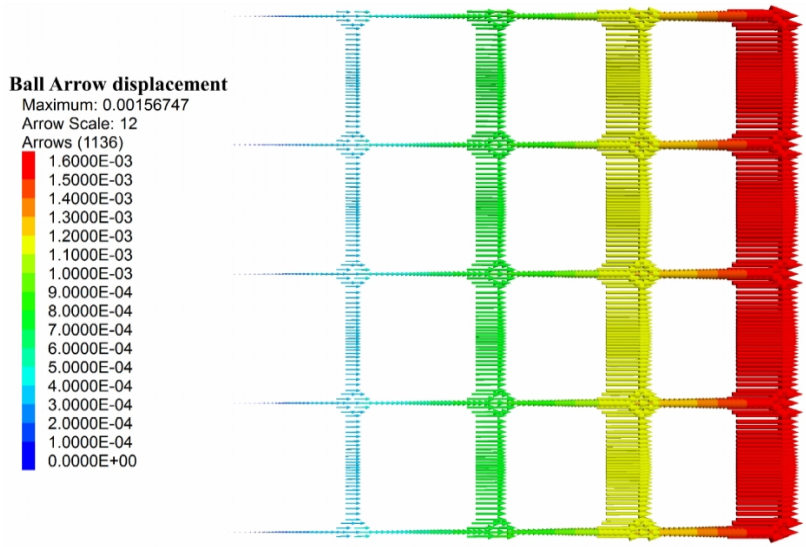

Figure 28 The displacement field of the S20 parallel-bonded grid at the end of the MAT test after application of one-percent extension.

2.4.2 Beamed grid (biaxial)

The Tensar SS20 biaxial geogrid is modeled using the grid-set properties in Table 2. A grid section consisting of four by four apertures is clamped along its right and left edges as shown in Figure 29. The grid is subjected to a one-percent extension, and the displacement field is shown in Figure 30. The grid effective modulus is 85.8 MPa , which is approximately the same as for the parallel-bonded biaxial grid. This is the expected behavior, because both grids have the same rib tensile stiffness, and it is this stiffness that is being measured in a macroscopic sense by the MAT test.

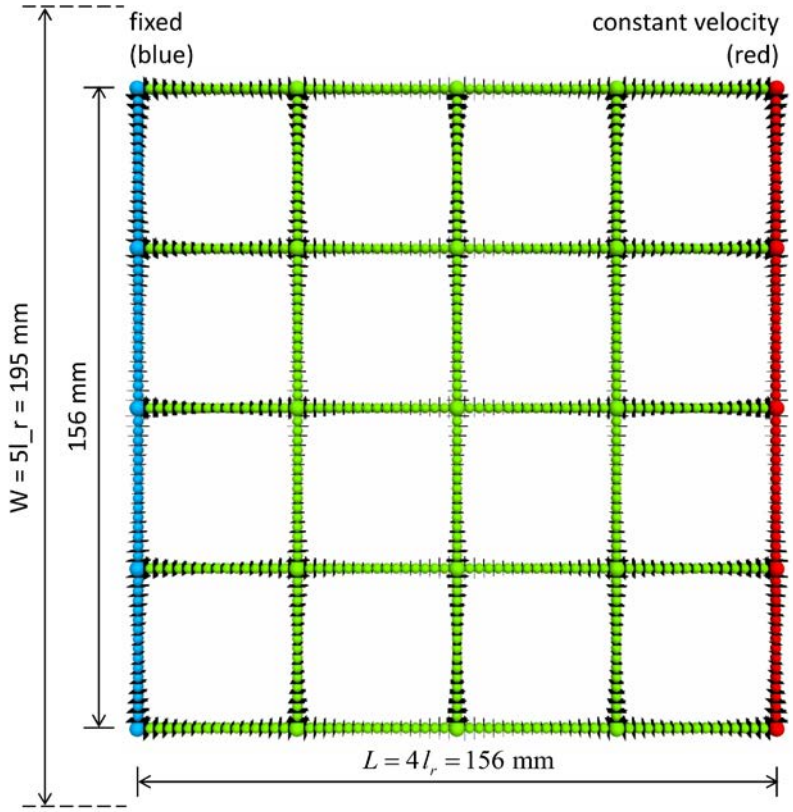

Figure 29 The SS20 beamed grid showing the boundary conditions for the MAT test.

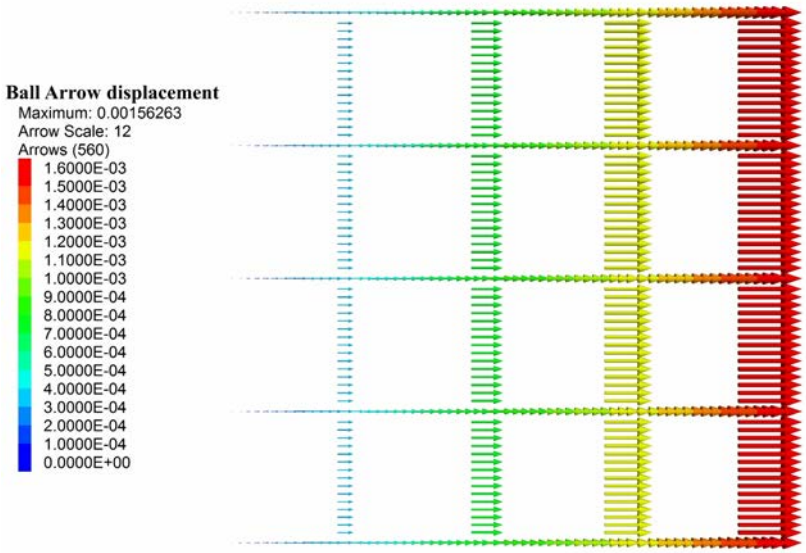

Figure 30 The displacement field of the S20 beamed grid at the end of the MAT test after application of one-percent extension.

2.4.3 Beamed grid (triaxial)

The Tensar TX160 triaxial geogrid is modeled using the grid-set properties in Table 3. A grid section consisting of six by four apertures is clamped along its right and left edges as shown in Figure 31. The grid is subjected to a one-percent extension, and the displacement field is shown in Figure 32. The grid effective modulus is 62.3 MPa , which is 27% less than the average effective modulus of the biaxial grids. The triaxial grid also displays a Poisson effect, whereby the grid contracts in the lateral direction in response to extension in the axial direction. The Poisson effect is absent for the biaxial grids. The reduced effective modulus of the triaxial grid may be related to the Poisson effect.

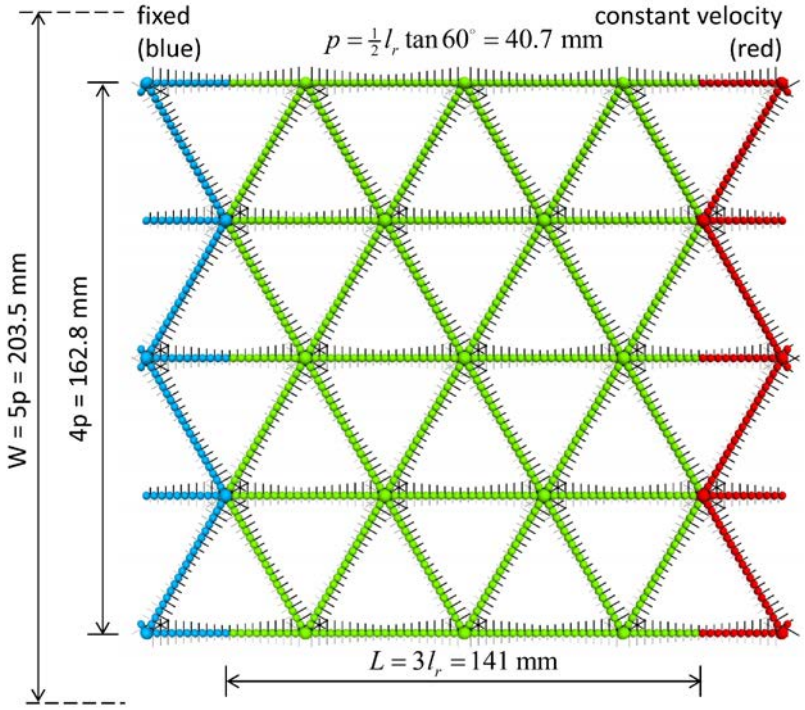

Figure 31 The TX160 beamed grid showing the boundary conditions for the MAT test.

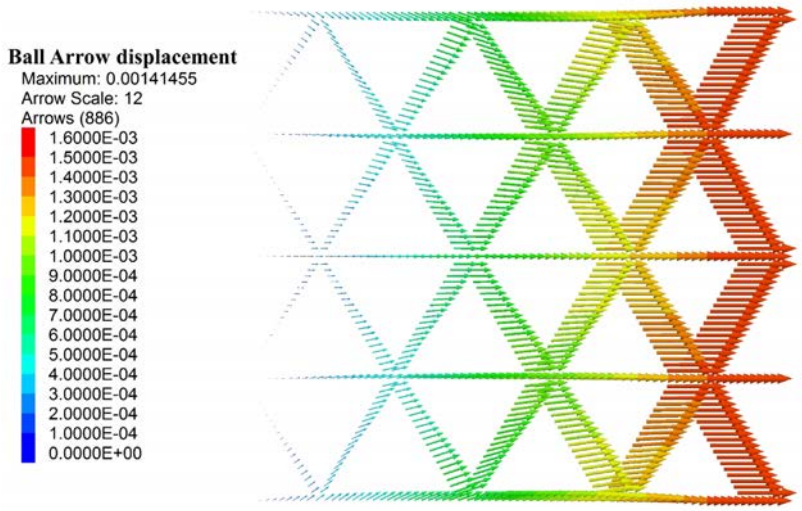

Figure 32 The displacement field of the TX160 beamed grid at the end of the MAT test after application of one-percent extension.

2.5 Grid-Embedment Procedure

The material-genesis procedure of Potyondy (2017) is modified to embed a geogrid in a granular material. The procedure occurs within a material vessel (in the form of either a polyaxial or cylindrical cell with frictionless walls) and produces a specimen consisting of a homogeneous, isotropic and well-connected grain assembly at a user-defined material pressure (P_m) with an embedded and well-interlocked grid. The procedure consists of a packing phase followed by a finalization phase. During the packing phase, the grain assembly is subjected to the boundary-contraction packing procedure during which the friction coefficient is set to μ_{CA} — typically chosen as zero to obtain a dense packing. During the finalization phase, the friction coefficient is set to its final value, μ , which is assigned to existing grain-grain contacts and new grain-grain contacts that may form during subsequent motion.

The boundary-contraction packing procedure as modified to support grid embedment consists of the following five steps (see Figure 33).

1. Create the grid set in its initial, undeformed configuration within the material vessel, and constrain the grid by fixing the grid balls so that they cannot translate or rotate. The grid remains constrained during the next three steps, during which the grid does not move or deform while the grains flow around the grid.
2. Generate a cloud of grains with grain-cloud porosity of n_c . The grains are drawn from a specified size distribution, and then placed at arbitrarily chosen positions that lie fully within the material vessel and do not overlap an exclusion region that surrounds each grid. The exclusion region is a thin layer with a normal extent that just touches the node balls; and if

the lateral extent exists ($C_e = 0$), then it just touches either the protruding half ribs or the outer node balls. There are large grain-grain overlaps in the grain cloud, but there are no grain-vessel or grain-grid overlaps. Typically, n_c is chosen equal to n_l, where n_l corresponds with the loose state for which grains are just in contact at a mean stress (σ_m) of zero. For a hill material of nearly uniform-sized spheres and no embedded grid, $n_l \cong 0.58$, and this value must be decreased to obtain a material with an embedded grid that has the same number of grains as the material with no embedded grid.

3. Set the friction coefficient to zero, and then allow the grains to rearrange until either the mean stress is near zero or static equilibrium is obtained. This step eliminates the large grain-grain overlaps by allowing the grains to move apart and flow uniformly into the grid apertures from above and below. The material is in an isotropic state at the end of this step.
4. Set the material friction coefficient to μ_{CA}, and then apply confinement by moving the vessel walls under control of a servomechanism until the wall pressures are within the specified tolerance of the material pressure and static equilibrium has been obtained. Setting $\mu_{CA} = 0$ gives the densest packing, while progressively looser packings are obtained by increasing μ_{CA}. Typically, one sets $\mu_{CA} = 0$ to allow the grains to be compressed uniformly into the grid apertures, and thereby obtain a grid that is well-interlocked with the grain assembly.
5. Remove the grid constraint by freeing the grid balls so that they can translate and rotate. Repeat step 4 on the unconstrained grid to allow the grid to move and deform in response to the compressive forces imposed by the grains.

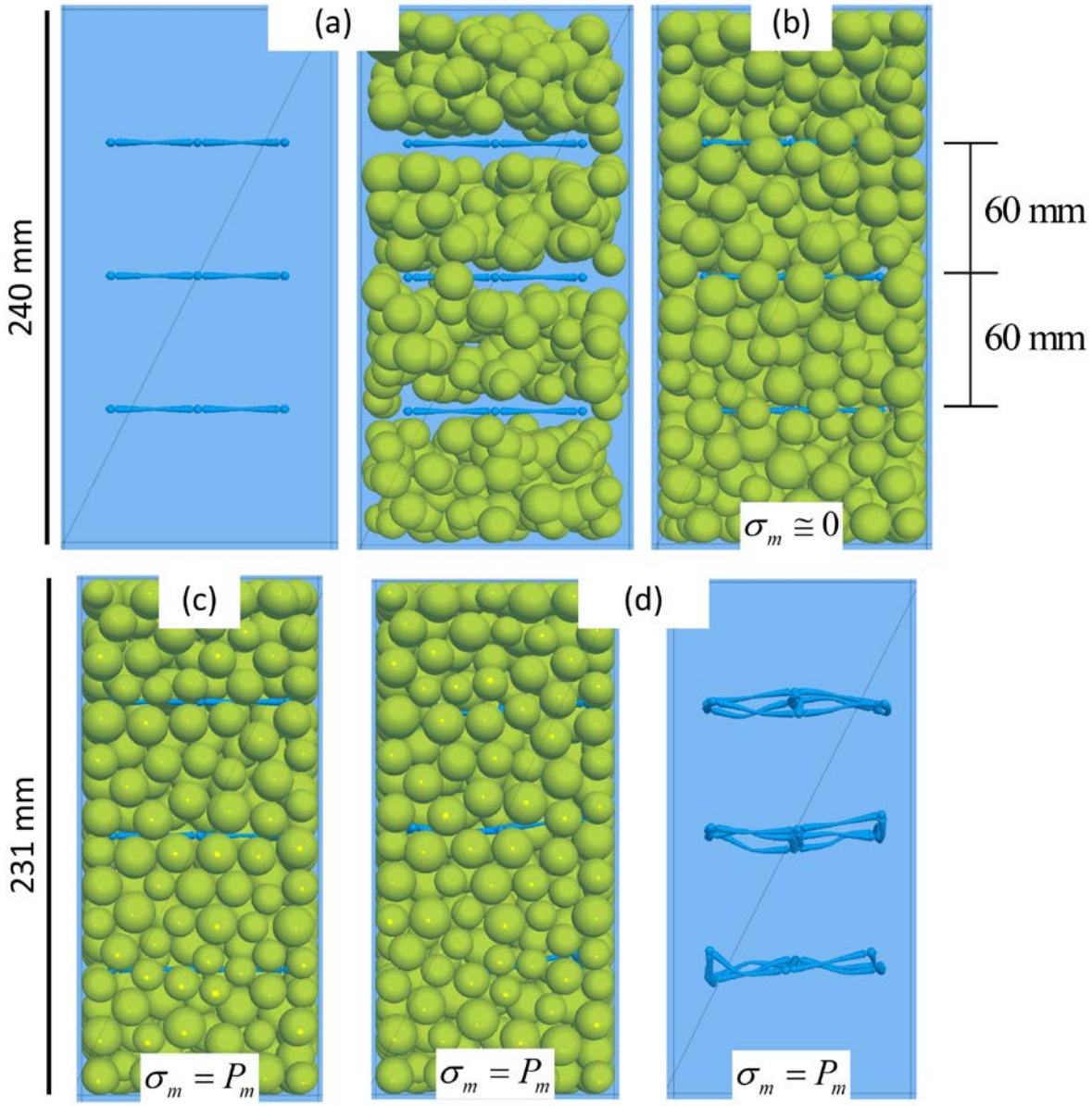

Figure 33 ***Grid-embedment procedure: (a) constrained grid and initial grain cloud at end of step 2, (b) constrained grid and relaxed grain cloud at end of step 3, (c) constrained grid and compacted granular assembly at end of step 4, and (d) unconstrained and deformed grid at end of step 5. The AG_SS20 model of the simple pavement-design example is shown in non-perspective view.***

3.0 PAVEMENT-DESIGN EXAMPLES

There are two pavement-design examples described in this section. The AG example provides a base case at the lowest resolution sufficient to demonstrate system behavior, whereas the C5Q example provides a more realistic case.[10] The AG example models a cuboid with three 2 by 2 grids containing material with a narrow grain-size distribution subjected to simple boundary conditions. The C5Q example models a cuboid with one 6 by 6 grid containing material with a broad grain-size distribution that matches the upper end of the MnDOT Class 5Q material designation subjected to boundary conditions typical of an aggregate base layer.

3.1 Simple Example

The simple pavement-design example is in the **`MG-HillGrid`** example-project directory. The example serves as a base case, and provides materials at the lowest resolution sufficient to demonstrate system behavior. Two instances of a hill material with a narrow grain-size distribution of grain diameters uniformly distributed from 14 to 20 mm are created.[11] The first instance is denoted as the AG material, and the second instance has three flat Tensar SS20 biaxial geogrids embedded within it (centered within the material vessel and oriented perpendicular to the specimen axis with a 60-mm spacing) and is denoted as the AG_SS20 material (see Figures 34 to 36). The material microproperties are listed in Table 4, and the grid-set properties are listed in Table 5. The materials are dry while being created in a polyaxial material vessel (of initial 240-mm height and 120-mm width and depth, with a 500 MPa effective modulus) and packed at a 1 MPa material pressure as shown in Figure 34.

Table 4 Microproperties of AG Materials*

Property	Value
Common group:	
N_m	$\{\text{AG}, \text{AG\_SS20}\}$
$\{T_m, N_{cm}\}$, α, C_ρ, $\rho_v \left[\text{kg/m}^3\right]$	$\{4, \text{hill}\}$, 0.7, 0, 2650
S_g, T_{SD}, $\{D_{\{l,u\}} [\text{mm}], \phi\}$, D_{mult}	0, 0, $\{14, 20, 1.0\}$, 1.0
Packing group:	

[10] A more realistic example that has been developed based on the models described herein is in the "Typical Roadway Model" section of Potyondy (2018a). The more realistic example is used to map out the modulus-porosity-grid-grain shape relationship.

[11] A hill material is defined as a granular assembly in which the hill contact model exists at all grain-grain contacts. The hill material behaves like an unsaturated granular material, and the grain-grain system behaves like two elastic spheres that may have a liquid bridge — refer to Potyondy (2016) for a comprehensive description of the model.

S_{RN}, P_m [kPa], ε_P, ε_{lim}, n_{lim}	10000, 1000, 1×10^{-2}, 8×10^{-3}, 2×10^{6}
C_p, n_c, μ_{CA}, v_{lim} [m/s]	0, {0.58,0.427},[1] 0,[2] 1.0
Hill material group:	
E_g [GPa], v_g, μ, α_h, ψ [kPa]	29, 0.15, 0.4, 0, 0

* Hill material parameters are defined in Table 2 of Potyondy (2016).

[1] The cloud porosity for the AG_SS20 material is decreased so that this material has a similar number of grains as the AG material.

[2] The friction coefficient during confinement application is zero to obtain a dense packing.

Table 5 Grid Set Properties of SS20 Parallel-Bonded Grids*

Property	Value
Grid set group:	
n_g, s_z [mm], $\{n_x,n_y\}$, $\mathbf{c}$ [mm], C_t	[3, 60.0, {3,3}, (−39.0,−39.0,−60.0), 0], AG [1, NA, {6,6}, (−97.5,−97.5,0), 0], C5
C_g, D_n [mm], l_r [mm], κ_r, n_c	0, 4.0, 39.0, 0.9, 7
$\bar{R}_n$ [mm], $\bar{R}_m$ [mm], $\bar{\lambda}_j$, C_e	2.9, 1.0, 1.0, 0, AG 1, C5
Material properties group:	
α_g, ρ_g [kg/m^3], E_g^* [MPa], κ_g^*	0.7, 950, 700,[1] 2.0
E_{gs}^* [MPa], κ_{gs}^*, μ_{gs}	500, 2.0, 0.5

* Grid-set parameters are defined in Table 1.

[1] SS20 properties in Stahl and te Kamp (2013) are 770 and 630 MPa in the TD and LD directions, respectively.

The aggregate properties are summarized as follows. There are approximately 550 granite grains modeled as spheres drawn from a narrow grain-size distribution, with grain diameters uniformly distributed from 14 to 20 mm. The grain density is 2650 kg/m^3. The Young's modulus and Poisson's ratio of the grains are 29 GPa and 0.15, respectively. The friction coefficient is 0.4. The suction is zero, because the material is dry. The damping constant is zero, because quasi-static conditions are enforced via local damping, with a local-damping factor of 0.7.

The grid material properties were taken from Stahl and te Kamp (2013). The grid density is 950 kg/m^3, which is similar to the 946 kg/m^3 for polypropylene (Wikipedia, 2015a). The grid effective modulus is 700 MPa, which is approximately one-half of the 1.5 – 2.0 GPa for

polypropylene (Wikipedia, 2015b).[12] The grid stiffness ratio is two. The structural properties of the grid (quantified by the rib tensile stiffness and the junction torsional stiffness) match those of a Tensar SS20 biaxial geogrid. The material properties of the grid surface were chosen as follows. The grid-surface effective modulus should be large enough to prevent excessive grid-grain overlap, and the value was set equal to that of the material vessel. The grid-surface stiffness ratio was set equal to the grid stiffness ratio. The grid-surface friction coefficient was set to 0.5.

The two materials at the end of material genesis are shown in Figures 34 and 35, and the configuration of a grid layer is shown in Figure 36. Both materials have approximately 550 spherical grains, with grain diameters uniformly distributed from 14 to 20 mm. The 17.0 mm average grain diameter gives a vessel resolution (number of grains across the smallest vessel dimension) of 7.1. The AG_SS20 material has a grid resolution (number of grains across a grid aperture) of 2.3. Both materials are dry, packed at a 1.0 MPa material pressure, and have a porosity of 0.379. Both materials have approximately the same number of dry hill contacts (1362 and 1328 for the AG and AG_SS20 materials, respectively), while the AG_SS20 material has an additional 2388 internal grid contacts and 421 grid-grain contacts. The internal grid contacts join the 1143 grid balls to one another via parallel bonds (denoted as grid bonds in Figure 36).

We confirm that the materials form well-connected grain assemblies at the 1 MPa material pressure by plotting the mean stress and noting that the measurement-based value has reached the wall-based value, which is equal to the 1 MPa material pressure (see Figure 37). The material with the embedded grid requires more cycles to achieve this state, and the measurement-based mean stress lags behind the wall-based value.

[12] Our value is approximately one-half that of the physical material because of the extensive parallel-bond overlinking, whereby as one proceeds along a rib, each rib ball is joined to the next two rib balls. The overlinking is removed by removing the mid-rib and tip-rib balls, and the structural properties of such a grid match those of a Tensar SS20 biaxial geogrid by setting the grid effective modulus to 1.7 GPa.

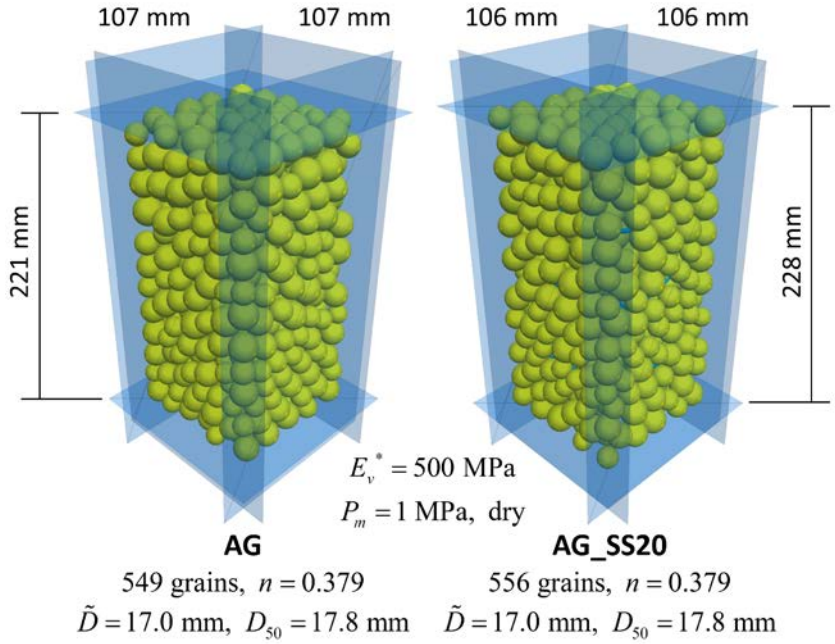

Figure 34 Dry AG and AG_SS20 materials at the end of material genesis.

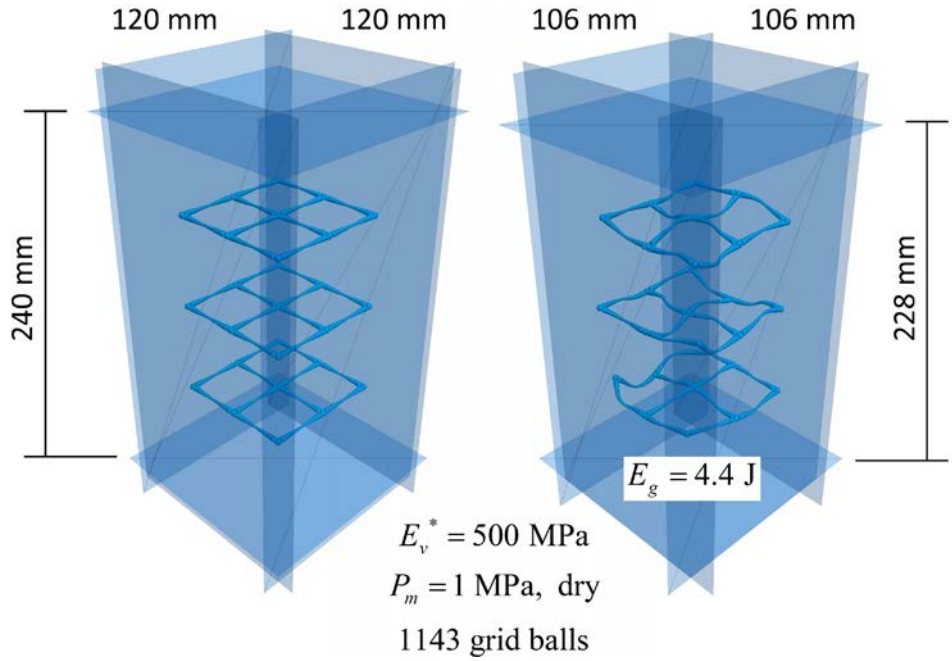

Figure 35 The embedded grid set in the AG_SS20 material in the polyaxial vessel at the start (left image) and end (right image) of material genesis.

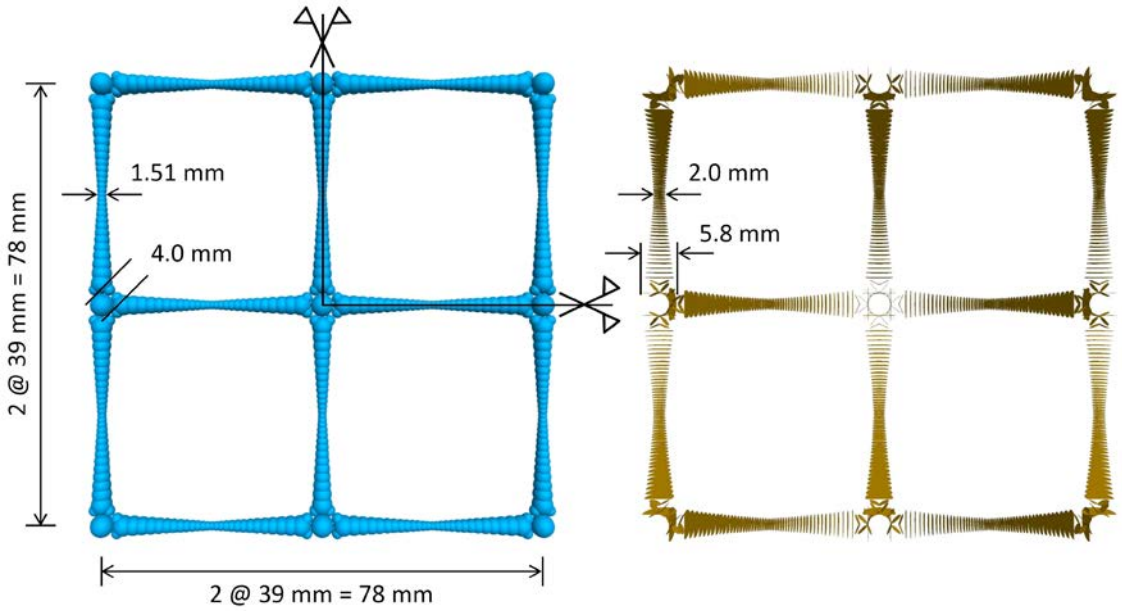

Figure 36 The undeformed configuration of a grid layer in the AG_SS20 material showing grid balls (left image) and grid bonds (right image).

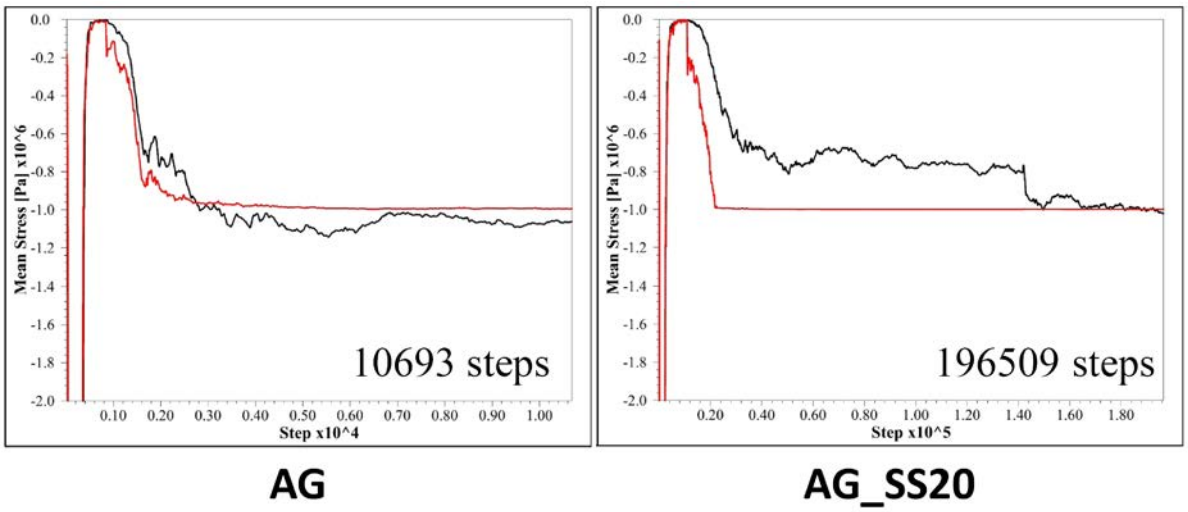

Figure 37 Mean stress acting on the boundary (red) and within the material (black) versus step for the AG and AG_SS20 materials during material genesis.

The macroscopically applied compressive load is carried by the granular material as force chains that propagate from one grain to the next across grain-grain contacts. The force-chain fabric is depicted as a network of cylinders, with a cylinder at each contact. Force magnitude corresponds with cylinder thickness and color, and force direction corresponds with cylinder orientation. An examination of the force-chain fabric at the end of material genesis reveals the following material characteristics. Both materials have a similar force-chain fabric, with maximum forces of approximately 2000 N (see Figure 38). The middle grid in the AG_SS20 material is being compressed by the grains with a maximum force of 250 N, and its front-most aperture is being loaded in tension (see Figure 39). The compressive forces acting on the grids cause them to deform, and the total strain energy stored in the three grids is 4.4 Joules (see Figure 35). If the grains were removed, and the model cycled to a new state of static equilibrium, the grids would return to their undeformed configurations.

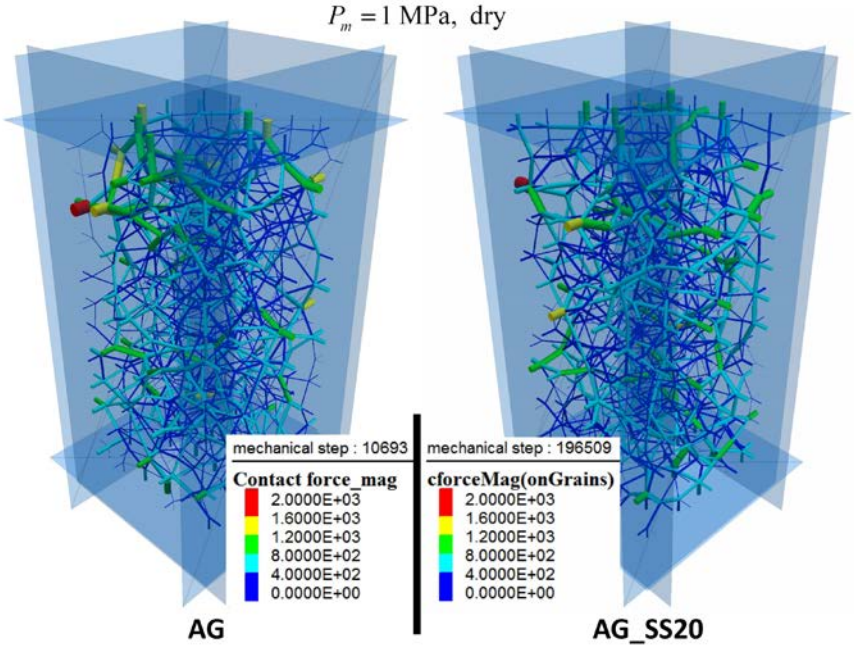

Figure 38 Force-chain fabric in the AG and AG_SS20 materials in the polyaxial vessel at the end of material genesis.

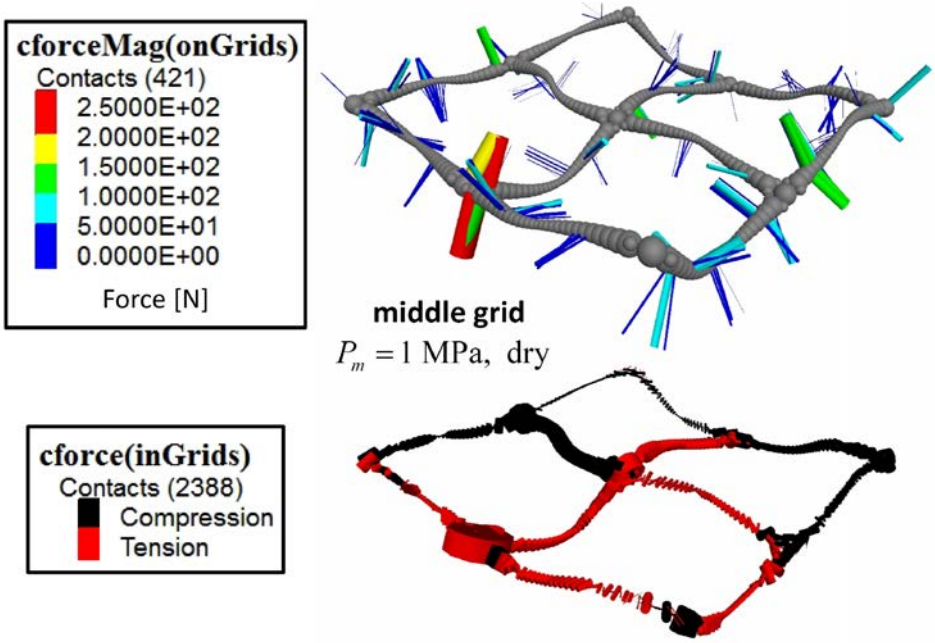

Figure 39 Forces acting on and in the middle grid in the AG_SS20 material in the polyaxial vessel at the end of material genesis.

The AG materials are subjected to triaxial testing. The materials are tested dry and wet. The wet material has a 20 kPa suction added between all grains that are within 3 mm of one another at the end of material genesis. During each triaxial test, the confinement is 1 MPa, and a load-unload cycle is performed at an axial strain of one percent to produce the deformation fields shown in Figure 40, and the stress-strain curves in Figures 41 and 42. The response is hysteretic. The grid and moisture both increase the material strength (measured as the deviator stress at one percent axial strain). The grid delays the onset of material dilation. The resilient modulus of the dry AG material with no grid is measured as 239 MPa in Figure 43, and the resilient moduli for the other cases are similar. The grid has a negligible effect on the resilient modulus of this simple system, but the grid increases the resilient modulus of the more realistic system examined in the next section.[13]

[13] A demonstration of the confining effect of the grid could be obtained by performing a cyclic triaxial test similar to the one described in Section 3.2 of McDowell et al. (2006), and examining the force chains after partial unloading. The cyclic triaxial test has 10-kPa confinement. Deviator stress is cycled 10–20 kPa (3 times), 10–30 kPa (three times), and then 10–40 kPa (three times). The partial unloading consists of reducing the confinement to 5 kPa.

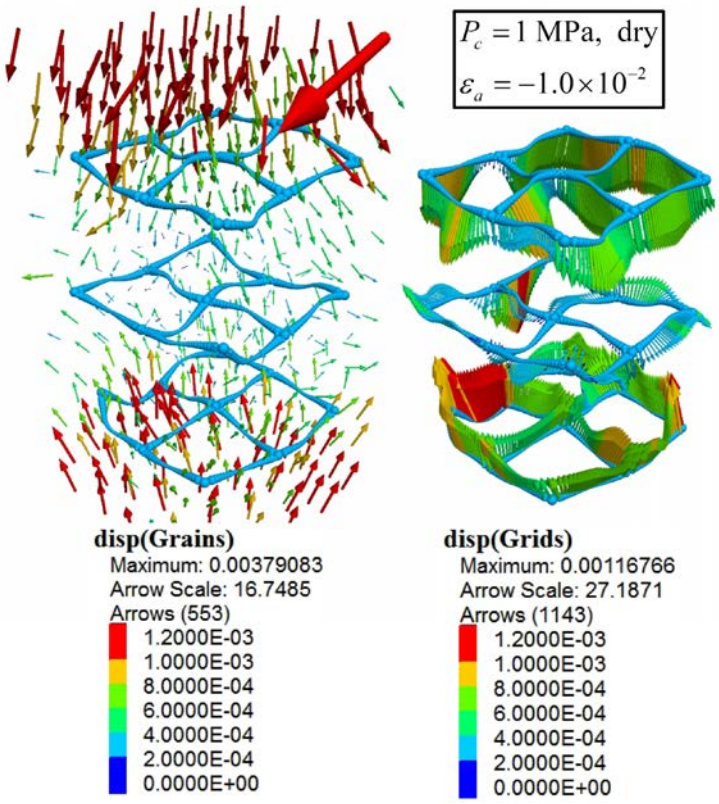

Figure 40 ***Displacement fields of the dry AG_SS20 material (left) and grid (right) after application of one percent axial strain. The top and bottom grids flow with the material and move toward one another. There is very little radial expansion to be resisted by the grids. The walls of the polyaxial vessel are not shown in these images.***

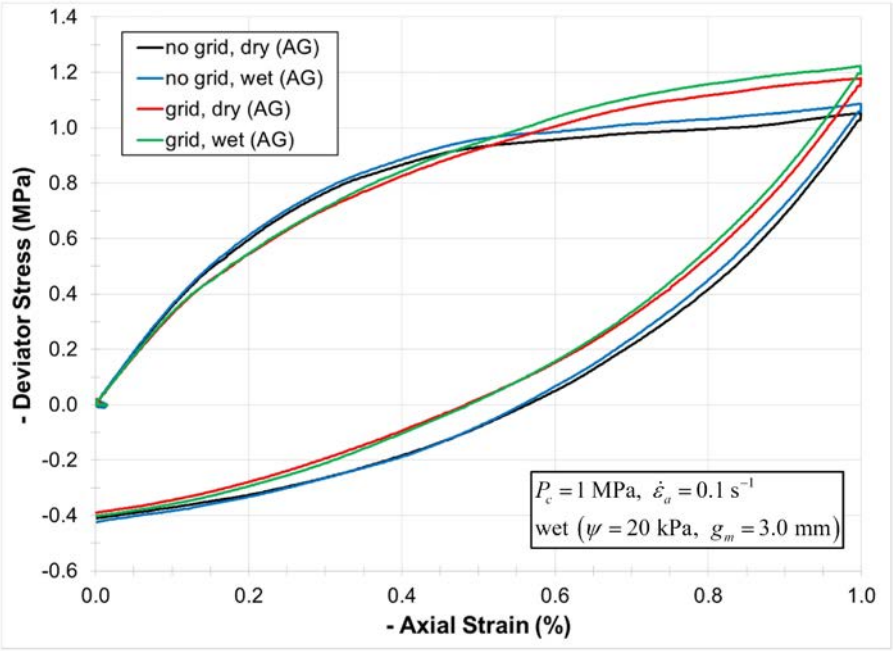

Figure 41 Deviator stress versus axial strain for dry and wet AG and AG_SS20 materials tested at 1 MPa confinement.

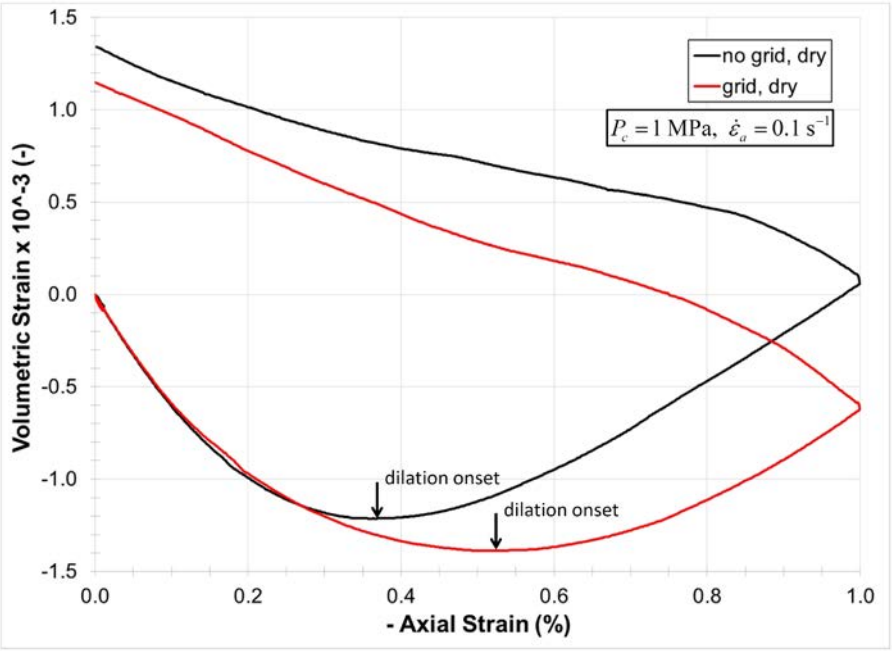

Figure 42 Volumetric strain versus axial strain for dry AG and AG_SS20 materials tested at 1 MPa confinement, and dilation onset.

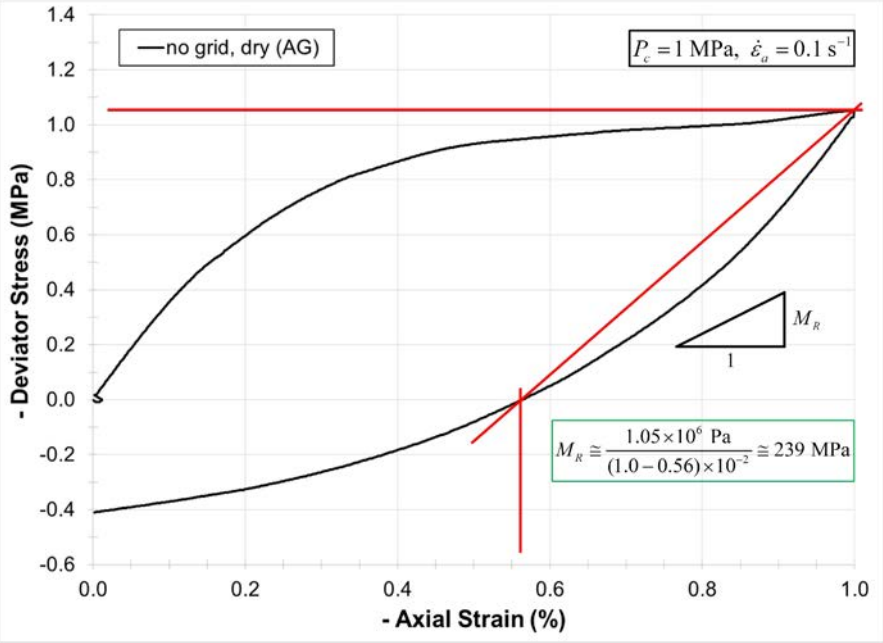

Figure 43 Deviator stress versus axial strain for dry AG material tested at 1 MPa confinement, and resilient modulus.

3.2 Realistic Example

The realistic pavement-design example is in the **`MatGen-HillGrid_C5Q`** example-project directory. Two instances of a hill material are created to represent the aggregate base layer of an asphalt-surface roadway (Potyondy et al., 2016; Siekmeier et al., 2016). The grain-size distribution lies within the upper end of the MnDOT Class 5Q aggregate base grading designation (see Figure 44). The first instance is denoted as the C5Q material, and the second instance has one flat Tensar SS20 biaxial geogrid embedded within it (centered within the material vessel and oriented perpendicular to the specimen axis) and is denoted as the C5Q_SS20 material (see Figure 45).

The C5Q materials are subjected to triaxial testing. The materials are tested dry and moist. The moist material has a 30 kPa suction added between all grains that are within 3 mm of one another at the end of material genesis.[14] During each triaxial test, the confinement is 150 kPa, and a load-unload cycle is performed at an axial strain of 0.02% to measure the resilient moduli of the dry and moist materials (see Figure 46).[15]

[14] The suction is typical for aggregates with gravimetric moisture content ranging from 5 to 10 percent.
[15] The confinement is similar to that defined in resilient modulus laboratory protocols, and axial strains correspond with vertical strains in the aggregate base layer for typical traffic loads.

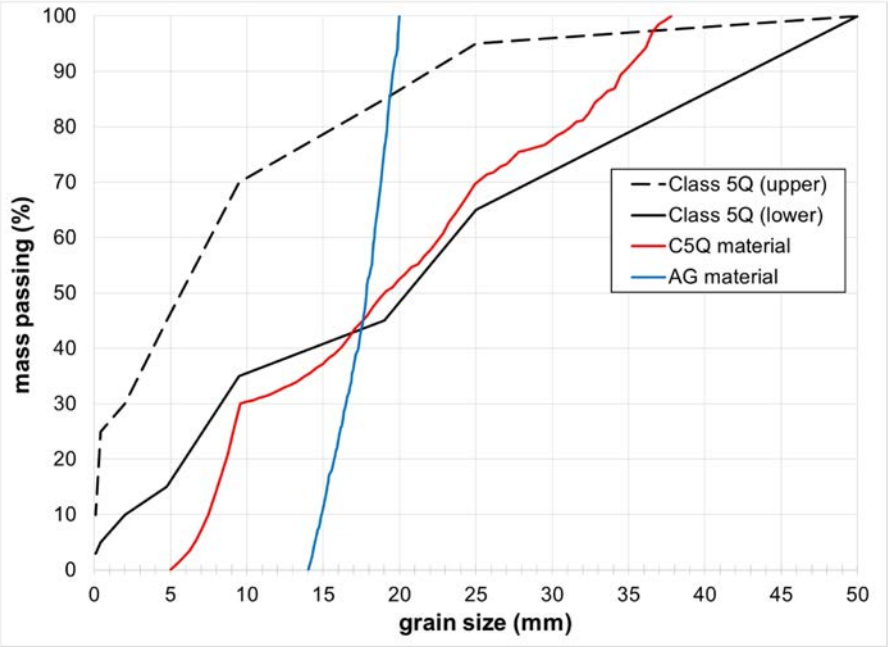

Figure 44 ***Grain size distribution curves for the C5Q and AG materials along with the limits of the MnDOT Class 5Q aggregate base grading designation.*** (Class 5Q limits from MnDOT (2016), Table 3138-3: Base and Surfacing Aggregate [containing less than 25 percent recycled aggregates].)

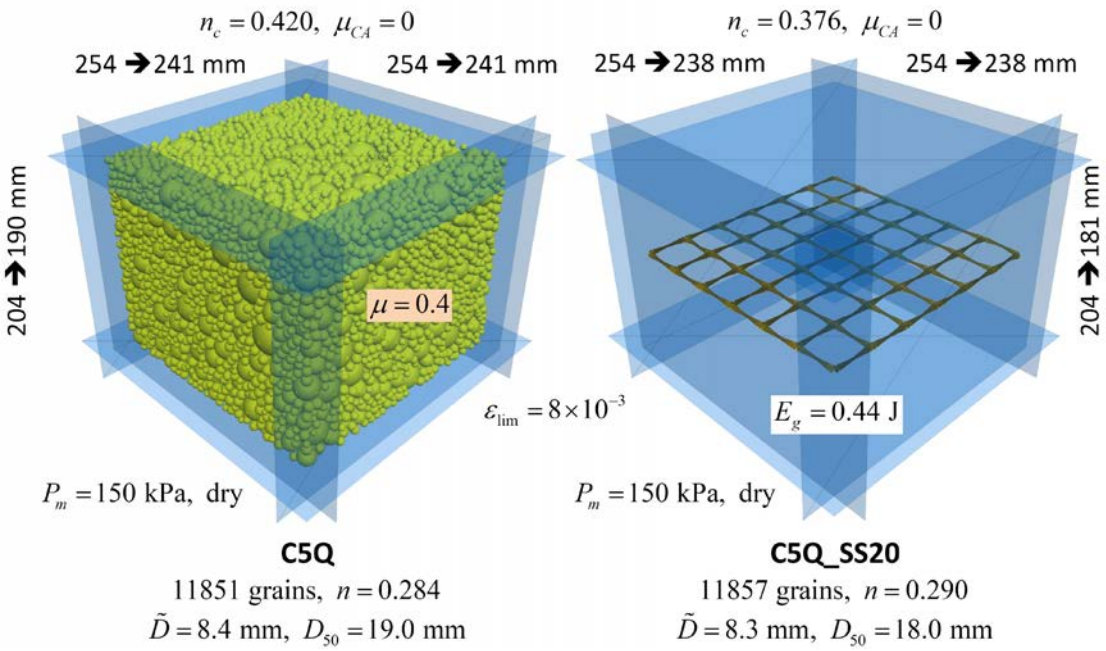

Figure 45 C5Q material and embedded grid set in the C5Q_SS20 material at the end of material genesis.

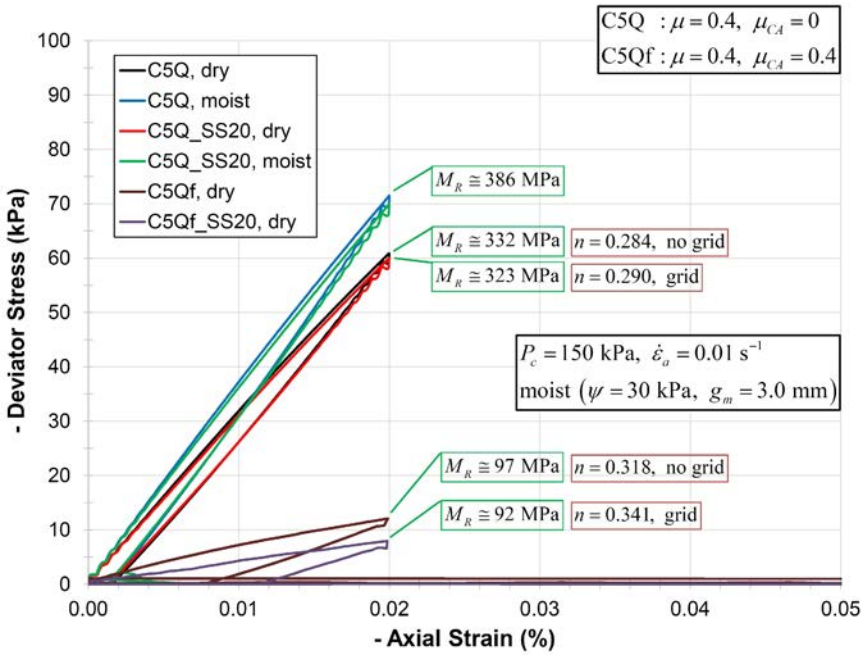

Figure 46 Deviator stress versus axial strain for dry and moist C5Q and C5Q_SS20 materials tested at 150 kPa confinement.

Adding moisture stiffens the material for both the no-grid and grid cases (increasing the resilient modulus from approximately 332 MPa to 386 MPa); however, the material stiffness is the same for the no-grid and grid cases. Why is this, and is this a general conclusion? Additional study has demonstrated that there is a general relationship between resilient modulus and material porosity, with resilient modulus decreasing as porosity increases from 0.28 to 0.35. By varying μ_{CA} from zero to the true material friction coefficient, two distinct curves are obtained, one for the no-grid model and the other for the grid model, with the no-grid curve lying beneath the grid curve (see Figure 47).[16] When μ_{CA} is non-zero, the material porosity of the no-grid specimen is less than that of the grid specimen. We speculate that the grid is inhibiting the packing process, forming a local region that is more porous than the surrounding region, and thereby increasing the overall material porosity.[17] The porosities of 0.284 and 0.290 for the case shown in Figure 46 are the lowest porosities that one can obtain for this material, because the friction coefficient has been set to zero $\left(\mu_{CA} = 0\right)$ during packing. For this case, the resilient moduli for the no-grid and grid models are approximately equal. The effect of the grid on material stiffness is found by comparing the resilient moduli for the no-grid and grid cases at the same material porosity. When this is done, we find that the presence of the grid increases the resilient modulus by factors ranging from 1.0 to approximately 2.5 depending on confinement and moisture conditions.

[16] The material shown in Figure 47 has a true material friction coefficient of 0.6. The porosity varies from the use of different friction coefficients during packing. The gain factor for a porosity of 0.323 is 1.8.

[17] The material porosity is obtained as the average value from three spherical measurement regions placed symmetrically along the axis of the largest vessel dimension (see section "Stress, Strain and Porosity in the Material" in Potyondy [2017a]).

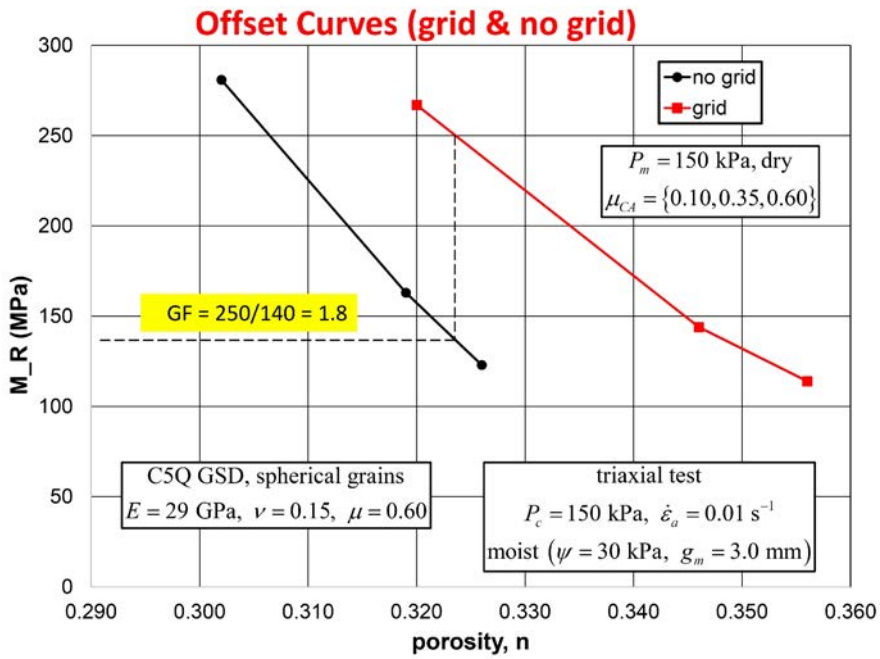

Figure 47 Resilient modulus versus porosity for grid and no-grid models with friction coefficients during packing varying from 0.1 to 0.6, and tested moist at 150 kPa confinement.

4.0 REFERENCES

Bagshaw, S.A., P.R. Herrington, P. Kathirgamanathan and S.R. Cook. (2015) "Geosynthetics in Basecourse Reinforcement," Opus International Consultants Ltd., Report to NZ Transport Agency, Wellington, New Zealand, NZ Transport Agency Research Report 574, September 2015.

Buchanan, S. (2007) "Resilient Modulus: What, Why, and How?" Vulcan Materials Company, August 31, 2007. Document **`2-Resilient-Modulus-Buchanan.pdf`** accessed from www.vulcaninnovations.com/public/pdf on November 6, 2015

Chen, C., G.R. McDowell and N.H. Thom. (2013) "A Study of Geogrid-Reinforced Ballast using Laboratory Pull-Out Tests and Discrete Element Modelling," *Geomechanics and Geoengineering*, ***8***(4), 244–253.

Clyne, T. (2001) "Monitoring Geosynthetics in Local Roadways 10-Year Performance Summary," Minnesota Department of Transportation, Saint Paul, MN, 2001.

Cook, R.D., D.S. Malkus and M.E. Plesha. (1989) ***Concepts and Applications of Finite Element Analysis***, Third Edition, New York: John Wiley & Sons.

Crandall, S.H., N.C. Dahl and T.J. Lardner. (1978) ***An Introduction to the Mechanics of Solids***, Second Edition, New York: McGraw-Hill Book Company.

Han, Z., and S.K. Vanapalli. (2016) "State-of-the-Art: Prediction of Resilient Modulus of Unsaturated Subgrade Soils," *Int. J. Geomechanics*, 10.1061/(ASCE)GM.1943-5622.0000631, 04015104.

Itasca Consulting Group, Inc. (2018) ***PFC — Particle Flow Code in 2 and 3 Dimensions***, Version 5.0, Documentation Set of version 5.00.35 [March 21, 2018]. Minneapolis: Itasca.

Jas. H., M. Stahl, H. Konietzky, L. te Kamp and T. Oliver. (2015a) "Discrete Element Simulation of Geogrid Stabilized Sub-Base: Modelling and Calibration and Plate Load Simulation under Special Consideration of Important Boundary Conditions," to appear in *Sixth Symposium on Deformation Characteristics of Geomaterials* (Buenos Aires, Argentina, November 2015).

Jas. H., M. Stahl, H. Konietzky, L. te Kamp and T. Oliver. (2015b) "Discrete Element Modeling of a Trafficked Sub-Base Stabilized with Biaxial and Multi-Axial Geogrids to Compare Stabilization Mechanisms," *Proc. Geosynthetics 2015* (Portland, OR, February 15–18, 2015), pp. 245–254.

Konietzky, H., L. te Kamp, T. Groeger and C. Jenner. (2004) "Use of DEM to Model the Interlocking Effect of Geogrids under Static and Cyclic Loading," *Numerical Modeling in*

Micromechanics via Particle Methods, pp. 3–11, Y. Shimizu, R. Hart and P. Cundall, Eds., Taylor & Francis Group, London.

McDowell, G.R., O. Harireche, M. Konietzky, S.F. Brown and N.H. Thom. (2006) "Discrete Element Modelling of Geogrid-Reinforced Aggregates," *Proceeding of the Institution of Civil Engineers — Geotechnical Engineering*, ***159***(1), 35–48.

MnDOT. (2016) ***Standard Specifications for Construction***, 2016 Edition, Minnesota Dept. of Transportation, Saint Paul, MN.

Potyondy, D. (2018a) "Model-Validation Tests," Itasca Consulting Group, Inc., Technical Memorandum 2-3558-01:17TM52 (June 22, 2018), Minneapolis, Minnesota.

Potyondy, D. (2018b) "Beam Contact Model [version 1]," Itasca Consulting Group, Inc., Technical Memorandum 2-3558-01:17TM07 (June 22, 2018), Minneapolis, Minnesota.

Potyondy, D. (2017) "Material-Modeling Support in PFC [fistPkg25]," Itasca Consulting Group, Inc., Technical Memorandum ICG7766-L (March 16, 2017), Minneapolis, Minnesota.

Potyondy, D. (2016) "Hill Contact Model [version 4]," Itasca Consulting Group, Inc., Technical Memorandum ICG7795-L (October 12, 2016), Minneapolis, Minnesota.

Potyondy, D. O. (2015) "The Bonded-Particle Model as a Tool for Rock Mechanics Research and Application: Current Trends and Future Directions," *Geosystem Engineering,* ***18***(1), 1–28.

Potyondy, D., J. Siekmeier and L. Petersen. (2016) "Aggregate-Geogrid Interaction Model Incorporating Moisture Effects," in Transportation Research Board 2016 Annual Meeting Compendium of Papers.

Qian, Y., D. Mishra, E. Tutumluer and H.A. Kazmee. (2015) "Characterization of Geogrid Reinforced Ballast Behavior at Different Levels of Degradation through Triaxial Shear Strength Test and Discrete Element Modeling," *Geotextiles and Geomembranes*, ***43***(5), 393–402.

Siekmeier, J., and J. Casanova. (2016) "Geogrid Reinforced Aggregate Base Stiffness for Mechanistic Pavement Design," Saint Paul, Minnesota, Minnesota Department of Transportation Research Report 2016-24, MN/RC 2016-24, July 2016.

Siekmeier, J., J. Bittmann, D. Potyondy and L. Petersen. (2016) "Introducing a Geogrid Gain Factor for Flexible Pavement Design," in *Proceedings University of Minnesota 64th Annual Geotechnical Engineering Conference* (Saint Paul, MN, March 4, 2016).

Skallman, J. (2010) "Geogrids (Multiaxial) on CSAH and MSAS Routes — General Specification, Granular Equivalent (G.E.) and Design Guidelines," Minnesota Dept. of Transportation, Saint Paul, MN, Tech. Memo. 10-SA-03, December 21, 2010.

Stahl, M. (2011) "Interaktion Geogitter-Boden: Numerische Simulation und Experimentelle Analyse," Ph.D. Thesis, Technische Universität Bergakademie Freiberg, Germany, Heft 2011-5 (in German).

Stahl, M., and H. Konietzky. (2011) "Discrete Element Simulation of Ballast and Gravel under Special Consideration of Grain-Shape, Grain-Size and Relative Density," *Granular Matter*, ***13***, 417–428.

Stahl, M., H. Konietzkey, L. te Kamp and H. Jas. (2014) "Discrete Element Simulation of Geogrid-Stabilised Soil," *Acta Geotechnica*, ***9***, 1073–1084.

Stahl, M., and L. te Kamp. (2013) "Project 13008: Geogrid Modelling with PFC3D — Generation and Calibration of Biaxial Geogrid SS20," Itasca Consultants GmbH, Gelsenkirchen, Germany, Report to Tensar International Ltd., United Kingdom, Report 01-2013, February 20, 2013.

Stahl, M., and L. te Kamp. (2012) "Project 12206: Geogrid Modelling with PFC3D — Generation and Calibration of TriAx-Geogrid TX160," Itasca Consultants GmbH, Gelsenkirchen, Germany, Report to Tensar International Ltd., United Kingdom, Report 01-2012, September 26, 2012.

Stille, B. (2015) "Geogrid Modeling Package," PowerPoint slide sets: **`TensarSS20-Generate&Calibrate.ppt`** and **`GeogridPackage.pptx`**.

Tanquist, B. (2012) ***MnPAVE User's Guide***. Office of Materials, Minnesota Dept. of Transportation, Maplewood, MN, July 2012.

Wikipedia. (2015a) Entry for "density polypropylene" on June 4, 2015.

Wikipedia. (2015b) Entry for "young's modulus polypropylene" on June 4, 2015.

APPENDIX C:
MODEL VALIDATION TESTS

Technical Memorandum

ITASCA
Consulting Group, Inc.

Date: June 22, 2018

To: John Siekmeier (MnDOT)

From: David Potyondy (Itasca)

Re: Model-Validation Tests

Ref: 2-3558-01:17TM52

This memo describes the model-validation tests for the MnDOT project. A typical roadway model is described, and various instances of this model are used to demonstrate the general modulus-porosity-grid-grain shape relation. The capability to perform Dynamic Cone Penetrometer (DCP) and Light Weight Deflectometer (LWD) tests on the synthetic material, both with and without grid, are also described.

TABLE OF CONTENTS

1.0 TYPICAL ROADWAY MODEL

A complete description of a typical roadway model is provided here. The roadway model has been used by Seikmeier and Casanova (2016) to compute geogrid gain factors, and by Garnica et al. (2017) to compute unsaturated gain factors. The geogrid gain factors are defined as the ratio of resilient modulus of the aggregate base with geogrid to resilient modulus of the aggregate base without geogrid. Unsaturated gain factors are defined as the ratio of resilient modulus of the aggregate base at in situ moisture/suction conditions to resilient modulus of the aggregate base near saturation (very low suction).

Garnica et al. (2017) provide the following description of this model.

> The aggregate particles are modeled as spheres with grain size distributions from 5 mm to 38 mm, which are within the MnDOT Class 5Q aggregate base grading designation (MnDOT, 2016; Tutumluer et al., 2015; Xiao and Tutumluer, 2012; Xiao et al., 2012). A "hill" material has been created as a new option in *PFC3D* to represent a typical unsaturated aggregate base. During compaction, the simulated aggregate is near saturation, but free draining (moisture surface tension between particles equal to zero) while being compacted at a stress between 100 and 200 kPa (Mooney and Rinehart, 2009; Rinehart and Mooney, 2009). Then moisture surface tension is added between the aggregate particles before performing the cyclic triaxial tests. Axial strains in the *PFC3D* model correspond with the vertical strains in the aggregate base layer calculated using MnPAVE for the expected traffic loads (Tanquist, 2012). The confining stresses are similar to those defined by resilient modulus laboratory protocols (NCHRP 1-28A, 2003).
>
> During the cyclic triaxial tests simulated using the *PFC3D* distinct element model, twelve load cycles were performed at axial strains of 0.02% (four cycles), 0.05% (four cycles), and 0.10% (four cycles) to estimate three strain-dependent resilient moduli (see Figure 1).
>
> . . . moisture is defined in terms of moisture tension stress based on suction measurements of typical natural and recycled aggregates in Minnesota (Gupta et al., 2007; Gupta et al., 2005). These moisture tensions [suction (ψ) ranging from 1 to 60 kPa] are in the range measured for aggregates at gravimetric moisture contents of about 5 to 10 percent. The moisture contact gap notation [moisture gap (g_m)] refers to distinct element model test cases where moisture tension was extended to aggregate particles separated by a gap of 1 to 10 mm in order to simulate the inclusion of sand-sized particles, which partially fill the gaps between the larger aggregate particles in the in situ aggregate layer being simulated in the distinct element model. Sand-sized particles (less

than 5 mm) are not currently included in the distinct element model due to computer processor speed limitations.

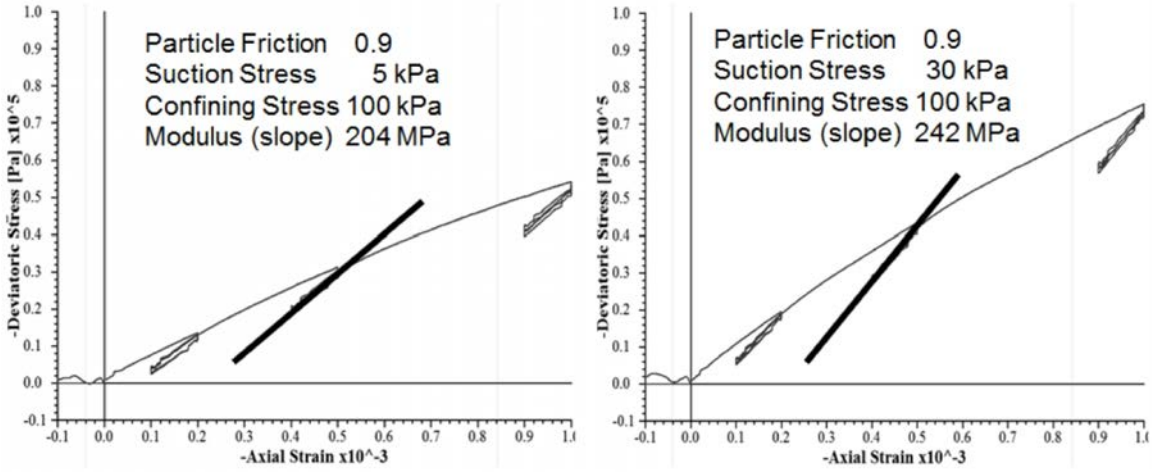

Figure 1 ***Cyclic triaxial simulations showing increased modulus with increased suction.*** (From Fig. 5 of Garnica et al. [2017])

The roadway model is in the **`MatGen-HillGrid_5Q`** example-project directory. Two instances of a hill material are created to represent the aggregate base layer of an asphalt-surface roadway. The aggregate grains are modeled as granite spheres with a grain-size distribution that lies within the upper end of the MnDOT Class 5Q aggregate base grading designation (see Figure 2).[1] The first instance is denoted as the 5Q material, and the second instance has one flat Tensar SS20 biaxial geogrid embedded within it and is denoted as the 5Q_SS20 material (see Figure 3).[2] The material microproperties are listed in Table 1, and the grid-set properties are listed in Table 2.[3] The materials are dry while being created in a polyaxial material vessel (initially 160-mm high and 265-mm wide and deep)[4] and packed at a 150 kPa material pressure. The materials are subjected to triaxial testing.[5]

[1] The grains are assigned properties of granite: density of 2650 kg/m^3, Young's modulus of 29 GPa, Poisson's ratio of 0.15 and friction coefficient of 0.6.

[2] The grid is assigned properties of polypropylene: density of 946 kg/m^3, Young's modulus of 1.2 GPa, and Poisson's ratio of 0.42. The ribs of the beamed grid are rectangular with a height of 3.5 mm, and a width that varies exponentially from 5.0 to 2.0 mm from the rib junction to mid rib. The grid surface is assigned a friction coefficient of 0.5. The grid with these properties matches the rib tensile stiffness and junction torsional stiffness of a Tensar SS20 biaxial grid.

[3] The parallel-bonded grid with properties listed in Table 3 gives the same resilient modulus as the beamed grid.

[4] There are approximately 8400 grains.

[5] The results presented here were produced using equilibrium-ratio limits of 8×10^{-3} and 1×10^{-5} during packing and compression-test seating, respectively. When the equilibrium-ratio limit during packing was decreased to 1×10^{-5}, the

The materials are tested moist. The moist materials have a 30 kPa suction added between all grains that are within 3 mm of one another at the end of material genesis. During each triaxial test, the confinement is 150 kPa, and a load-unload cycle is performed at an axial strain of 0.02% to measure the resilient modulus (see Figure 4).

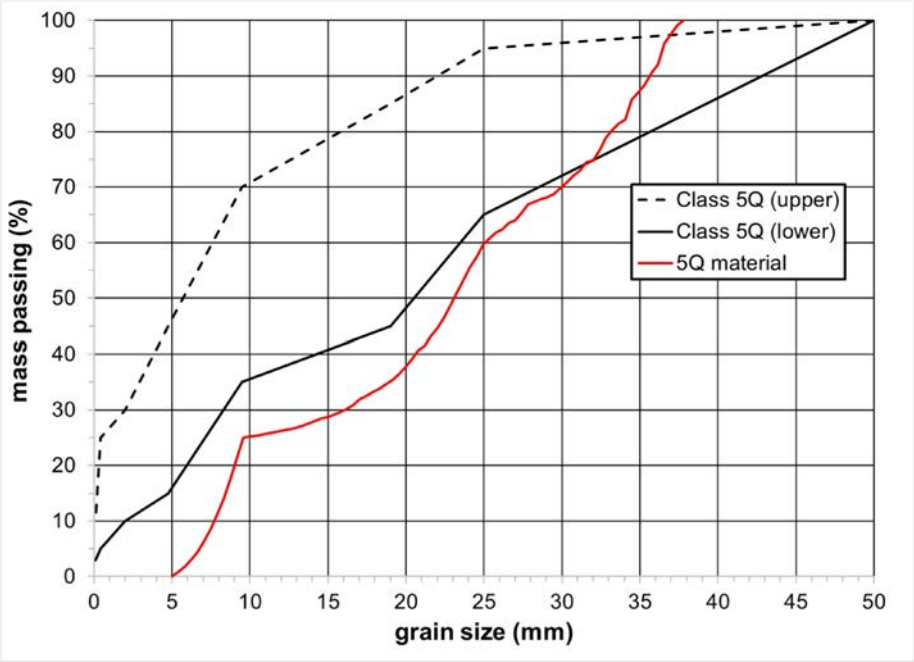

Figure 2 ***Grain size distribution curves for the 5Q material along with the limits of the MnDOT Class 5Q aggregate base grading designation.***[6] (Class 5Q limits from MnDOT (2016), Table 3138-3: Base and Surfacing Aggregate [containing less than 25 percent recycled aggregates])

model required 8 times more packing steps with a corresponding 1.3% decrease in material porosity, which caused the resilient modulus to increase by 11%. These effects are deemed sufficiently small to be neglected during typical model runs. The decrease of the equilibrium-ratio limit during packing did not affect the internal mean stress that was obtained at the end of packing, and for most no-grid models, the internal mean stress was 40% larger than the mean stress measured via forces acting on the material-vessel walls. Note that the specified material pressure matches the wall-based mean stress. We speculate that the boundary stress is lower, because a non-uniform stress state has become locked into the material. The shear stresses are no longer small relative to the direct stresses; thus, the stress state is not well characterized by mean stress. There is a complex, non-uniform stress state, which is representative of a real granular material. This effect should be studied in future work.

[6] The match of the Class 5Q grading designation can be improved by modifying the volume fractions to $\{0.3, 0.2, 0.2, 0.3\}$ for the four diameter ranges. Doing this increases the number of grains from approximately 8400 to 10150, and improves the match such that the synthetic material is within the grading range for grain sizes greater than 17 mm. Improving the match increases the material porosity by 4.4%, and has a negligible effect on measured resilient moduli.

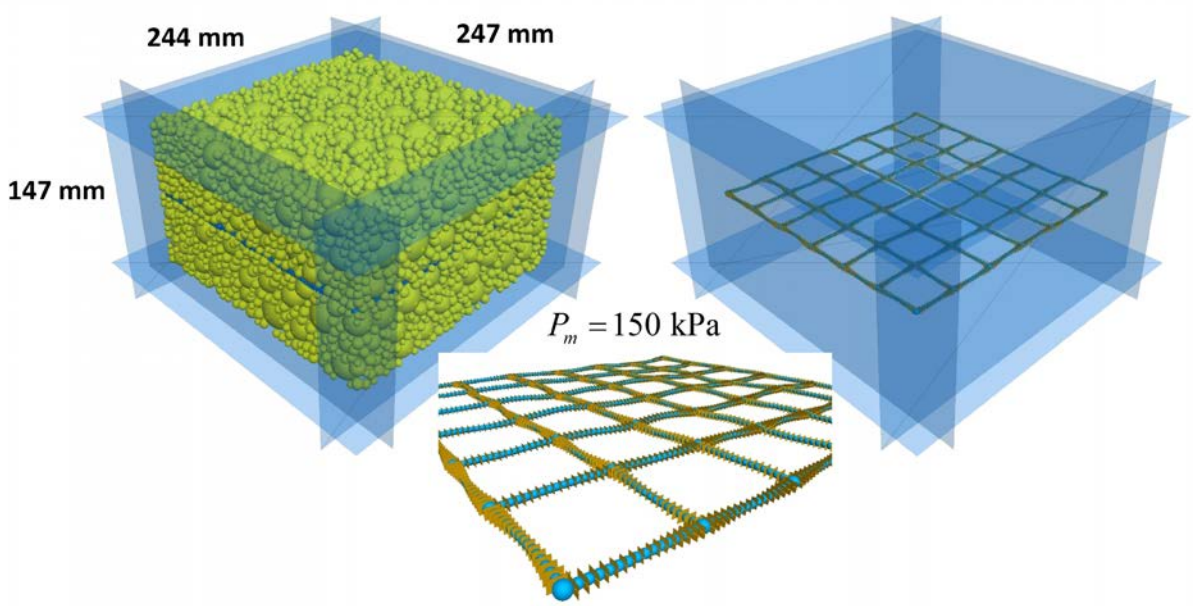

Figure 3 ***The 5Q_SS20 material at the end of material genesis showing grains and grid (left image) and deformed grid (middle and right images).***

Table 1 Microproperties of 5Q Materials*

Property	Value
Common group:	
N_m	$\{5Q, 5Q\_SS20\}$
$\{T_m, N_{cm}\}$, α, C_ρ, $\rho_v\,[\mathrm{kg/m^3}]$	$\{4, \mathrm{hill}\}$, 0.7, 0, 2650
S_g, n_{SD}, T_{SD}, D_{mult}	0, 4, 0, 1.0
$\{D_{\{l,u\}}\,[\mathrm{mm}],\ \phi\}^{(j)}$	$\{25.0, 38.0, 0.4\}^{(1)}$ $\{19.0, 25.0, 0.25\}^{(2)}$ $\{9.5, 19.0, 0.1\}^{(3)}$ $\{5.0, 9.5, 0.25\}^{(4)}$
Packing group:	
S_{RN}, $P_m\,[\mathrm{kPa}]$, ε_P, $\varepsilon_{\mathrm{lim}}$, n_{lim}	10000, 150, 1×10^{-2}, 8×10^{-3}, 2×10^{6}
C_p, n_c, μ_{CA}, $v_{\mathrm{lim}}\,[\mathrm{m/s}]$	0, $\{0.42, 0.37\}$,[1] 0.35[2], 1.0
Hill material group:	
$E_g\,[\mathrm{GPa}]$, ν_g, μ, α_h, $\psi\,[\mathrm{kPa}]$	29, 0.15, 0.6, 0, 0

* Hill material parameters are defined in Table 2 of Potyondy (2016).

[1] The cloud porosity for the grid model is decreased to obtain a similar number of grains as the no-grid model.

[2] Materials with increasing porosities are obtained by varying this parameter from 0.1 to 0.6.

Table 2 Grid Set Properties of SS20 Beamed Grid*

Property	Value
Grid set group:	
$n_g,\ \{n_x,n_y\},\ \mathbf{c}\,[\mathrm{mm}],\ C_t$	$1,\ \{7,7\},\ (-117.0,-117.0,0),\ 0$
$C_g,\ D_n\,[\mathrm{mm}],\ l_r\,[\mathrm{mm}],\ D_m\,[\mathrm{mm}]$	1, 4.0, 39.0, 2.5
$b_n\,[\mathrm{mm}],\ b_m\,[\mathrm{mm}],\ h_n\,[\mathrm{mm}],\ h_m\,[\mathrm{mm}],\ C_e$	5.0, 2.0, 3.5, 3.5, 0
Material properties group:	
$\alpha_g,\ \rho_g\left[\mathrm{kg/m^3}\right],\ E_g\,[\mathrm{GPa}],\ \nu_g$	0.7, 950, 1.2, 0.42
$E_{gs}^*\,[\mathrm{MPa}],\ \kappa_{gs}^*,\ \mu_{gs}$	500, 2.0, 0.5

* Grid-set parameters are defined in Table 1 of Potyondy (2018).

Table 3 Grid Set Properties of SS20 Parallel-Bonded Grid*

Property	Value
Grid set group:	
$n_g,\ \{n_x,n_y\},\ \mathbf{c}\,[\mathrm{mm}],\ C_t$	$1,\ \{7,7\},\ (-117.0,-117.0,0),\ 0$
$C_g,\ D_n\,[\mathrm{mm}],\ l_r\,[\mathrm{mm}],\ \kappa_r,\ n_c$	0, 4.0, 39.0, 0.9, 7
$\bar{R}_n\,[\mathrm{mm}],\ \bar{R}_m\,[\mathrm{mm}],\ \bar{\lambda}_j,\ C_e$	2.9, 1.0, 1.0, 0
Material properties group:	
$\alpha_g,\ \rho_g\left[\mathrm{kg/m^3}\right],\ E_g^*\,[\mathrm{MPa}],\ \kappa_g^*$	0.7, 950, 700, 2.0
$E_{gs}^*\,[\mathrm{MPa}],\ \kappa_{gs}^*,\ \mu_{gs}$	500, 2.0, 0.5

* Grid-set parameters are defined in Table 1 of Potyondy (2018).

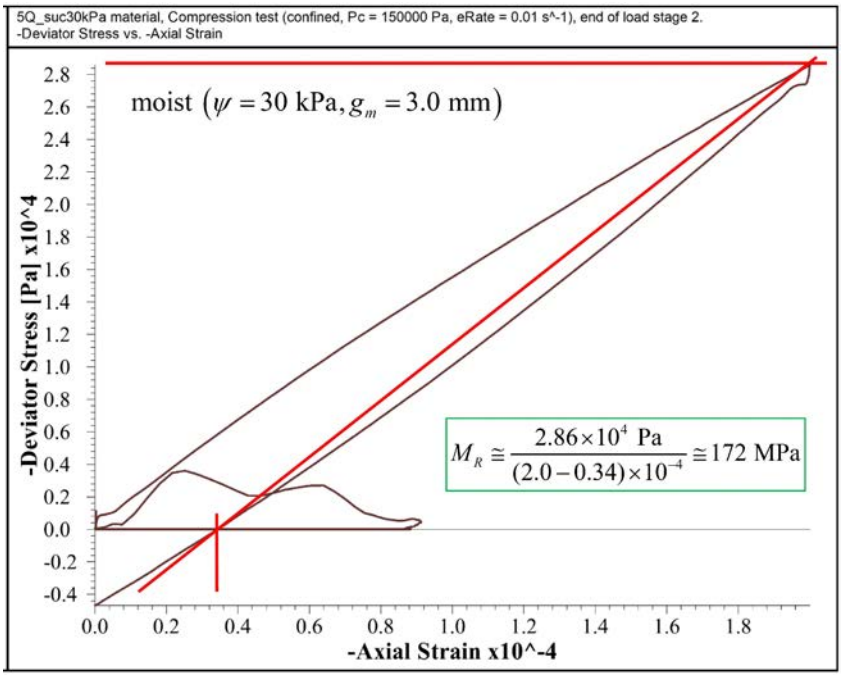

Figure 4 Deviator stress versus axial strain for 5Q material (n = 0.314) tested moist at 150 kPa confinement, and resilient modulus.

The following results demonstrate that there is a general relation between resilient modulus and material porosity, with resilient modulus decreasing as porosity increases. By varying the friction coefficient during packing (μ_{CA}) from 0.1 to the true material friction coefficient (taken here as 0.6), two distinct curves are obtained, one for the no-grid model and the other for the grid model, with the no-grid curve lying beneath the grid curve (see Figure 5). For a given μ_{CA} , the material porosity of the no-grid specimen is less than that of the grid specimen. We speculate that the grid is inhibiting the packing process, forming a local region that is more porous than the surrounding region, thereby increasing the overall material porosity. The effect of the grid on material stiffness is found by comparing the resilient moduli for the no-grid and grid cases at the same material porosity. When this is done, we find that the presence of the grid increases the resilient modulus by factors ranging from 1.0 to approximately 2.5, depending on confinement and moisture conditions.

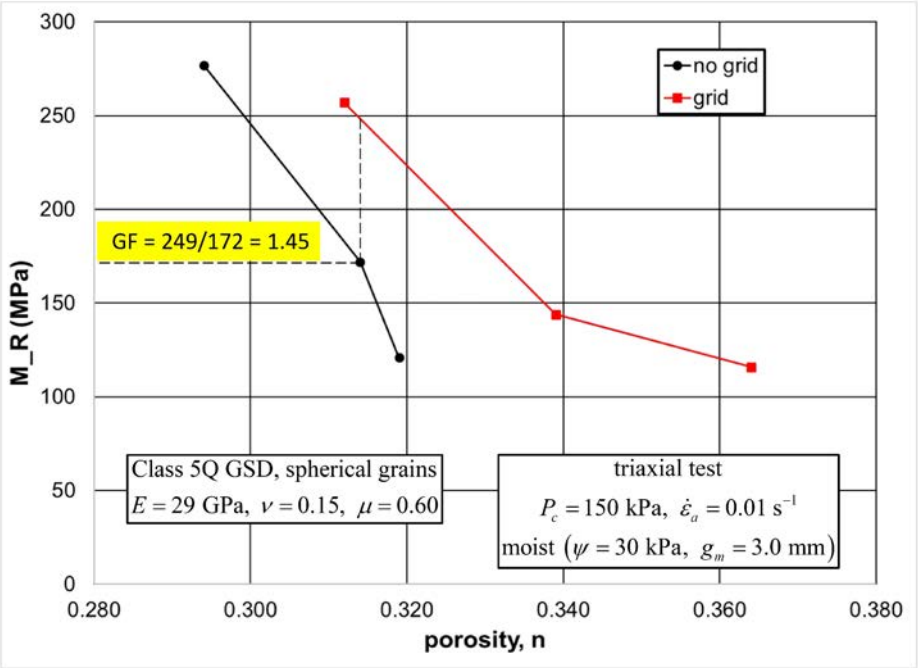

Figure 5 Resilient modulus versus porosity for grid and no-grid models, tested moist at 150 kPa confinement.

The effect of grain shape is studied by replacing the spherical grains of the roadway model with dyad-shaped grains (see Figure 6). The grain-size distribution of the all-dyad material is similar to that of the all-sphere material. The modulus-porosity-grid-grain shape relations are shown in Figure 7. The results are summarized as follows.

- The all-dyad material has a larger resilient modulus than the all-sphere material.
- For the same grain shape, the grid curve lies above the no-grid curve; thus, gain factors are greater than one.
- The presence of the grid causes the material to pack to a less dense state.
- The all-dyad material packs to a wider porosity range than the all-sphere material.
- For the same μ_{CA}, the all-dyad material packs to a less dense state than the all-sphere material.

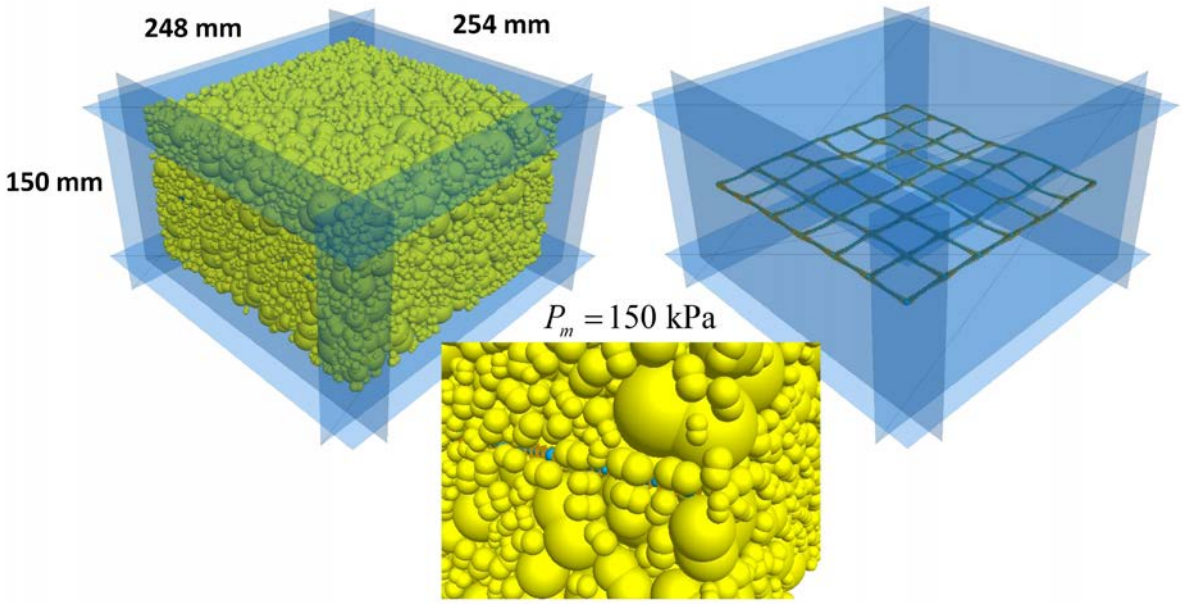

Figure 6 ***The 5Q_SS20 material with all-dyad grains at the end of material genesis showing grains and grid (left and middle images), and deformed grid (right image).***

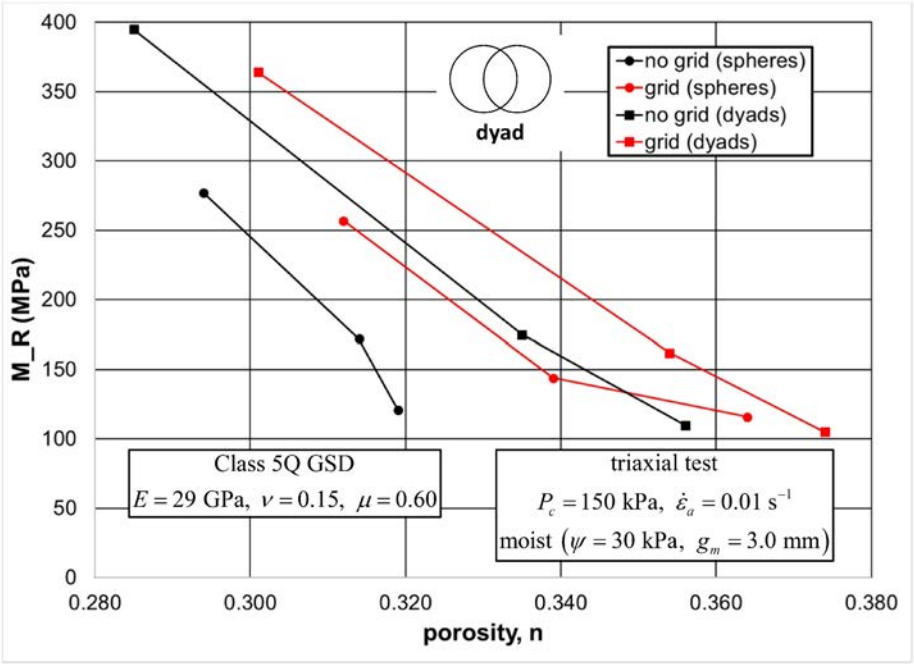

Figure 7 ***Resilient modulus versus porosity for grid and no-grid models of all-spheres and all-dyads, tested moist at 150 kPa confinement.***

2.0 DCP AND LWD PROBES

The capability to perform Dynamic Cone Penetrometer and Light Weight Deflectometer tests on the synthetic material are described here. The physical DCP and LWD tests are described in the first and second subsections. The simulated DCP and LWD tests can be performed on the material within a triaxial cell. The simulated tests are termed "probes," because they allow one to probe the state of the material under various boundary conditions, including the boundary conditions of a triaxial test. The probe model is described in the third subsection. A simple example of the DCP and LWD probe capability is provided in the final subsection.

2.1 Dynamic Cone Penetrometer Test

The Dynamic Cone Penetrometer (DCP) test is used to characterize the granular aggregate in the base layer of an asphalt pavement by measuring penetration to provide an estimate of the material shear strength and modulus. The DCP test is a performance-related construction quality assurance test. The simulated DCP test is based on the DCP device as specified by the Minnesota Department of Transportation (see Figures 8 and 9), and described in Yohannes et al. (2009), Siekmeier et al. (2009), and ASTM (2015). The main components of the DCP are a cone-tipped rod, to which is attached an anvil and drop hammer. The DCP is placed on the ground surface, and oriented vertically. After some initial penetration caused by the weight of the device, the hammer is raised to a fixed height above the anvil, and then released. The hammer strikes the anvil, which drives the rod into the ground. A series of hammer drops is performed, and for each drop the penetration per blow (DCP Penetration Index, DPI) is measured. The DPI is used to estimate the shear strength and modulus of unbound materials using empirical relations (Siekmeier et al., 2009).

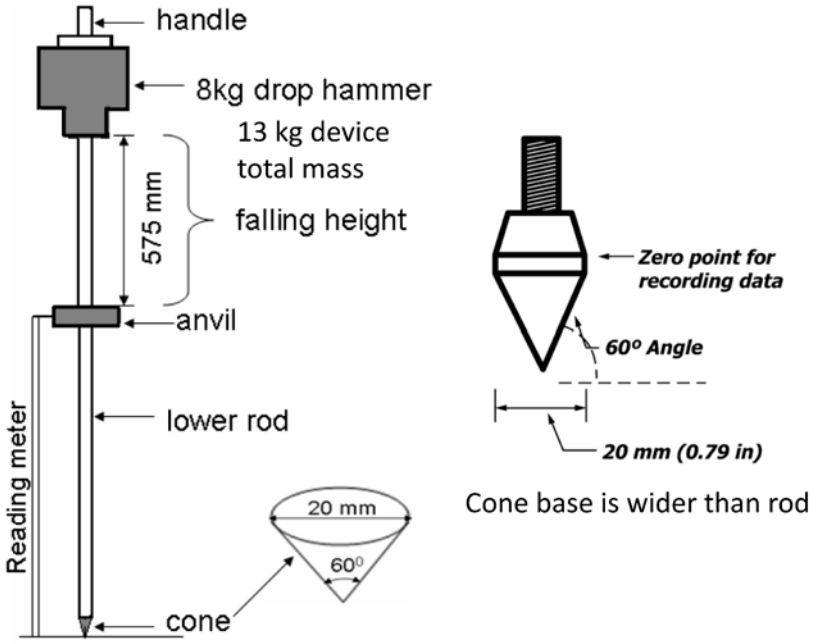

Figure 8 ***Sketch of DCP device and detail of cone tip.*** (From Fig. 1.4 of Yohannes et al. [2009] and Fig. 2 of ASTM [2015])

Figure 9 ***Dynamic Cone Penetrometer as used in the field.*** (From Fig. 1.1 of Siekmeier et al. [2009])

2.2 Light Weight Deflectometer Test

The Light Weight Deflectometer (LWD) test is used to characterize the granular aggregates in the base layer of an asphalt pavement by measuring surface deflection to provide an estimate of the material modulus. The LWD test is a performance-related construction quality assurance test. The simulated LWD test is based on the LWD device as specified by the Minnesota Department of Transportation (see Figures 10 & 11), and described in Davich et al. (2006), Siekmeier et al. (2009), and ASTM (2007). The LWD device induces a material response by dropping a weight onto a plate resting on the test layer. A load cell within the device measures the time history of the load pulse, and a geophone suspended through the bottom plate measures the time history of the material displacement (see Figure 12). The peak load and peak displacement are used to calculate modulus (Siekmeier et al., 2009, Eq. 1.6). The LWD directly measures the quantities of force and displacement that constitute pavement loading. MnDOT now specifies that a peak force of 6.28 kN be delivered to the ground by a 200 mm diameter plate, which corresponds with a 200 kPa peak stress being applied to the material.

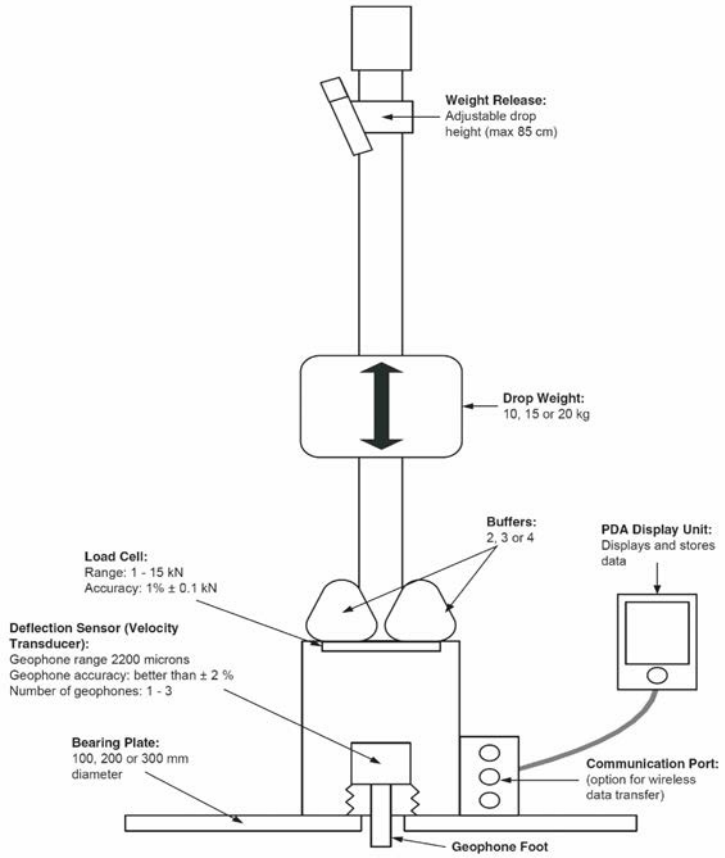

Figure 10 Sketch of LWD device. (From Fig. 1 of Fleming et al. [2007])

Figure 11 ***Light Weight Deflectometer as used in the field.*** (From Fig. 1.2 of Siekmeier et al. [2009])

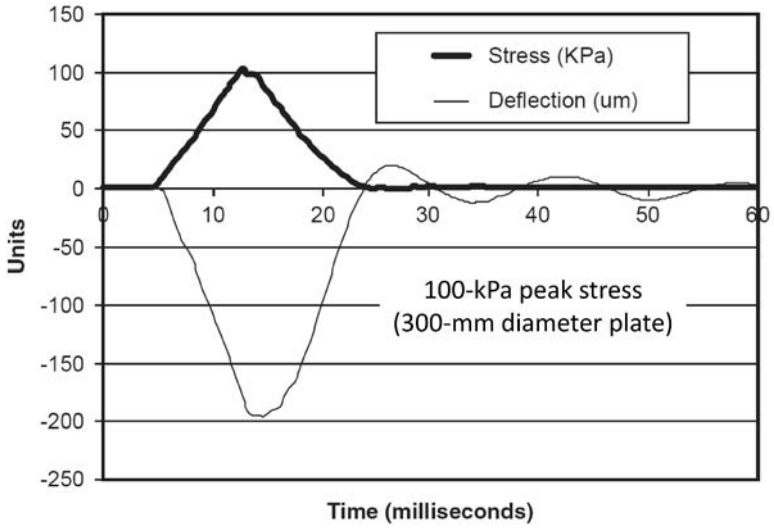

Figure 12 ***Example of LWD output from test on 400 mm of well-graded crushed granodiorite.*** (From Fig. 2 of Fleming et al. [2007])

2.3 Probe Model

The DCP and LWD models described herein are like the models of Tan et al. (2014), with the primary difference being the use of a *PFC* clump[7] to model the rod/plate — Tan et al. (2014) model the rod/plate as a collection of walls.[8] In both models, a dropping hammer is not modeled. Instead, a time-varying external force is applied to the rod/plate.[9] Another difference in the models is the material-genesis procedure. In the models described herein, a cloud of overlapping grains is created within a vessel and allowed to rearrange under conditions of zero gravity and zero friction. A friction coefficient is then specified, and the vessel boundary is moved inward to obtain a specified material pressure. The true material friction coefficient is then assigned to the material. In the model of Tan et al. (2014), columns of grains are generated within a vessel, assigned arbitrary initial velocities, and allowed to rearrange under the influence of gravity. The material is then compacted by repeatedly dropping a weighted plate onto its surface. The true material friction coefficient is used during the entire procedure.

The probe model simulates a DCP or LWD test that is performed on the material in either the polyaxial or cylindrical cell during a triaxial test. The probed system is shown in Figure 13. The material is confined in the triaxial cell with the boundary conditions shown in Figure 14. The following boundary conditions are maintained throughout the probe event. The walls are frictionless. The bottom wall is fixed, and gravity is activated. The top wall provides axial pressure, and the side walls provide lateral pressure. These pressures may be maintained constant, and equal to either their initial values (which correspond with the compression-test state) or specified values. The lateral pressure is maintained by a servomechanism that controls the side-wall velocities. The axial pressure is maintained by a separate servomechanism that controls the top-wall velocity. The force at the bottom wall may become larger than the force at the top wall, because the bottom wall resists the axial pressure, the weight of the grains, and the force imposed by the rod/plate.

[7] A *PFC* clump is a collection of overlapping spherical pebbles that remain fixed relative to one another. It behaves as a rigid body with associated mass.

[8] The walls remain fixed relative to one another, and behave as a rigid body with associated mass.

[9] Tan et al. (2014) modeled the hammer loads during the DCP and LWD tests as follows. A triangular force history was used for both tests. For the DCP test, the force history had a 0.1 ms duration with a peak force of 105 kN. These values were based on the experimentally measured load history during a DCP test with a load cell on the anvil (Nazarian et al., 2000), which measured an approximate triangular force history over 0.1 ms duration with a peak force of approximately 80 kN. For the LWD test, the force history had a 40 ms duration with a peak force of 6.28 kN, which provides a 200 kPa peak stress acting on a 200 mm diameter plate. These values were based on the results in Fleming et al. (2007).

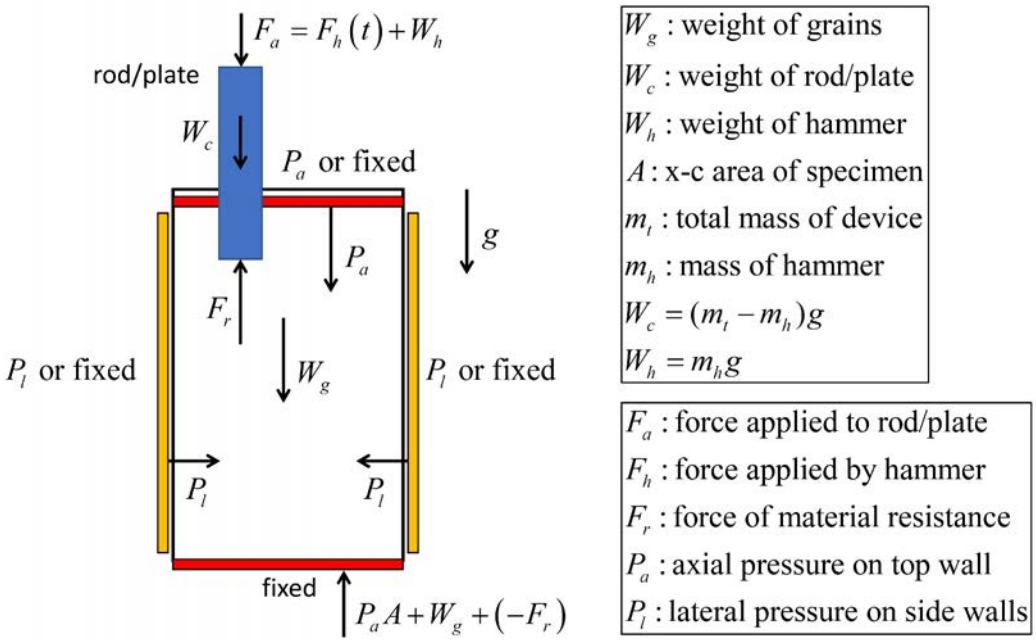

Figure 13 Sketch of probed system showing loads acting on the material.

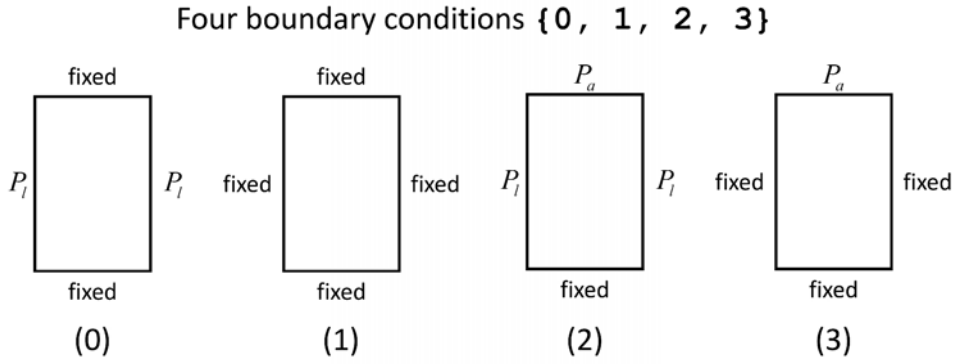

Figure 14 Boundary conditions enforced during a probe event. The bottom wall is fixed. The top wall and side walls can either be fixed, or provide a constant pressure boundary condition.

When simulating a DCP test, only the lower portion of the cone-tipped rod is included in the model. When simulating a LWD test, only the plate is included in the model. The rod/plate is modeled as a *PFC* clump. The rod/plate does not interact with the walls, it interacts only with the grains. If the DCP test is performed with a boundary-condition code of zero, then the system mimics driving a rod through a hole in the fixed top platen during a triaxial test in which the confining pressure is kept constant. The hammer drop is modeled by applying a time-varying external force to the rod/plate. The force-time history has a symmetrical triangular shape over a specified duration with a specified peak force.

The probe parameters are listed in Table 4. When performing a DCP test ($T_p = 0$), only the lower portion of the cone-tipped rod is included in the model (see Figure 15), and its geometry is defined by the cone included angle (θ_c), cone base diameter (D_c), rod diameter (D_r) and rod length (l_r). The cone-tipped rod is modeled as a clump, consisting of overlapping pebbles that just touch its sides. The number of pebbles, and their positions and radii are determined by the number of pebbles along the cone and rod axes (n_c and n_r), and the diameter of the pebble at the cone tip (D_t). A typical DCP clump is shown in Figure 16.

Table 4 DCP and LWD Probe Parameters

Parameter	Type	Range	Default	Description
T_p, **dl_probeType**	INT	$\{0,1\}$	0	probe-type code $\begin{cases} 0, & \text{DCP} \\ 1, & \text{LWD} \end{cases}$
Geometry group:				
θ_c, **dcp_coneAng**	FLT	$(0.0, 90.0)$	NA	cone included angle [degrees] $(T_p = 0)$
D_c, **dcp_coneBaseDiam**	FLT	$(0.0, \infty)$	NA	cone base diameter $(T_p = 0)$
D_r, **dcp_rodDiam**	FLT	$(0.0, \infty)$	NA	rod diameter $(T_p = 0)$
l_r, **dcp_rodLen**	FLT	$(0.0, \infty)$	NA	rod length $(T_p = 0)$
n_c, **dcp_nc**	INT	$[4, \infty)$	4	number of pebbles along cone axis $(T_p = 0)$
n_r, **dcp_nr**	INT	$[4, \infty)$	4	number of pebbles along rod axis $(T_p = 0)$
D_t, **dcp_Dt**	FLT	$(0.0, \infty)$	NA	diameter of pebble at cone tip $(T_p = 0)$
D_p, **lwd_plateDiam**	FLT	$(0.0, \infty)$	NA	plate diameter $(T_p = 1)$
n_r, **lwd_nr**	INT	$[2, \infty)$	3	number of touching pebbles in radial direction $(T_p = 1)$
Material properties group:				
m_t, **dl_massTot**	FLT	$(0.0, \infty)$	NA	device mass (including hammer)
m_h, **dl_massHam**	FLT	$(0.0, \infty)$	NA	hammer mass
E_s^*, **dl_semod**	FLT	$[0, \infty)$	0.0	rod/plate surface eff. modulus

κ_s^*, **dl_skrat**	FLT	$[0,\infty)$	0.0	rod/plate surface stiffness ratio
μ_s, **dl_sfric**	FLT	$[0,\infty)$	0.0	rod/plate surface friction coef.
Boundary conditions group:				
B_c, **dl_BCcode**	INT	$[0,3]$	0	boundary-condition code $\begin{cases} 0, & \text{top fixed, } P_l \text{ constant} \\ 1, & \text{top fixed, lateral fixed} \\ 2, & P_a \text{ constant, } P_l \text{ constant} \\ 3, & P_a \text{ constant, lateral fixed} \end{cases}$
$(P_a)'$, **dl_BCPaTop**	FLT	$[0,\infty)$	0.0	specified axial pressure (if value is non-zero)
$(P_l)'$, **dl_BCPl**	FLT	$[0,\infty)$	0.0	specified lateral pressure (if value is non-zero)
Δ_f, **dl_fPen**	FLT	$[0,\infty)$	0.0	forced penetration (if value is non-zero)
$\dot{\varepsilon}_f$, **dl_fPenRate**	FLT	$[0,\infty)$	0.0	forced penetration strain rate w.r.t. material vessel height
α, **dl_localDampFac**	FLT	$[0.0,0.7]$	0.0	local-damping factor (applied to grains and DCP)
α_h, **dl_hillDampCon**	FLT	$[0.0,1.0]$	0.0	damping constant of hill material (applied to grain-grain contacts)
g, **dl_grav**	FLT	$[0,\infty)$	0.0	gravitational acceleration
r_p, **dl_plRad**	FLT	$[0,\infty)$	0.0	placement radius
θ_p, **dl_plAng**	FLT	$[0.0,360.0)$	0.0	placement angle [degrees] w.r.t. positive x-axis
C_m, **dl_conLat**	INT	$\{0,1\}$	0	constrain lateral motion flag ($[0,1]:[\text{no},\text{yes}]$)
F_h, **dl_Fh**	FLT	$(0.0,\infty)$	0.0	hammer-force peak
t_h, **dl_th**	FLT	$(0.0,\infty)$	0.0	hammer-force duration
n_h, **dl_nh**	INT	$[500,\infty)$	2000	minimum number of steps during hammer-drop interval
n_{hi}, **dl_nhi**	INT	$[1,\infty)$	5	number of hammer-drop intervals to resolve drop process
Servo control and static equilibrium group:				
ε_p, **dl_PTol**	FLT	$(0.0,\infty)$	**pk_PTol**	pressure tolerance $\left(\frac{\lvert P-P_s\rvert}{P_s}\le\varepsilon_p\right)$ where P is current pressure
ε_{lim}, **dl_ARatLimit**	FLT	$(0.0,\infty)$	1×10^{-5}	equilibrium-ratio limit

				(parameter of **ft_eq**)
n_{lim}, **dl_stepLimit**	INT	$[1,\infty)$	**pk_stepLimit**	step limit (parameter of **ft_eq**)
v_{lim}, **dl_vLimit**	FLT	$(0.0,\infty)$	$10H\dot{\varepsilon}_a,\ \dot{\varepsilon}_a = 0.1$	servo velocity limit

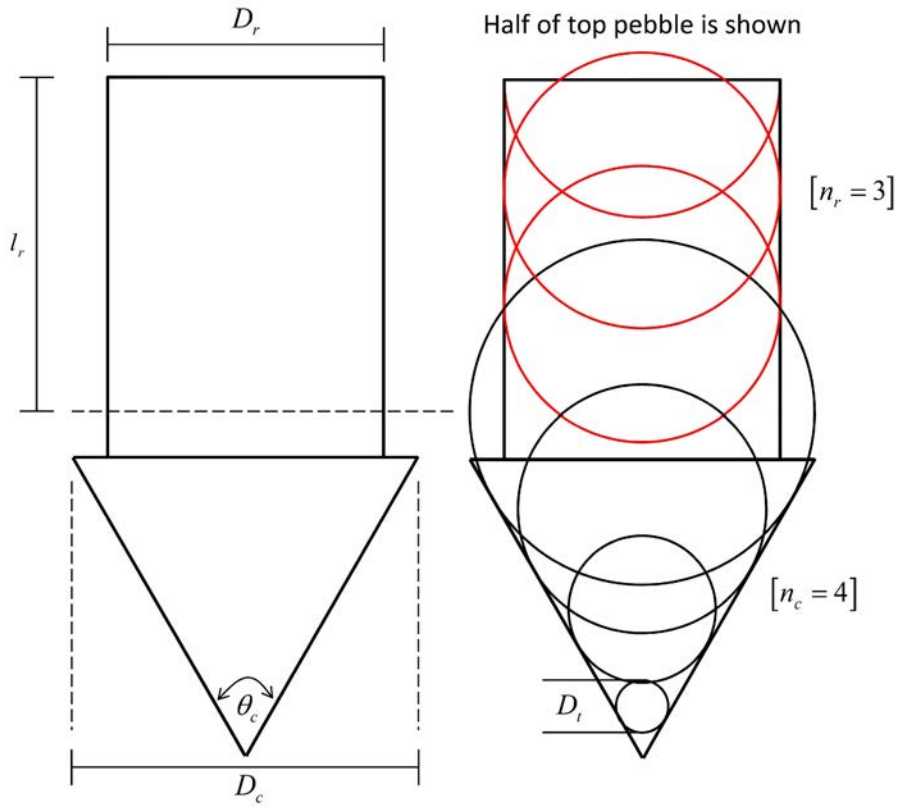

Figure 15 Parameters defining DCP geometry and clump discretization.

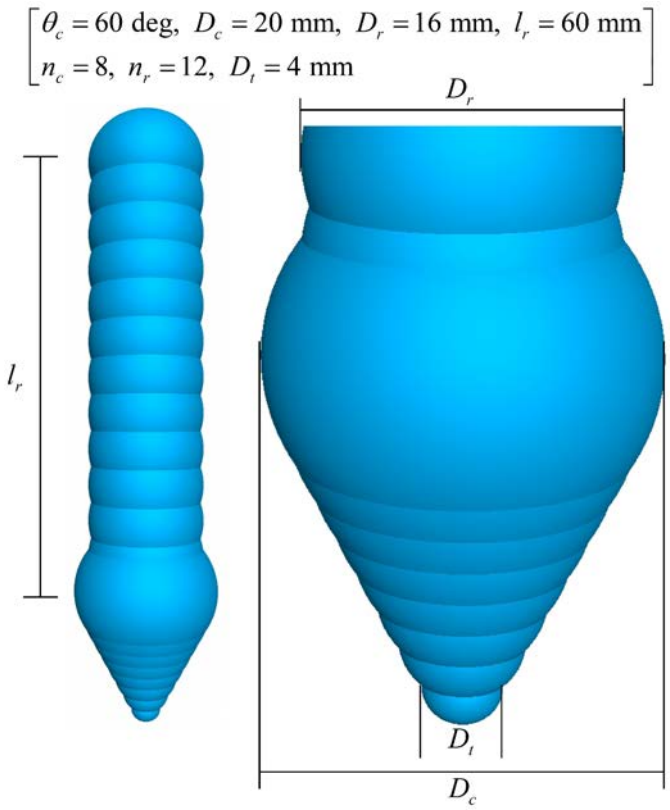

Figure 16 Typical DCP clump and parameter values.

When performing a LWD test ($T_p = 1$), only the plate is included in the model (see Figure 17), and its geometry is defined by the plate diameter (D_p) and number of touching pebbles in the radial direction (n_r). The plate is modeled as a clump, consisting of overlapping pebbles that form rings about the plate center. All pebbles have the same diameter, which is chosen such that n_r touching pebbles span from the plate center to the plate perimeter. The outer ring of pebbles is centered along the plate perimeter. A ring of pebbles is generated starting at each touching pebble (the solid green circles in Figure 17), and there are sufficient pebbles in each ring such that these pebbles just overlap. There are additional rings generated at the midpoints between each pair of touching pebbles (the dashed green circles in Figure 17).

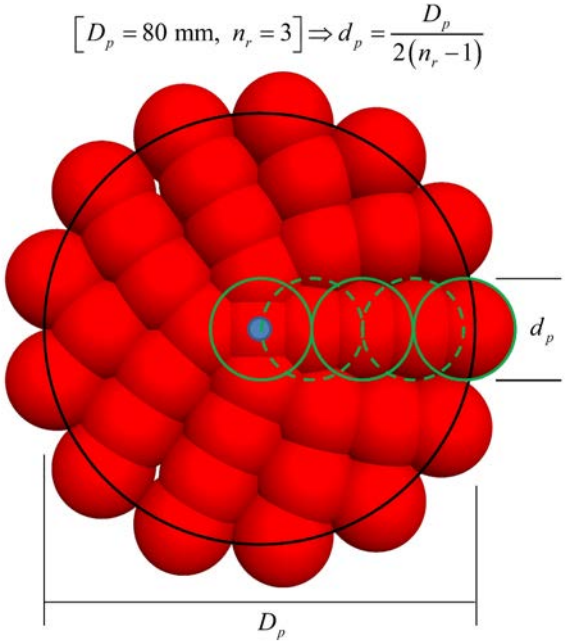

Figure 17 Typical LWD clump and parameter values. The two parameters define the plate geometry and discretization.

The material properties of the rod/plate are defined by the total mass of the device and mass of the hammer (m_t and m_h). It is the mass of the device without the hammer that is accelerated by the hammer loading. The hammer mass contributes to the total weight of the device. The material properties of the rod/plate surface are defined by the rod/plate surface effective modulus, stiffness ratio, and friction coefficient (E_s^*, κ_s^* and μ_s).[10]

The probe test consists of a setup phase, followed by placement and hammer-drop phases. During the setup phase, the boundary conditions (see Figure 14) are established (B_c, P_a' and P_l'), gravity is activated (g), and the model is cycled to reach static equilibrium. The model state is saved at the end of the setup phase.

During the placement phase, the rod/plate is created, a forced penetration may be imposed (Δ_f and $\dot{\varepsilon}_f$), and the rod/plate comes to static equilibrium. The rod/plate is modeled as a clump. It is oriented vertically above the material vessel, such that its lowest point is at the current height of the top wall and its location is specified with respect to the vessel axis by the placement radius and angle (r_p and

[10] The linear contact model is installed at the rod/plate-grain and rod/plate-grid contacts; the stiffness and friction coefficient of these contacts are set based on the specified deformability and friction coefficient. The null contact model is installed at the rod/plate-wall contacts.

θ_p), as shown in Figure 18. The rod/plate interacts only with the grains and the grid, it does not interact with the walls. The rod/plate is constrained to remain vertical — it cannot rotate, it is free to move axially, and its lateral motion is either free or constrained (C_m). The mass of the rod/plate without the hammer is assigned to the clump, and then the weight of the hammer is applied to the clump as an external force that is oriented in the axial direction, and applied at the clump centroid. The clump displacement and elapsed time are set to zero. If a forced penetration is desired ($\Delta_f \neq 0$), then it is imposed as follows. The axial velocity-fixity is set, the clump velocity is set equal to v ($v = \dot{\varepsilon}_f H$, where H is the specimen height), and the model is cycled until the clump displacement reaches the desired value (Δ_f). The axial velocity-fixity is then removed, thereby freeing the clump to move in response to the total force acting upon it. The model is cycled until a state of static equilibrium is reached. If a forced penetration was imposed, then there may be a slight rebound; otherwise, there will be a settlement. The specified damping is activated (see damping discussion in the next paragraph). The model state is saved at the end of the placement phase.

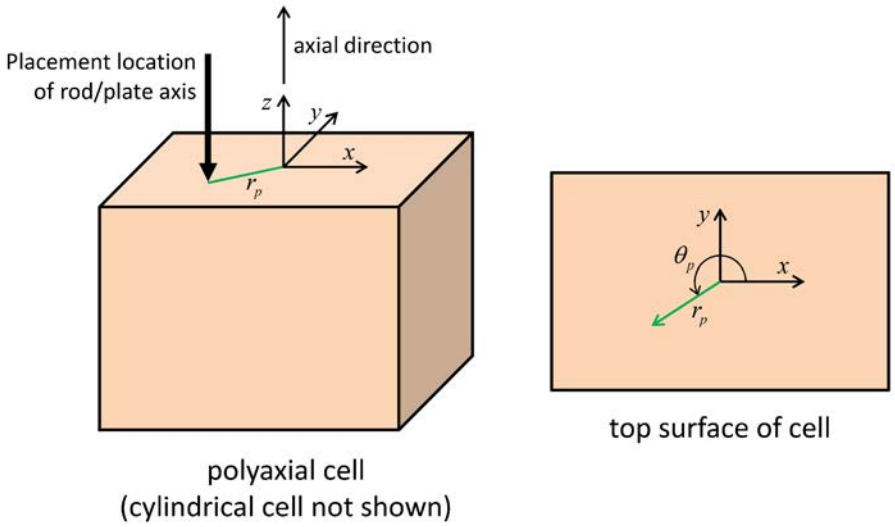

Figure 18 Parameters controlling rod/plate placement.

The model is run dynamically (not quasi-statically) during the hammer drops, because there are dynamic effects occurring that may influence the penetration. The hammer loading will accelerate both the rod/plate and the grains, and if the local-damping factor is too large, then excessive energy will be removed from the system, thereby reducing the rod/plate penetration from its true value. Two forms of damping are available: local-damping and hill damping. During a quasi-static run, we set the local-damping factor (α) equal to 0.7, and the hill damping constant (α_h) to zero. During a dynamic run, we set the local-damping factor to a small value (0.02 or less), and set the hill damping constant to 0.07. The value of 0.07 was used in all simulations performed by Tan et al. (2014), and this value corresponds with a restitution coefficient of 0.9. These damping values are assumed to

provide realistic energy dissipation for a granular material, but further study is warranted to confirm this assumption. It would be prudent to study the effect of damping on the DCP penetration and LWD deflection.

The hammer drop occurs during the hammer-drop phase. The falling hammer is modeled by applying a time-varying external force to the rod/plate. The hammer force is defined by its peak value and duration (F_h and t_h) as shown in Figure 19. The minimum number of steps during the hammer drop (n_h) ensures proper resolution of the loading process, and the number of hammer-drop intervals over which to maintain the smaller timestep (n_{hi}) ensures proper resolution of the model response.[11] The rod/plate accelerates in response to the hammer force, and penetrates further into the granular material. The model is cycled until a state of static equilibrium is reached. The model state is saved at the end of the hammer-drop phase.

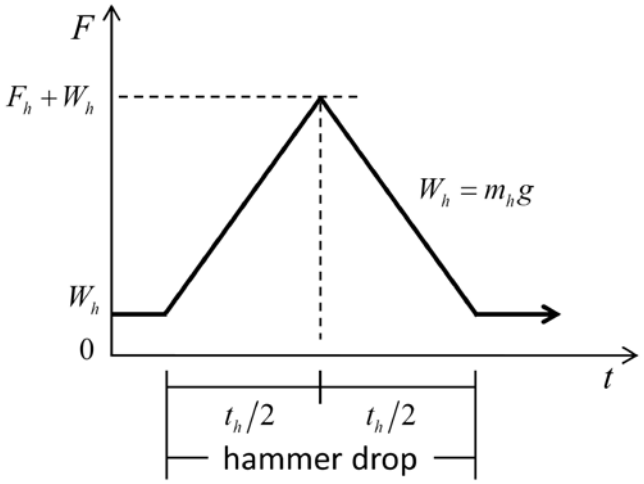

Figure 19 Total external force applied to the rod/plate during the hammer drop.

The following items are monitored during the probe test. The axial pressure acting on the top wall (P_a) and the lateral pressure acting on the side walls (P_l) are stored in the *FISH* variables **dl_PaTop** and **dl_Pl**. The elapsed time since rod/plate creation is stored in the *FISH* variable **dl_eTime**. The penetration and penetration velocity are taken as the motion in the z-direction, and stored in the *FISH* variables **dl_pen** and **dl_penV**. The penetration is measured with respect to the height of the top wall at the start of the placement phase. The applied external force and resisting force (provided by the material) acting on the rod/plate are stored in the *FISH* variables **dl_aF** and **dl_rF**.

[11] The timestep is reduced to meet this criterion, and the reduced timestep is used both during the hammer drop and for the specified number of multiples of the hammer-drop duration (n_{hi}).

2.4 Simple Example

A simple example of the DCP and LWD probe capability is provided in the **`MG-HillGrid`** example-project directory. The example serves as a base case, and provides a modeled system at the lowest resolution sufficient to demonstrate system behavior. The modeled system is the same as that described in the Simple Example section of Potyondy (2018), with the exception that the grid is modeled using beamed contacts instead of parallel-bonded contacts. The grid-set properties are listed in Table 2. The materials are dry while being created in a polyaxial material vessel (of initial 240 mm height and 120 mm width and depth, with a 500 MPa effective modulus) and packed at a 1 MPa material pressure as shown in Figure 20.

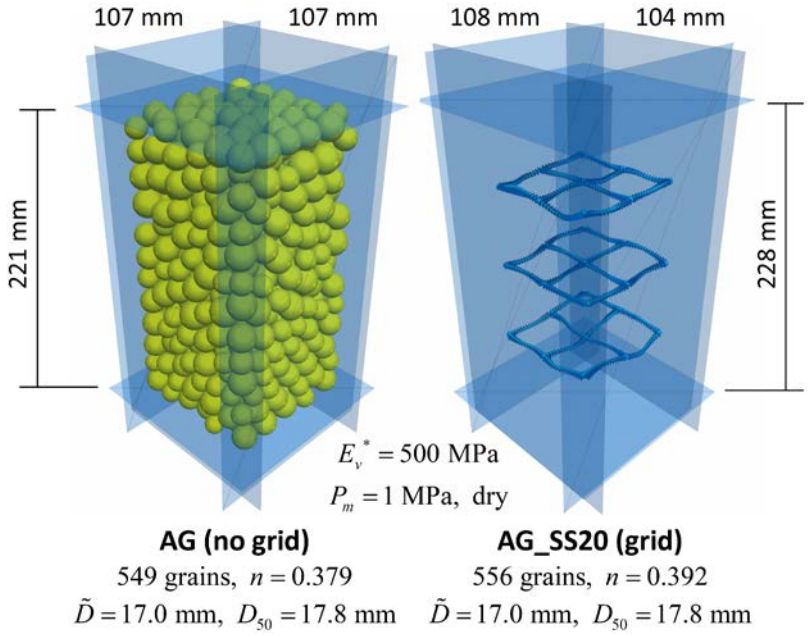

Figure 20 Dry AG and AG_SS20 materials at the end of material genesis.

The materials are subjected to triaxial testing. The materials are tested dry. During each triaxial test, the confinement is 25 kPa, and two load-unload cycles are performed to produce the stress-strain curves in Figure 21. We focus on the material at the end of the seating phase of the triaxial test, at which point the confinement has been reduced from 1 MPa to 25 kPa, and the porosity has increased from 0.379 to 0.384. The material has very little strength at this low confinement, and is in a very loosely packed state. The material with the grid is weaker (being able to sustain a deviator stress of only 9 kPa) and more loosely packed than the material without the grid. The DCP and LWD probes are performed on the material at the end of the seating phase of the triaxial test, when the axial and lateral pressures are both equal to 25 kPa.

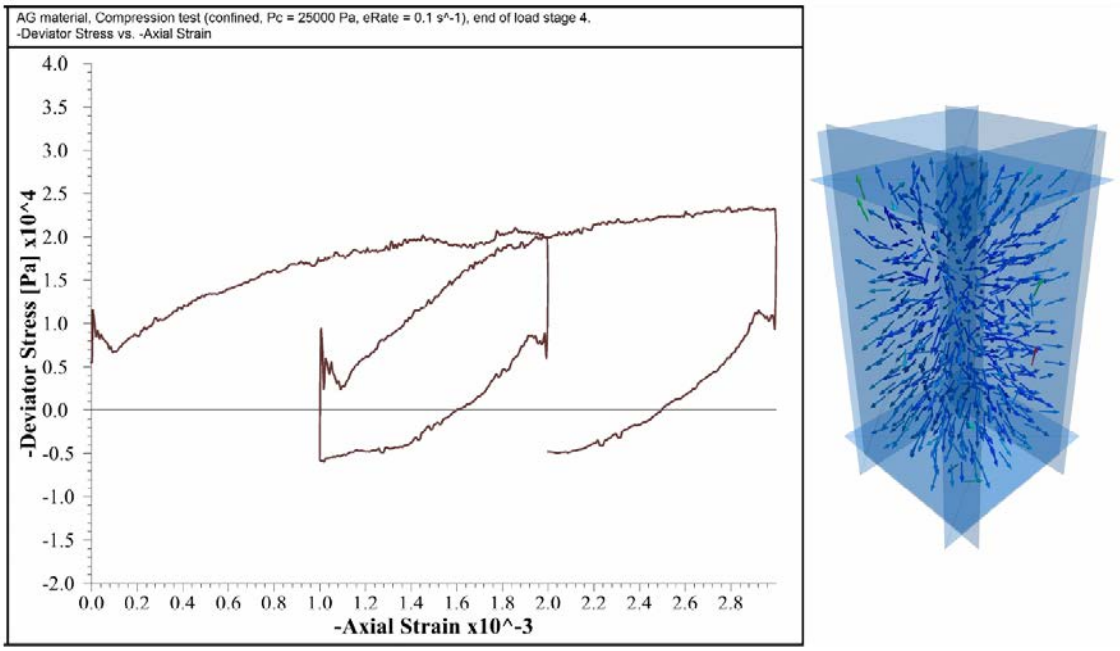

Figure 21 Deviator stress versus axial strain for dry AG material tested at 25 kPa confinement, and grain displacements induced by reducing the confinement from 1 MPa to 25 kPa.

2.4.1 DCP Test

The present discussion focuses on the no-grid model to demonstrate reasonable model behavior. The grid model is discussed only to demonstrate that the DCP penetration is being inhibited by the grid. A quantitative comparison of DCP penetration between grid and no-grid models should be performed using models with the same porosity, but in the present case, the porosity of the grid model is larger than that of the no-grid model (0.407 versus 0.384).

The DCP test properties are listed in Table 5. The DCP geometry corresponds with the MnDOT standard, and the geometry of the near-cone region is shown in Figure 16. The DCP is centered along the specimen axis, and free to move laterally. The DCP test is performed on the materials at the end of the seating phase of the triaxial test, when the axial and lateral pressures are both 25 kPa. During the DCP test, the lateral pressure is maintained constant, and the top wall is fixed. The DCP is forced 50 mm into the material, and then four hammer drops are performed. Each hammer drop has a 105 kN peak force and 0.1 ms duration.

Table 5 DCP Test Properties*

Property	Value
T_m	0
Geometry group:	
θ_c [deg], D_c [mm], D_r [mm], l_r [mm]	60, 20, 16, 240
$\{n_c, n_r\}$, D_t [mm]	{8,48}, 4
Material properties group:	
(m_t, m_h) [kg], E_s^* [GPa], κ_s^*, μ_s	(13,8), 1[1], 2, 0.6
Boundary conditions group:	
B_c, $(P_a)'$ [kPa], $(P_l)'$ [kPa] Δ_f [mm], $\dot{\varepsilon}_f$	0, 0, 0, 50, 1.0
α, α_h, g [m/s^2], r_p [mm], θ_p [deg], C_m	0.02, 0.07, 9.81, 0, 0, 0
F_h [kN], t_h [ms], n_h, n_{hi}	105, 0.1, 2000, 10
Servo control group:	
ε_p, ε_{lim}, n_{lim}, v_{lim}	1×10^{-2}, 2×10^{-5}, 5×10^{5}, 0.24

* Probe parameters are defined in Table 4.

[1] This value is chosen large enough to prevent excessive interpenetration of the DCP and grains.

The DCP penetration is shown in Figure 22, and the modeled system after four hammer drops is shown in Figure 23. The DCP penetration increases with each hammer drop, and the total penetration after four drops is 148 mm. The downward motion of the DCP is resisted by the forces exerted by the grains on the cone. These resisting forces are evident in the force-chain plot of Figure 24, which shows the force-chain configurations at the ends of the forced penetration and the first two hammer drops. It is the disturbance of these stable force-chain configurations by the hammer loading that allows the DCP to move downward. The DCP may also move laterally during its downward motion as it encounters grains that are offset from its vertical axis.

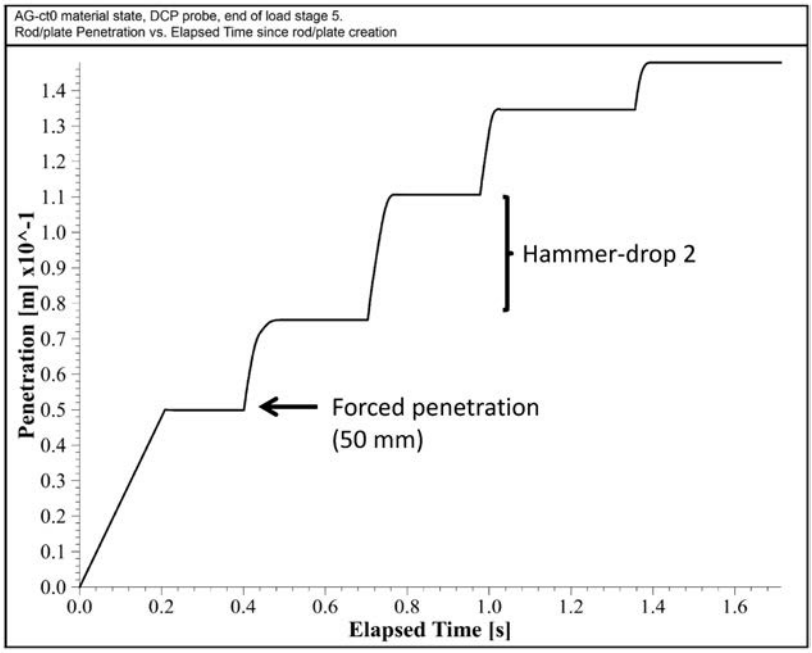

Figure 22 Penetration versus elapsed time after four hammer blows to the no-grid model.

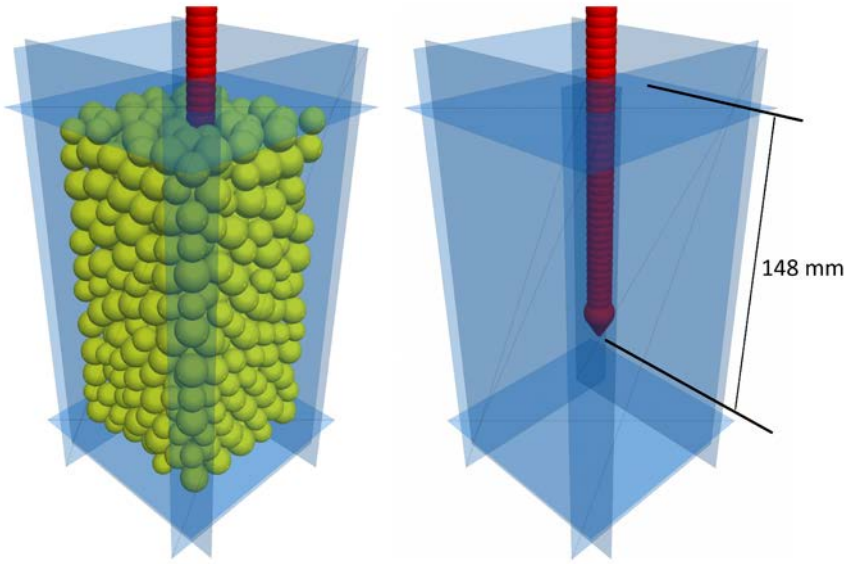

Figure 23 Model configuration after four hammer blows to the no-grid model.

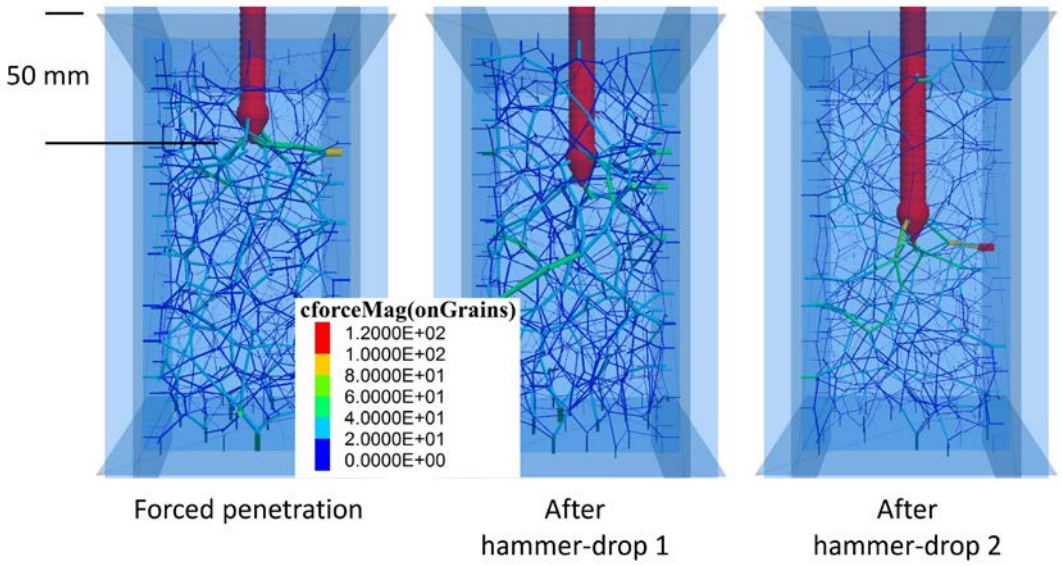

Figure 24 Stable force-chain configurations during the DCP test on the no-grid model.

The applied and resisting forces during the first hammer-drop event are shown in Figure 25. The resisting force begins to build up during the hammer-drop duration, and it is well resolved while the timestep remains small. When the timestep returns to its original value (updated automatically to ensure stable forward integration of the equations of motion), the resisting force varies in a less-smooth fashion. An ideal simulation would maintain the smaller timestep throughout the entire drop process, which includes the time of hammer-force application and additional time during which the resisting force increases and then returns to equal the DCP weight. It is expected that the response shown here (controlled by n_h and n_{hi}) provides an adequate resolution of the loading and response processes, while maintaining an acceptable overall run time. The time scales associated with the loading and response processes are seen by plotting the applied and resisting forces versus time in Figure 26. The peak hammer-drop force is 105 kN, whereas the peak resisting force is only 800 N (which is 130 times smaller). The loading process occurs over a 0.1 millisecond interval, but the response process occurs over a 0.1 second interval (which is 1000 times longer). These force magnitudes and time scales are reasonable.

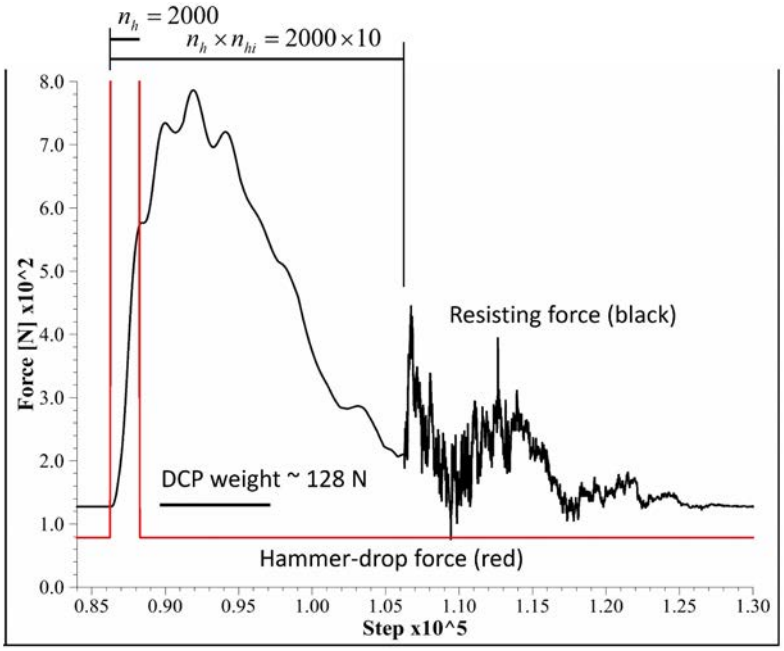

Figure 25 Applied (red) and resisting (black) forces versus step during the first hammer-drop event.

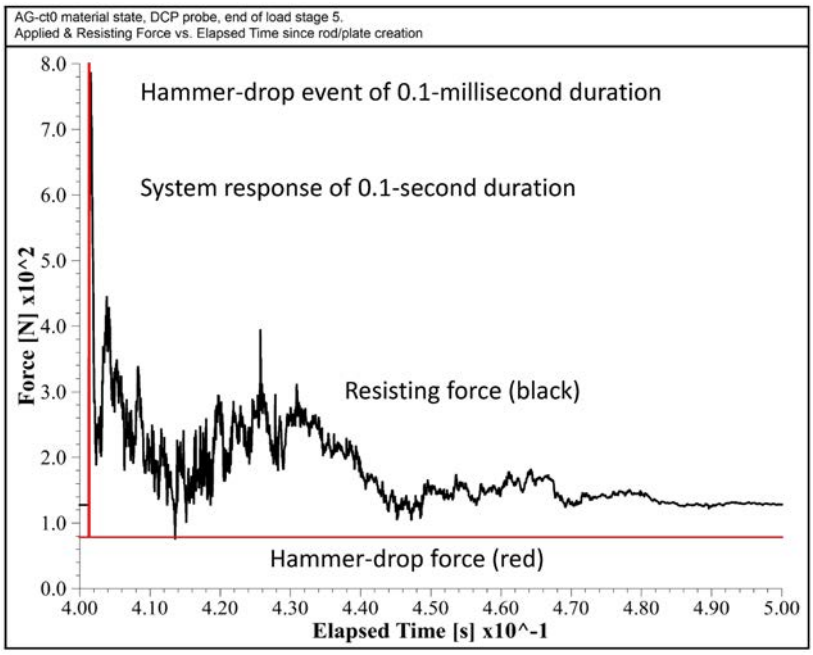

Figure 26 Applied (red) and resisting (black) forces versus time during the first hammer-drop event.

The resisting force during the forced-penetration process is shown in Figure 27. The resisting force fluctuates during the process as the DCP pushes past grains, forcing them to move apart and rearrange to accommodate its presence. The peak resisting force is approximately 420 N. It is expected that this peak value will be sensitive to the penetration rate. The current penetration rate was chosen slow enough to approach quasi-static conditions. After the imposed penetration ceases, and the axial motion of the DCP is freed, the force drops back to the DCP weight. This behavior is reasonable, because the work done on the system by the DCP as it is forced into the material is dissipated by frictional sliding and grain rearrangement. Very little of the imposed energy is stored as strain energy, and thus, there is negligible rebound of the DCP when its axial motion is freed.

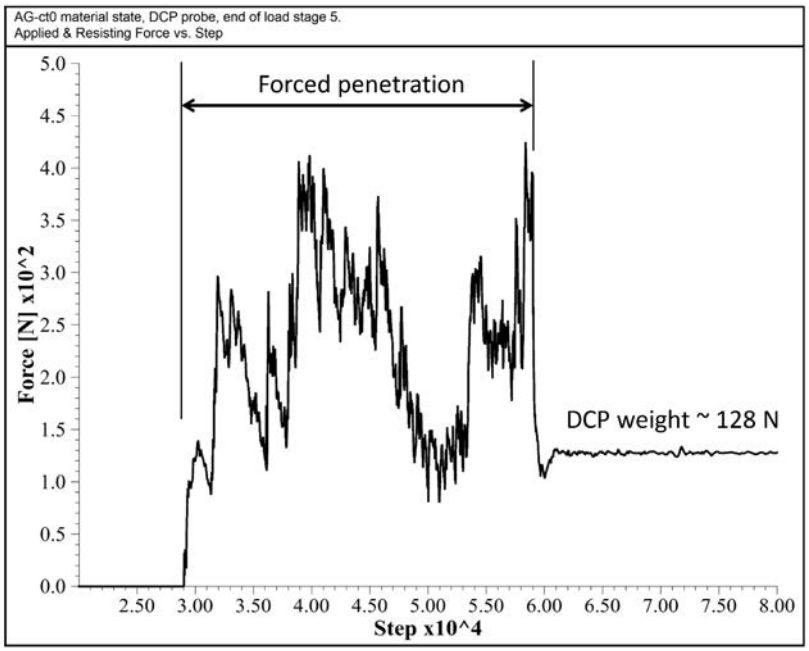

Figure 27 Resisting force versus step during the forced-penetration process.

A final check of the system behavior is to examine the axial and lateral pressures during the forced-penetration process as shown in Figure 28. The servomechanism that controls the side-wall velocities is maintaining the lateral pressure at its initial value of 25 kPa. The top wall is fixed; therefore, the pressure acting on this wall is reduced to 14 kPa as the DCP moves into the material and compresses the top of the material.

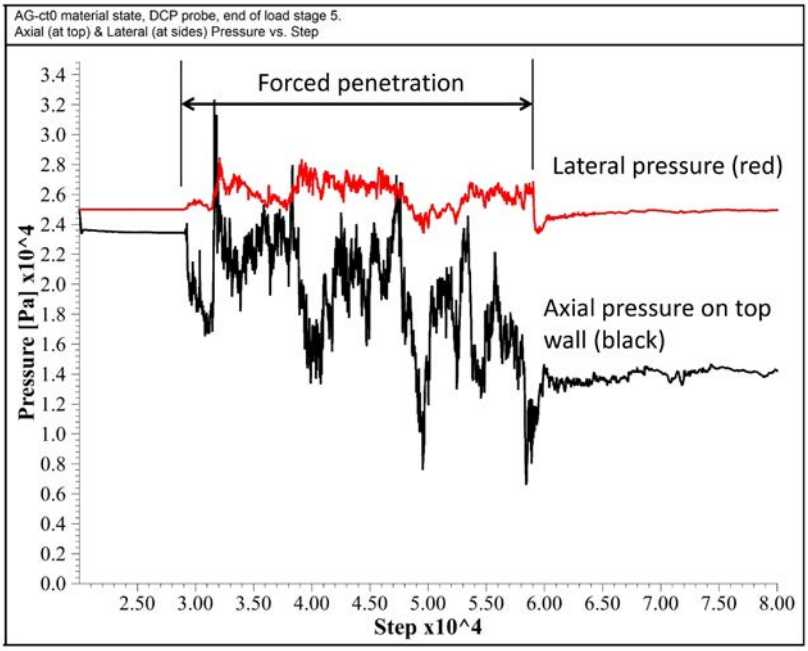

Figure 28 Axial and lateral pressures versus step during the forced-penetration process.

The following response is observed when the same DCP test, with the same boundary conditions, is performed on the AG_SS20 material (the material with grid) at the end of the seating phase of the triaxial test, when the axial and lateral pressures are both 25 kPa. During the DCP test, the lateral pressure is maintained constant, and the top wall is fixed. The DCP is placed along the specimen axis, and the top-most grid lies 60 mm below the top of the specimen. The DCP is forced 50 mm into the material, and then four hammer drops are performed. The DCP penetration is shown in Figure 29, and the modeled system after four hammer drops is shown in Figure 30. The DCP penetration increases with each hammer drop, and the total penetration after four drops is 122 mm. This is less than the 148-mm total penetration of the no-grid model. The ability of the grid to inhibit the DCP penetration is evident in Figure 31. After the first hammer drop, the DCP has contacted the top-most grid and begun to penetrate the back-left aperture. Very little penetration occurs during the second hammer drop, as the grid forces the DCP to move laterally. Substantial penetration occurs during the third hammer drop, as the DCP moves past the top-most grid.

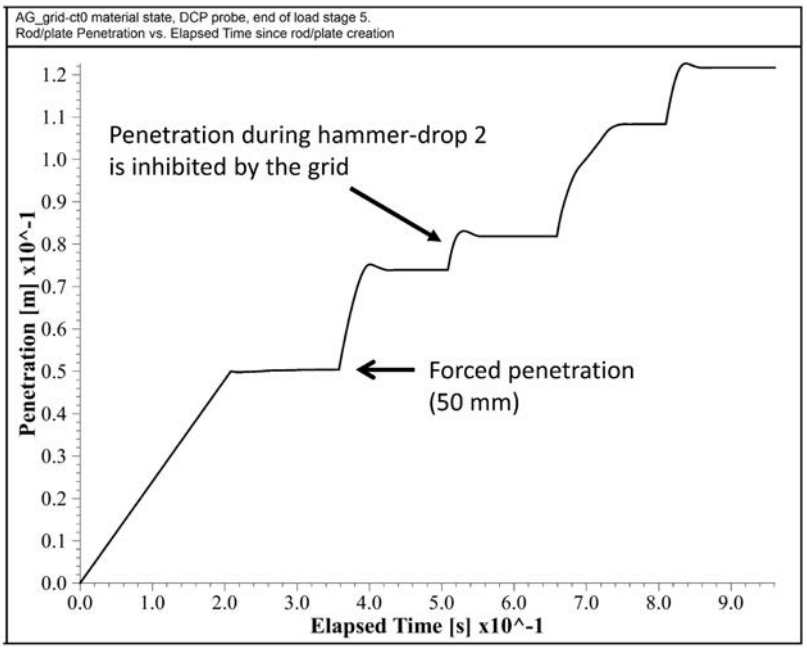

Figure 29 Penetration versus elapsed time after four blows to the grid model.

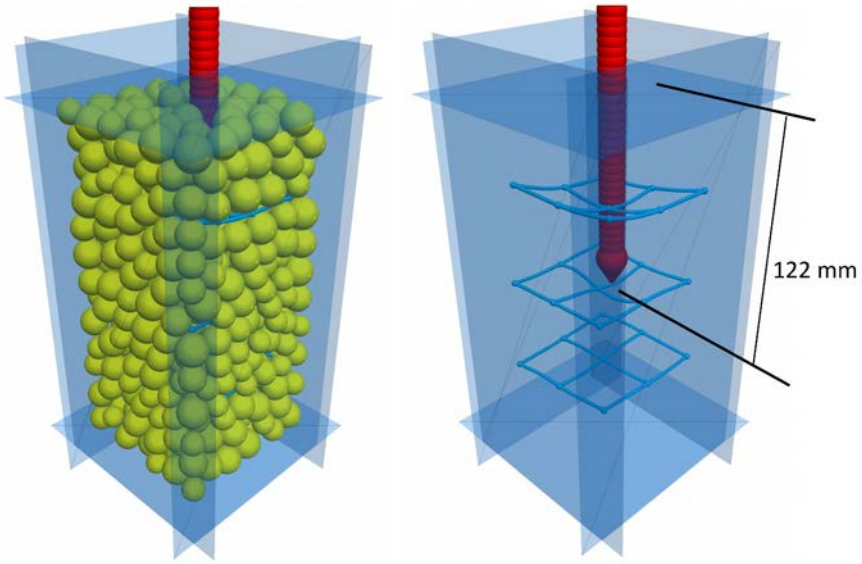

Figure 30 Model configuration after four hammer blows to the grid model.

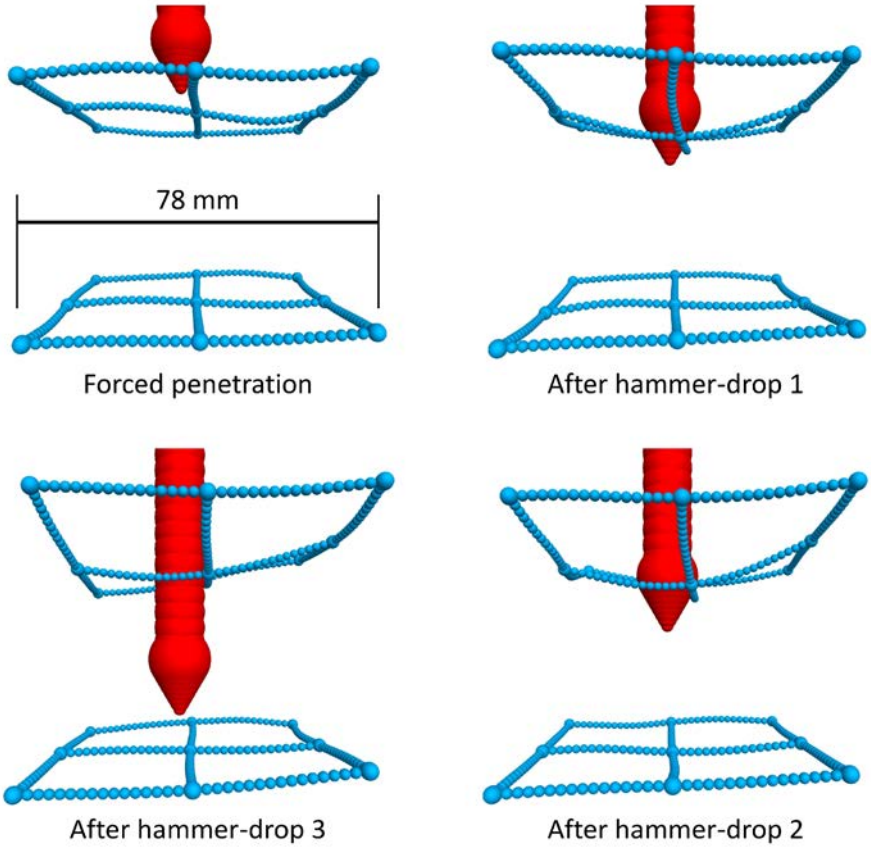

Figure 31 Evolving DCP location and grid configuration during the DCP test on the grid model.

2.4.2 LWD Test

The LWD test properties are listed in Table 6. The LWD geometry is shown in Figure 17. The LWD plate has an 80 mm diameter, and each hammer drop has a 250 N peak force and 40 ms duration such that the plate delivers a 50 kPa peak stress to the material.[12] The LWD is centered along the specimen axis, and is free to move laterally. The LWD test is performed on the materials at the end of the seating phase of the triaxial test, when the axial and lateral pressures are both 25 kPa. During the LWD test, the lateral pressure is maintained constant, and the top wall is fixed. The LWD settles under the force of gravity, and then eight hammer drops are performed.

[12] The MnDOT standard specifies that a 200 mm diameter plate deliver a 200 kPa peak stress to the material. The peak stress in the present model is reduced, because the material is in a very loosely packed state and cannot sustain the larger stress without excessive plastic deformation.

Table 6 LWD Test Properties*

Property	Value
T_m	1
Geometry group:	
$D_p\,[\text{mm}],\ n_r$	80, 3
Material properties group:	
$(m_t, m_h)\,[\text{kg}],\ E_s^*\,[\text{GPa}],\ \kappa_s^*,\ \mu_s$	$(34,10)^1$, 1, 2, 0.6
Boundary conditions group:	
$B_c,\ (P_a)'\,[\text{kPa}],\ (P_l)'\,[\text{kPa}]\ \Delta_f\,[\text{mm}],\ \dot{\varepsilon}_f$	0, 0, 0, 0, 0
$\alpha,\ \alpha_h,\ g\,[\text{m/s}^2],\ r_p\,[\text{mm}],\ \theta_p\,[\text{deg}],\ C_m$	0.02, 0.07, 9.81, 0, 0, 0
$F_h\,[\text{N}],\ t_h\,[\text{ms}],\ n_h,\ n_{hi}$	250, 40, 2000, 10
Servo control group:	
$\varepsilon_p,\ \varepsilon_{\text{lim}},\ n_{\text{lim}},\ \nu_{\text{lim}}$	1×10^{-2}, 2×10^{-5}, 5×10^{5}, 0.24

* Probe parameters are defined in Table 4.

[1] The total mass consists of a 15-kg plate, 5-kg guide rod, 10-kg hammer and 4-kg electronics (Zorn Stendal, 2005).

The LWD penetration is shown in Figure 32, and the modeled system after six hammer drops is shown in Figure 33. After an initial 1.4 mm penetration due to the self-weight of the device, the penetration increases with each hammer drop. This indicates that the material is not behaving elastically; instead, there is some plastic deformation. The penetration during the sixth hammer drop is shown in Figure 34, from which a 13 MPa modulus is obtained. The plastic deformation is evident in this plot. The hammer drops are compacting the material (see Figure 35). The resisting force tracks with the applied load during the sixth hammer-drop event (see Figure 36), and the maximum applied load just equals the device weight. Such a small applied load may not be sufficient to measure the elastic properties throughout the entire specimen depth. These results demonstrate that the model is working correctly. It is expected that more realistic and quantitatively correct behavior will be obtained for materials that are less loosely packed than the material examined here.

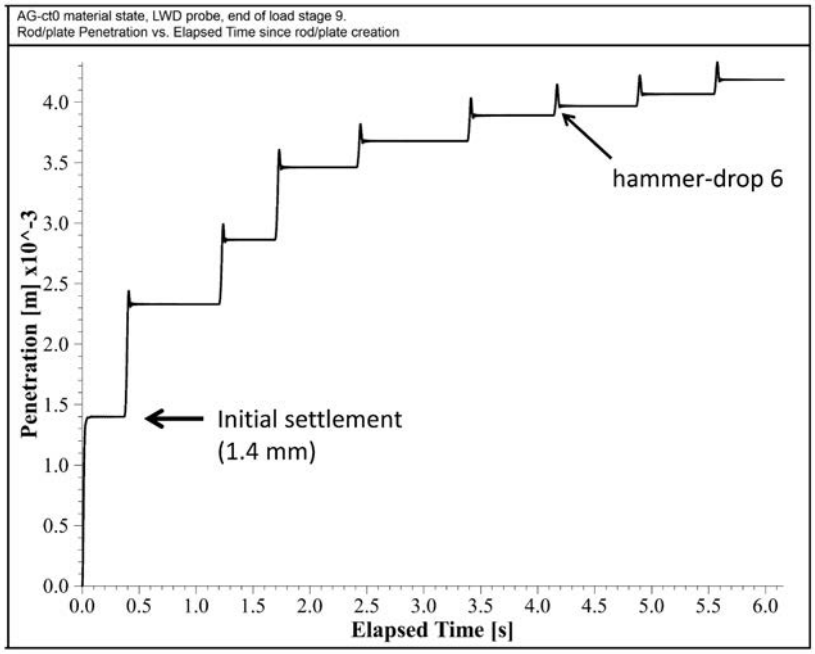

Figure 32 LWD penetration versus elapsed time after eight hammer blows to the no-grid model.

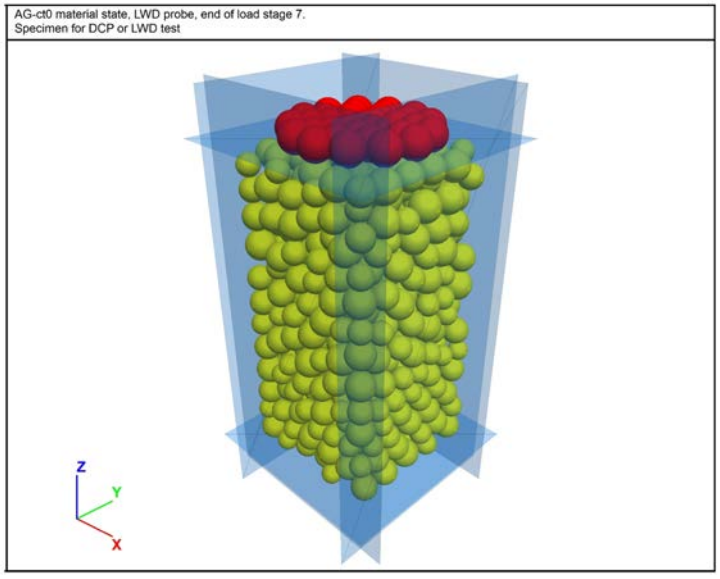

Figure 33 LWD model configuration after six hammer blows to the no-grid model.

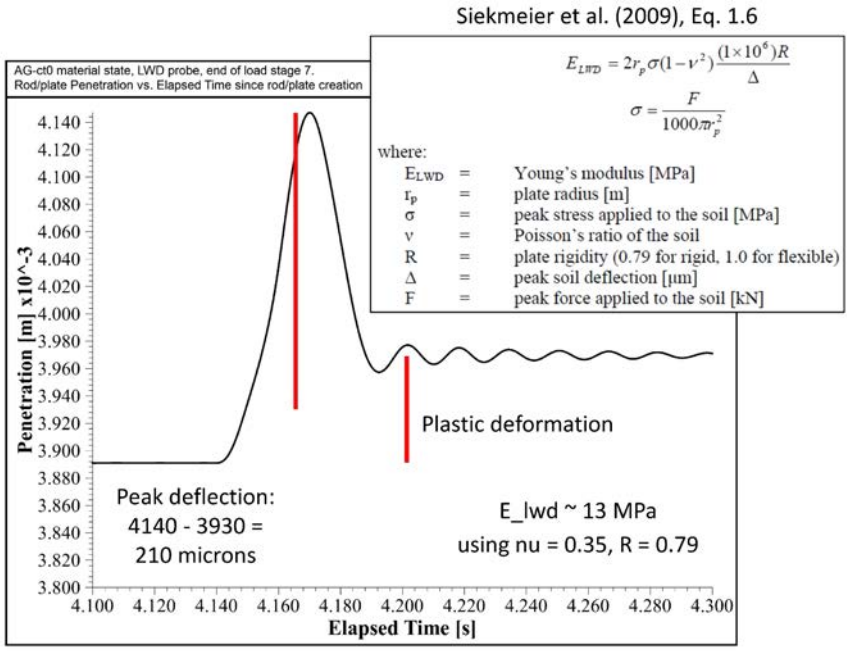

Figure 34 LWD model penetration versus elapsed time during the sixth hammer drop.

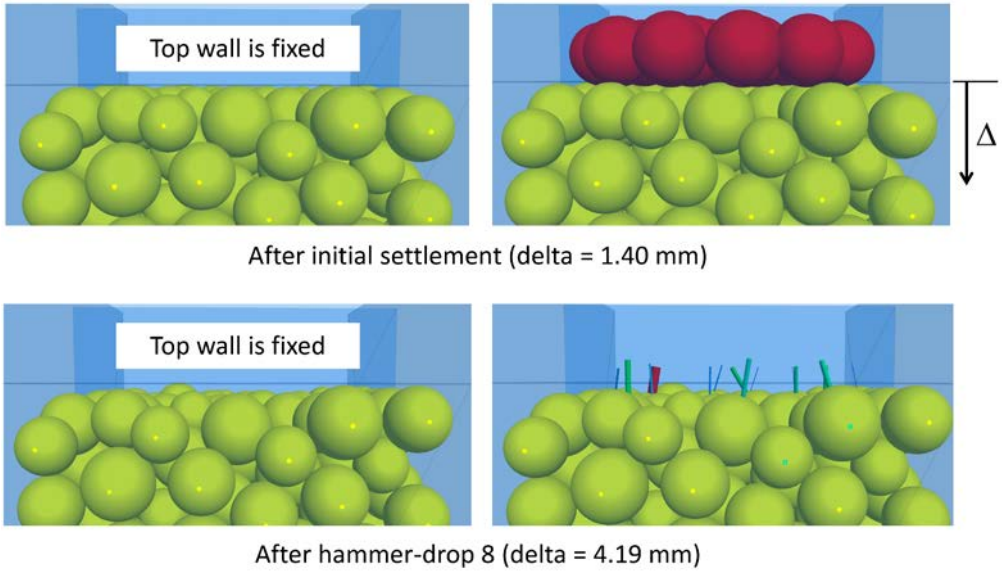

Figure 35 Top of no-grid LWD model after initial settlement and eight hammer blows, with the forces applied to the material by the plate shown in the bottom-right image.

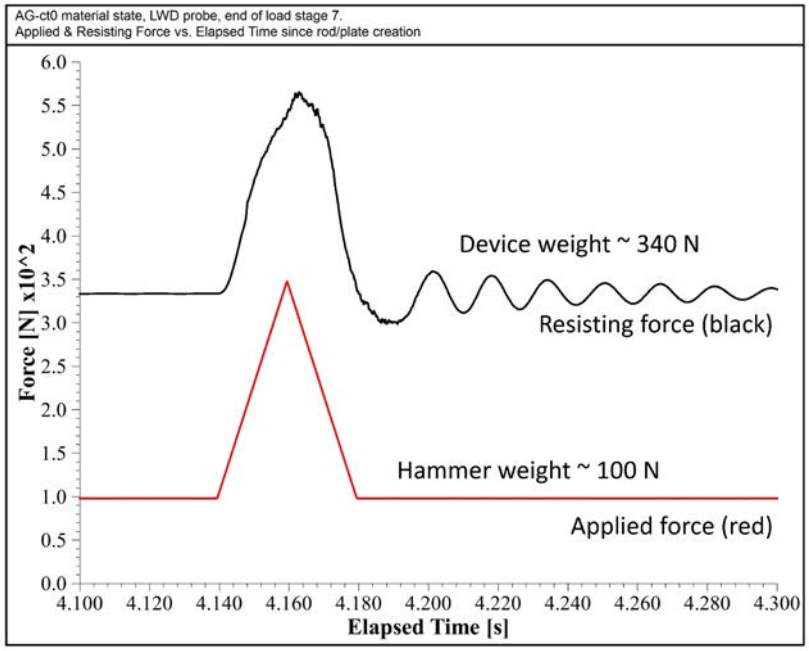

Figure 36 Applied (red) and resisting (black) forces versus time during the sixth hammer-drop of the no-grid LWD model.

3.0 REFERENCES

ASTM. (2015) "Standard Test Method for Use of the Dynamic Cone Penetrometer in Shallow Pavement Applications," Designation: D6951/D6951M-09 (Reapproved 2015), American Society for Testing and Materials, West Conshohocken, PA, 2015.

ASTM. (2007) "Standard Test Method for Measuring Deflections with a Light Weight Deflectometer (LWD)," Designation: E2583-07, American Society for Testing and Materials, West Conshohocken, PA, 2007.

Davich, P., F. Camargo, B. Larsen, R. Roberson and J. Siekmeier. (2006) "Validation of DCP and LWD Moisture Specifications for Granular Materials," Minnesota Department of Transportation Research Report MN/RC 2006-20, July 2006, Saint Paul, MN.

Fleming, P.R., M.W. Frost and J.P. Lambert. (2007) "Review of Lightweight Deflectometer for Routine In Situ Assessment of Pavement Material Stiffness," *Transportation Research Record: Journal of the Transportation Research Board*, No. 2004, pp. 80–87, DOI: 10.3141/2004-09, Transportation Research Board of the National Academies, Washington, D.C.

Garnica, P., N. Perez, J. Siekmeier, R. Roberson and B. Tanquist. (2017) "State of the Practice in Mexico and Minnesota to Estimate the Effect of Water Content/Suction in Subgrade Soils and Granular Materials," in ***Proceedings of PanAm-UNSAT 2017: Second Pan-American Conference on Unsaturated Soils*** (Dallas, TX, November 12–15, 2017).

Gupta, S., A. Ranaivoson, T. Edil, C. Benson and A. Sawangsuriya. (2007) "Pavement Design using Unsaturated Soil Technology," Minnesota Department of Transportation Research Report MN/RC 2007-11, Saint Paul, MN.

Gupta, S., A. Singh and A. Sawangsuriya. (2005) "Moisture Retention Characteristics of Base and Sub-base Materials," Minnesota Department of Transportation Research Report MN/RC 2005-06, Saint Paul, MN.

MnDOT. (2016) ***Standard Specifications for Construction***, 2016 Edition, Minnesota Department of Transportation, Saint Paul, MN.

Mooney, M., and R. Rinehart. (2009) "In Situ Soil Response to Vibratory Loading and Its Relationship to Roller-Measured Soil Stiffness," *Journal of Geotechnical and Geoenvironmental Engineering,* ***135***(8), ASCE, Washington, D.C.

Nazarian, S., V. Tandon, K. Crain and D. Yuan. (2000) "Use of Instrumented Dynamic Cone Penetrometer in Pavement Characterization," in ***Nondestructive Testing of Pavements and Backcalculation of Moduli: Third Volume*** (S.D. Tayabji and E.O. Lukanen, eds.), pp. 214–229, American Society for Testing and Materials, ASTM STP 1375, West Conshohocken, PA.

NCHRP 1-28A. (2003) "Harmonized Test Methods for Laboratory Determination of Resilient Modulus for Flexible Pavement Design," National Cooperative Highway Research Program, Transportation Research Board, Washington, D.C.

Potyondy, D. (2018) "Pavement-Design Package for PFC3D [pdPkg14]," Itasca Consulting Group, Inc., Technical Memorandum ICG16-8528-15TM (June 22, 2018), Minneapolis, MN.

Potyondy, D. (2017) "Material-Modeling Support in PFC [fistPkg25]," Itasca Consulting Group, Inc., Technical Memorandum ICG7766-L (March 16, 2017), Minneapolis, MN.

Potyondy, D. (2016) "Hill Contact Model [version 4]," Itasca Consulting Group, Inc., Technical Memorandum ICG7795-L (October 12, 2016), Minneapolis, MN.

Rinehart, R., and M. Mooney. (2009) "Measurement of Roller Compacted Induced Triaxial Soil Stresses and Strains," *Geotechnical Testing Journal*, ***32***(4), ASTM International, West Conshohocken, PA.

Siekmeier, J., and J. Casanova. (2016) "Geogrid Reinforced Aggregate Base Stiffness for Mechanistic Pavement Design," Saint Paul, Minnesota, Minnesota Department of Transportation Research Report 2016-24, MN/RC 2016-24, July 2016.

Siekmeier, J., C. Pinta, S. Merth, J. Jensen, P. Davich, F. Camargo and M. Beyer. (2009) "Using the Dynamic Cone Penetrometer and Light Weight Deflectometer for Construction Quality Assurance," Minnesota Department of Transportation Research Report MN/RC 2009-12, February 2009, Saint Paul, MN.

Tan, D., K. Hill and L. Khazanovich. (2014) "Quantifying Moisture Effects in DCP and LWD Tests Using Unsaturated Mechanics," Dept. of Civil Engr., University of Minnesota, Final Report to Minnesota Department of Transportation, Saint Paul, MN, MN/RC 2014-13, February 2014.

Tanquist, B. (2012) ***MnPAVE User's Guide***. Office of Materials, Minnesota Department of Transportation, Saint Paul, MN, July 2012.

Tutumluer, E., Y. Xiao and W. Wilde. (2015) "Cost Effective Base Type and Thickness for Long Life Concrete Pavements," Minnesota Department of Transportation Research Report 2015-42, Saint Paul, MN.

Xiao, Y., and E. Tutumluer. (2012) "Best Value Granular Material for Road Foundations," Minnesota Department of Transportation Research Report 2012-01, Saint Paul, MN.

Xiao, Y., E. Tutumluer, Y. Qian and J. Siekmeier. (2012) "Gradation Effects Influencing Mechanical Properties of Aggregate Base and Granular Subbase Materials in Minnesota," Transportation Research Record 2267, Transportation Research Board, Washington, DC.

Yohannes, B., K. Hill and L. Khazanovich. (2009) "Mechanistic Modeling of Unbound Granular Materials," Minnesota Department of Transportation Research Report MN/RC 2009-21, June 2009, Saint Paul, MN.

Zorn Stendal. (2005) ***Light Drop Weight Tester ZFG 2000: Operating Manual***, Stendal, Germany.

APPENDIX D:
BEAM CONTACT MODEL

Technical Memorandum

ITASCA
Consulting Group, Inc.

Date: June 22, 2018

To: John Siekmeier (MnDOT)

From: David Potyondy (Itasca)

Re: Beam Contact Model [version 1]

Ref: 2-3558-01:17TM07

This memo describes the beam contact model (version 1) as provided in the pavement-design package for *PFC* 5.0.[1] A pebbled-beam (P-beam) is a string of spherical balls for which the beam contact model exists at all ball-ball contacts. A P-beam provides the structural behavior of a prismatic and bisymmetrical beam composed of isotropic, linear elastic material. The model formulation and test problem are provided in the first and second major sections, respectively. The test problem consists of a tip-loaded cantilever beam subjected to axial, flexural and twisting deformations.

[1] The pavement-design package is described in Potyondy (2018). The beam contact model is referred to in commands and FISH by the name **`beam`**, and is provided as a dynamic link library (DLL) file that is loaded into *PFC3D* at runtime. The version number of the beam contact model is given by the command {**`list contact modellist`**} and listed in the "Minor" column.

TABLE OF CONTENTS

1.0 FORMULATION

The formulation of the beam contact model is the subject of this section. The first three subsections summarize the notational conventions, the PFC model and the kinematic variables — refer to Itasca (2018, PFC Model Components) for a complete description of these concepts. The remaining subsections contain the formulation, which begins with a definition of a P-beam, and is followed by the activity-deletion criteria, force-displacement law, properties, energies, methods and time step estimation scheme of the beam contact model.

1.1 NOTATIONAL CONVENTIONS

Vectors are denoted by boldface type, such as $\mathbf{v}$. The length or magnitude of $\mathbf{v}$ is denoted $\|\mathbf{v}\|$ or simply v. The addition of a hat denotes a unit vector, such that $\hat{\mathbf{v}} = \mathbf{v}/\|\mathbf{v}\|$. The addition of a dot denotes a time derivative, such as . There is a global coordinate system (xyz). The vector $\mathbf{v}$ can be expressed in the global coordinate system by the relations:

$$\begin{aligned} &\mathbf{v} = \mathbf{v}(x, y, z) = v_x \hat{\mathbf{i}} + v_y \hat{\mathbf{j}} + v_z \hat{\mathbf{k}} \\ &\text{with } v_x = \mathbf{v} \cdot \hat{\mathbf{i}}, \quad v_y = \mathbf{v} \cdot \hat{\mathbf{j}}, \quad v_z = \mathbf{v} \cdot \hat{\mathbf{k}} \end{aligned} \tag{1}$$

where $\hat{\mathbf{i}}$, $\hat{\mathbf{j}}$ and $\hat{\mathbf{k}}$ are unit vectors directed along the positive x, y and z axes, respectively.

1.2 THE PFC MODEL

The PFC programs (*PFC2D* and *PFC3D*) provide a general purpose, distinct-element modeling framework that includes a computational engine and a graphical user interface. A particular instance of the distinct-element model is referred to as a *PFC model*, which refers to both the 2D and 3D models. The PFC model simulates the movement and interaction of many finite-sized particles. The particles are rigid bodies with finite mass that move independently of one another and can both translate and rotate. Particles interact at pair-wise contacts by means of an internal force and moment. Contact mechanics are embodied in particle-interaction laws that update the internal forces and moments. The time evolution of this system is computed via the distinct-element method, which provides an explicit dynamic solution to Newton's laws of motion. The PFC model provides a synthetic material consisting of an assembly of rigid grains that interact at contacts and includes both granular and bonded materials.

We here generalize and expand upon the definition of the PFC model given above. The PFC model simulates the movement of particles and their mechanical interaction at pair-wise contacts. We denote each particle as a *body* to clarify that it is not a point mass but, instead, is a rigid body with finite mass and a well-defined surface. The PFC model consists of bodies and *contacts* (see Figure 2). There are three types of bodies: *balls*, *clumps* and *walls*. Bodies have surface properties that are assigned to the *pieces* on the body surface. A ball consists of one piece, which is the ball itself, while the pieces of a clump and wall are called *pebbles* and *facets*, respectively. A ball is a rigid unit-thickness disk in 2D or sphere in 3D. A clump is a collection of pebbles that are rigid unit-thickness disks in 2D or spheres in 3D.

Clumps model arbitrarily shaped rigid bodies. The pebbles comprising a clump can overlap but contacts do not exist between them; instead, contacts form between the pebbles on the boundary of a clump and other bodies. A wall is a collection of facets that are linear segments in 2D or triangles in 3D and that form a manifold and orientable surface.

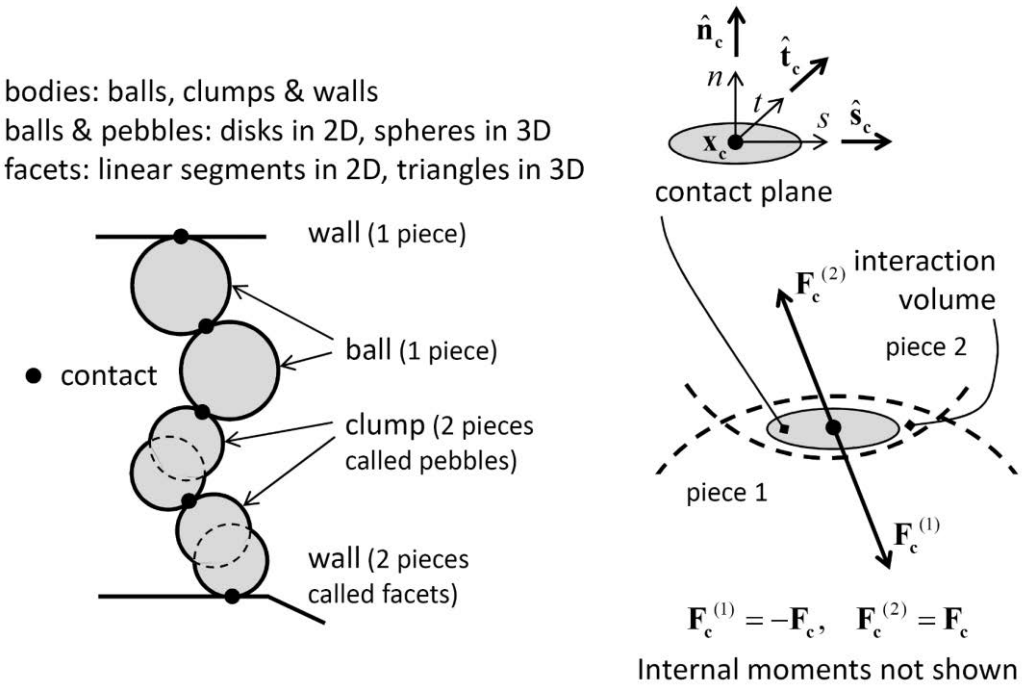

Figure 2 PFC model showing bodies and contacts (left) and contact plane with internal force (right). *(From Fig. 1 of Itasca [2018][2].)*

Contact mechanics are embodied in particle-interaction laws that employ a soft-contact approach for which all deformation occurs at the contacts between the rigid bodies. The mechanical interaction between the surfaces of two bodies occurs at one or more pair-wise mechanical contacts. Contacts are created and deleted based on body proximity by the contact-detection logic. A contact provides an interface between two pieces. The interface consists of a contact plane with location $\left(\mathbf{x}_c\right)$, normal direction $\left(\hat{\mathbf{n}}_c\right)$, and coordinate system $\left(nst\right)$. The contact plane is centered within the interaction volume (either gap or overlap) of the two pieces, oriented tangential to the two pieces, and rotated to ensure that relative motion of the piece surfaces remains symmetric with respect to the contact plane. Each contact stores a force $\left(\mathbf{F}_c\right)$ and moment $\left(\mathbf{M}_c\right)$ that act at the contact location in an equal and opposite sense on the two pieces. The internal force and moment are updated by the particle-

[2] In documentation set at PFC Model Components: PFC Model Formulation: Model Components.

interaction law, which takes the relative motion and surface properties of the two pieces as input. We refer to the particle-interaction law as a *contact model.*

1.3 KINEMATIC VARIABLES

Kinematics considers the motion of systems of bodies without regard to the role of the forces causing the motion, while kinetics considers the relationship of the forces to the kinematic variables. The kinetics of the PFC model are embodied in the force-displacement law of each contact model. The kinematic variables that serve as the input to the force-displacement law are discussed here.

Contact resolution occurs when a new contact is detected during the cycle sequence, prior to the force-displacement calculations. During contact resolution, the contact state variables (see Table 2) are updated. Each contact model uses its properties, along with the relative motion of the two contacting pieces, to update the contact force and moment.

Table 2 Contact State Variables

Property	Description
m_c	effective inertial mass
Contact plane (see Figures 2 and 3)**:**	
$\mathbf{x}_c$	contact-plane location
$\hat{\mathbf{n}}_c$	contact-plane normal direction
$\hat{\mathbf{s}}_c$	contact-plane coordinate system (s axis)
$\hat{\mathbf{t}}_c$	contact-plane coordinate system (t axis)
g_c	contact gap ($g_c > 0$ is open)
Relative motion (see Figures 4 and 5)**:**	
$\dot{\mathbf{u}}$	relative translational velocity
$\dot{\boldsymbol{\omega}}$	relative rotational velocity
$\Delta\delta_n$	relative normal-displacement increment ($\Delta\delta_n > 0$ is opening)
$\Delta\boldsymbol{\delta}_s$	relative shear-displacement increment
$\Delta\theta_t$	relative twist-rotation increment

$\Delta\boldsymbol{\theta}_{\mathbf{b}}$	relative bend-rotation increment $\left(\Delta\theta_{bs},\Delta\theta_{bt}\right)$

The contact shown in Figure 3 has been created between the pieces of two bodies. Each contact has two ends, **end1** and **end2**, with the associated pieces and bodies labelled 1 and 2. The bodies are rigid. Therefore, the motion of body $\left(b\right)$ is described by its rotational velocity $\left(\boldsymbol{\omega}^{(b)}\right)$ and the translational velocity $\left(\dot{\mathbf{x}}^{(b)}\right)$ of its centroid $\left(\mathbf{x}^{(b)}\right)$. The contact state variables include the contact-plane information as well as the contact gap $\left(g_c\right)$, which is the minimal signed distance separating the piece surfaces. A vector quantity that lies on the contact plane ($\mathbf{S}$) can be expressed in the contact plane coordinate system by the relations:

$$\begin{aligned}&\mathbf{S}=\mathbf{S}\left(s,t\right)=S_s\hat{\mathbf{s}}_{\mathbf{c}}+S_t\hat{\mathbf{t}}_{\mathbf{c}}\\&\text{with}\quad S_s=\mathbf{S}\cdot\hat{\mathbf{s}}_{\mathbf{c}},\quad S_t=\mathbf{S}\cdot\hat{\mathbf{t}}_{\mathbf{c}}.\end{aligned}\tag{2}$$

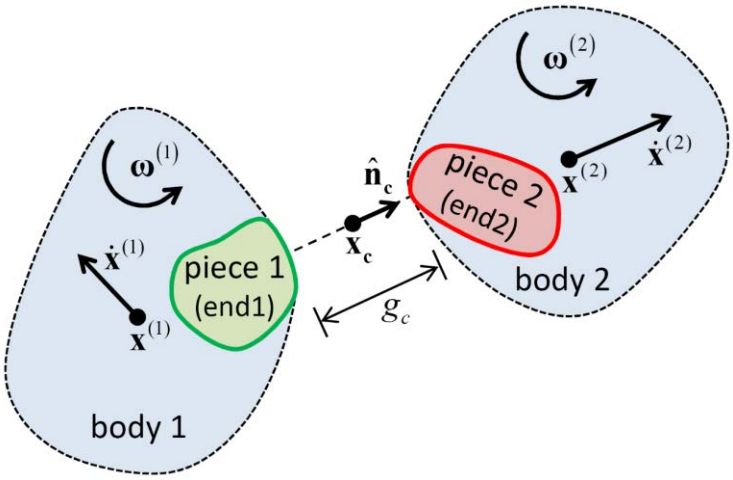

Figure 3 A contact between the pieces of two bodies. *(From Fig. 1 of Itasca [2018][3].)*

The relative motion of the piece surfaces at a contact is described by the relative translational $\left(\dot{\mathbf{u}}\right)$ and rotational $\left(\dot{\boldsymbol{\theta}}\right)$ velocities:

[3] In documentation set at PFC Model Components: Contacts and Contact Models: Contact Resolution.

$$\boldsymbol{\omega}^{(1)}. \tag{3}$$

In this expression, $\dot{\mathbf{x}}^{(b)}$ is the translational velocity of body (b) at the contact location:

$$\left(\mathbf{x}_{\mathbf{c}} - \mathbf{x}^{(b)}\right) \tag{4}$$

where $\dot{\mathbf{x}}^{(b)}$ is the translational velocity of body (b); $\boldsymbol{\omega}^{(b)}$ is the rotational velocity of body (b); $\mathbf{x}_{\mathbf{c}}$ is the contact location; and $\mathbf{x}^{(b)}$ is either the centroid (if the body is a ball or clump) or the center of rotation (if the body is a wall) of body (b). The contact location defines a point that is fixed with respect to each body, and thus, $\dot{\mathbf{x}}_{\mathbf{c}}$ is the translational velocity of that point in body (b).[4]

The relative translational velocity can be expressed as

$$\text{with} \tag{5}$$

where v_n ($v_n > 0$ is moving apart) and $\mathbf{v}_s$ are the relative translational velocities normal and tangential, respectively, to the contact plane, and the subscripts n and s correspond with normal and shear action, respectively (see Figure 4 — the centering of the contact within the interaction volume ensures that the relative displacement is symmetric with respect to the contact plane).

The relative rotational velocity can be expressed as

$$\text{with} \tag{6}$$

[4] The location of this point within each body may change — e.g., under increasing applied compression, the overlap increases and these points move deeper into each body.

where $\dot{\omega}_t$ and $\dot{\omega}_b$ are the relative rotational velocities normal and tangential, respectively, to the contact plane, and the subscripts t and b correspond with twisting and bending action, respectively (see Figure 5).

The relative displacement and rotation increments at the contact during a time step Δt are

$$\begin{aligned}
&\Delta\boldsymbol{\delta} = \Delta\delta_n \hat{\mathbf{n}}_\mathbf{c} + \Delta\boldsymbol{\delta}_\mathbf{s} \quad \left[\Delta\delta_{ss} = \Delta\boldsymbol{\delta}_\mathbf{s}\cdot\hat{\mathbf{s}}_\mathbf{c},\ \Delta\delta_{st} = \Delta\boldsymbol{\delta}_\mathbf{s}\cdot\hat{\mathbf{t}}_\mathbf{c}\right] \\
&\Delta\boldsymbol{\theta} = \Delta\theta_t \hat{\mathbf{n}}_\mathbf{c} + \Delta\boldsymbol{\theta}_\mathbf{b} \quad \left[\Delta\theta_{bs} = \Delta\boldsymbol{\theta}_\mathbf{b}\cdot\hat{\mathbf{s}}_\mathbf{c},\ \Delta\theta_{bt} = \Delta\boldsymbol{\theta}_\mathbf{b}\cdot\hat{\mathbf{t}}_\mathbf{c}\right] \\
&\text{with} \quad \Delta\delta_n = \dot{\omega}_n \Delta t, \quad \Delta\boldsymbol{\delta}_\mathbf{s} = \dot{\boldsymbol{\omega}}_\mathbf{s} \Delta t \\
&\qquad\quad \Delta\theta_t = \dot{\omega}_t \Delta t, \quad \Delta\boldsymbol{\theta}_\mathbf{b} = \dot{\boldsymbol{\omega}}_\mathbf{b} \Delta t
\end{aligned} \tag{7}$$

where $\Delta\delta_n$ is the relative normal-displacement increment, $\Delta\boldsymbol{\delta}_\mathbf{s}$ is the relative shear-displacement increment, $\Delta\theta_t$ is the relative twist-rotation increment, and $\Delta\boldsymbol{\theta}_\mathbf{b}$ is the relative bend-rotation increment.

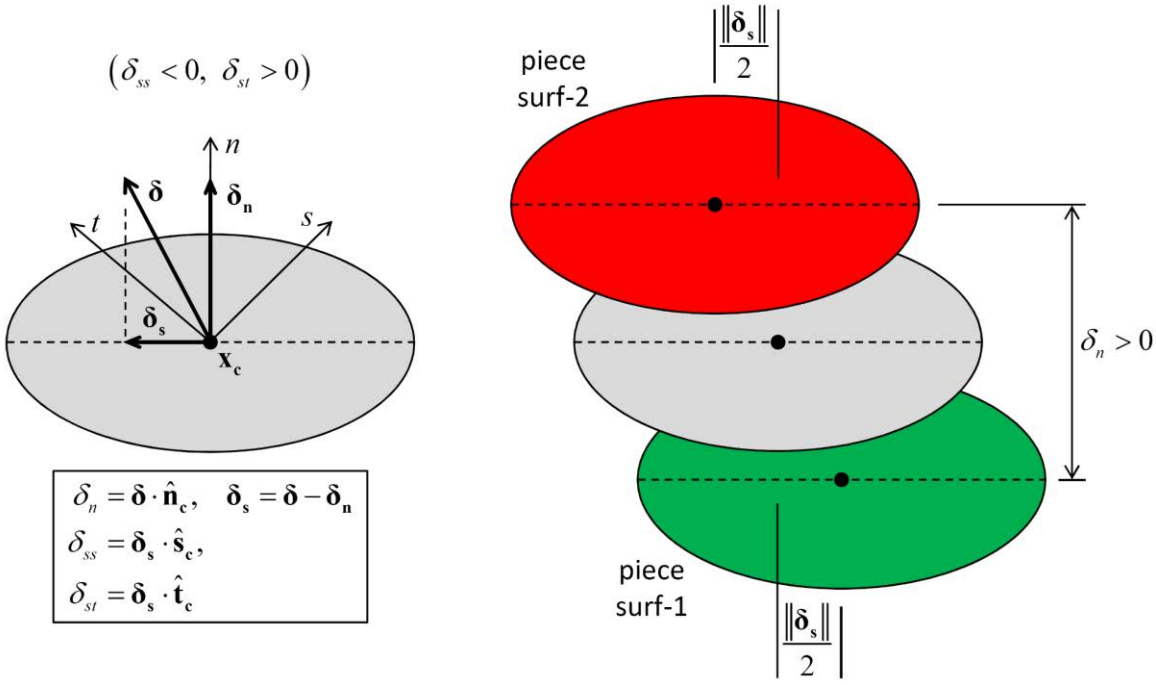

Figure 4 Kinematics of a contact showing contact plane with relative displacement and motion of piece surfaces.
(From Fig. 7 of Itasca [2018][5].)

[5] In documentation set at PFC Model Components: Contacts and Contact Models: Contact Resolution.

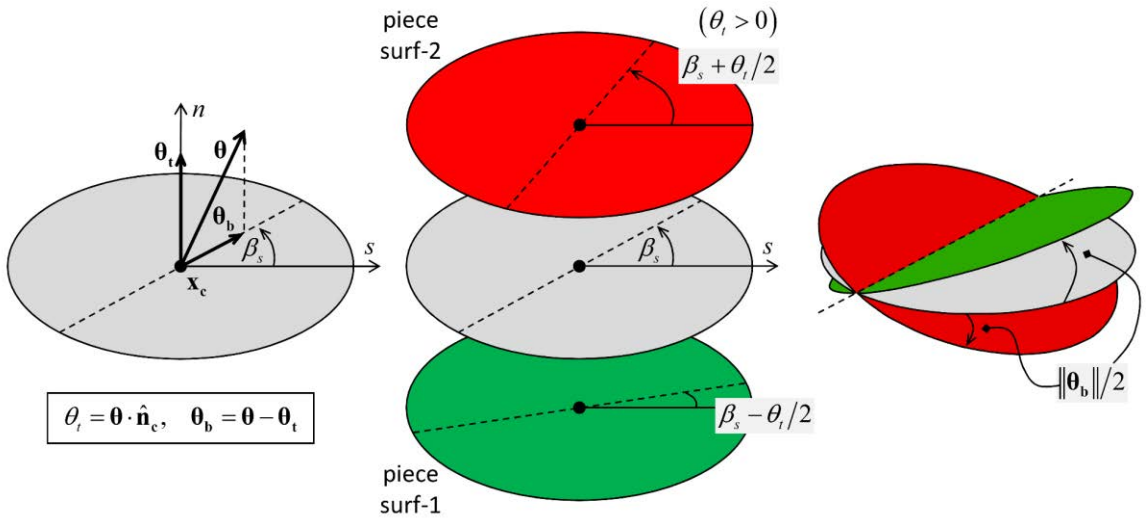

Figure 5 Kinematics of a contact showing contact plane with relative rotation and motion of piece surfaces.
(From Fig. 8 of Itasca [2018][6].)

1.4 P-BEAM

A pebbled beam (P-beam) is defined as a string of spherical balls for which the beam contact model exists at all ball-ball contacts. A P-beam provides the structural behavior of a prismatic and bisymmetrical beam composed of isotropic, linear elastic material. A P-beam is defined by the string of balls, and the ball densities (used along with ball radii to obtain ball mass). The structural properties of a P-beam are defined by the properties of each beam contact model in the string. The properties of the beam contact model are listed in Section 1.7.

There are two coordinate systems associated with the interface of the beam contact model (see Figure 6): the contact plane coordinate system (*nst*), and the beam coordinate system (*xyz*). The beam cross-sectional properties are specified in the beam coordinate system. The beam coordinate system is defined by the centers of the two contacting balls and by the vector $\mathbf{Y}$ such that: (1) the centroidal axis coincides with the *x*-axis; (2) the *x*-axis is directed from the center of ball-1 to the center of ball-2; and (3) the *y*-axis is aligned with the projection of $\mathbf{Y}$ onto the cross-sectional plane. If $\mathbf{Y}$ is not specified, or is parallel with the local *x*-axis, then $\mathbf{Y}$ defaults to the global *y*- or *x*-direction, whichever is not parallel with the local *x*-axis. For the general beam cross section shown in Figure 6, the cross-sectional properties of area (A), polar moment of inertia (J), and moments of inertia about the y- and z-axes (I_y and I_z) are defined by the integrals:

$$A = \int_A dA, \quad J = \int_A r^2 dA, \quad I_y = \int_A z^2 dA, \quad I_z = \int_A y^2 dA \tag{8}$$

[6] In documentation set at PFC Model Components: Contacts and Contact Models: Contact Resolution.

where the two principal axes of the beam cross section are defined by the *y*- and *z*-axes. The cross-sectional properties of the rectangular cross section shown in Figure 6 are given by (Ugural and Fenster, 1987, Appendix C)

$$A = bh, \quad J = \frac{bh\left(b^2 + h^2\right)}{12}, \quad I_y = \tfrac{1}{12} bh^3, \quad I_z = \tfrac{1}{12} hb^3. \tag{9}$$

The cross-sectional properties are specified directly (**bm_bhGiven = 0**), or the cross section is assumed to be rectangular (**bm_bhGiven = 1**) with specified width (b) and height (h), and the cross-sectional properties are computed internally via Eq. (9).

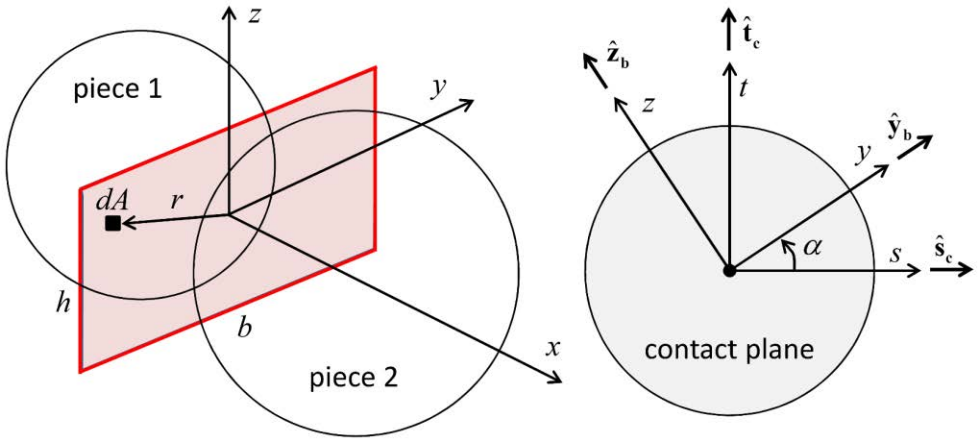

Figure 6 Beam coordinate system (xyz) with the two principal axes of the beam cross section defined by the y- and z-axes (left). Relationship between beam coordinate system and contact plane coordinate system (right).

The beam coordinate system should be defined before cycling by specifying the **bm_Ydir** property. The beam coordinate system remains fixed with respect to the contact plane coordinate system as shown in Figure 6. A beamed contact is a contact that has been assigned the beam contact model. During the first cycle after a beamed contact has been created, $\mathbf{Y}$ is projected onto the contact plane to obtain $\hat{\mathbf{y}}_b$, which is oriented at an angle α with respect to the *s*-direction. The contact model does not store α, instead it stores the cosine and sine of α given by

$$\cos\alpha = \hat{\mathbf{y}}_b \cdot \hat{\mathbf{s}}_c, \quad \sin\alpha = \hat{\mathbf{y}}_b \cdot \hat{\mathbf{t}}_c. \tag{10}$$

These terms are used to update the bending moments in the *x*- and *y*-directions (see the Force-Displacement Law). The mapping between the beam and contact coordinate systems of a vector $\mathbf{S}$ that lies on the interface is given by the relations:

$$\begin{Bmatrix} S_y \\ S_z \end{Bmatrix} = \left[\mathbf{t_{gl}}\right] \begin{Bmatrix} S_s \\ S_t \end{Bmatrix}, \quad \begin{Bmatrix} S_s \\ S_t \end{Bmatrix} = \left[\mathbf{t_{gl}}\right]^T \begin{Bmatrix} S_y \\ S_z \end{Bmatrix}$$
$$\left[\mathbf{t_{gl}}\right] = \begin{bmatrix} \cos\alpha & \sin\alpha \\ -\sin\alpha & \cos\alpha \end{bmatrix} \tag{11}$$
$$y_s = \hat{\mathbf{y}}_\mathbf{b} \cdot \hat{\mathbf{s}}_\mathbf{c} = \cos\alpha, \quad y_t = \hat{\mathbf{y}}_\mathbf{b} \cdot \hat{\mathbf{t}}_\mathbf{c} = \sin\alpha$$
$$z_s = \hat{\mathbf{z}}_\mathbf{b} \cdot \hat{\mathbf{s}}_\mathbf{c} = -\sin\alpha, \quad z_t = \hat{\mathbf{z}}_\mathbf{b} \cdot \hat{\mathbf{t}}_\mathbf{c} = \cos\alpha.$$

The beam interfaces are displayed as a microstructural plot set (see Section 3.2 in Potyondy [2018]). The beam interfaces plot set (geometry set name: **"beam interfaces"**) displays the interface of each beamed contact. The interface and *y*-axis can be displayed by the geometry plot item by specifying {Colorby: Group} and {Sets: beam interfaces}, with {Colors:} used to turn each entity on/off and specify its color. The interface is drawn as a rectangular polygon with width and height of the beam. The beam *y*-axis is drawn as a line from the interface center that extends just beyond the interface edge. If the width and height are not specified for the beam, then only the *y*-axis is drawn.

1.5 ACTIVITY-DELETION CRITERIA

A contact with the beam model is always active.

1.6 FORCE-DISPLACEMENT LAW

The force-displacement law for the beam contact model updates the contact force and moment:

$$\mathbf{F_c} = \mathbf{F}, \quad \mathbf{M_c} = \mathbf{M} \tag{12}$$

where $\mathbf{F}$ is the beam force and $\mathbf{M}$ is the beam moment. The beam force is resolved into a normal and shear force, and the beam moment is resolved into a twisting and bending moment:

$$\mathbf{F} = -F_n \hat{\mathbf{n}}_\mathbf{c} + \mathbf{F_s}, \quad \mathbf{M} = M_t \hat{\mathbf{n}}_\mathbf{c} + \mathbf{M_b} \tag{13}$$

where $F_n > 0$ is tension. The beam shear force and bending moment lie on the contact plane and are expressed in the contact plane coordinate system:

$$\mathbf{F_s} = F_{ss} \hat{\mathbf{s}}_\mathbf{c} + F_{st} \hat{\mathbf{t}}_\mathbf{c}, \quad \mathbf{M_b} = M_{bs} \hat{\mathbf{s}}_\mathbf{c} + M_{bt} \hat{\mathbf{t}}_\mathbf{c}. \tag{14}$$

When a beamed contact is created, an interface between two notional surfaces is established, and the beam force and moment are zeroed. The beamed contact provides an elastic interaction between these two notional surfaces. Each notional surface is connected rigidly to its associated ball. The beam surface gap is defined as the cumulative relative normal displacement of the ball surfaces:

$$g_s = \sum \Delta\delta_n \tag{15}$$

where $\Delta\delta_n$ is the relative normal-displacement increment of Eq. (7).

The following internal state variables are updated during the first cycle. The beam length

$$L = \left\| \mathbf{x}^{(2)} - \mathbf{x}^{(1)} \right\| \tag{16}$$

is the center-to-center distance between the two balls. The beam normal and shear stiffnesses are

$$k_n = \frac{E}{L}, \quad k_s = \frac{G}{L} = \frac{E}{2(1+\nu)L} \tag{17}$$

where E is the Young's modulus, G is the shear modulus, and ν is the Poisson's ratio.

The force-displacement law for the beam force and moment consists of the following steps.

1. Update F_n:

$$F_n := F_n + k_n A \Delta\delta_n \tag{18}$$

   where A is the cross-sectional area, and $\Delta\delta_n$ is the relative normal-displacement increment of Eq. (7).

2. Update $\mathbf{F_s}$:

$$\mathbf{F_s} := \mathbf{F_s} - k_s A \Delta\boldsymbol{\delta}_\mathbf{s} \quad \left[F_{ss} := F_{ss} - k_s A \Delta\delta_{ss},\ F_{st} := F_{st} - k_s A \Delta\delta_{st} \right] \tag{19}$$

   where A is the cross-sectional area, and $\Delta\boldsymbol{\delta}_\mathbf{s}$ is the relative shear-displacement increment of Eq. (7).

3. Update M_t:

$$M_t := M_t - k_s J \Delta\theta_t \tag{20}$$

   where J is the cross-sectional polar moment of inertia, and $\Delta\theta_t$ is the relative twist-rotation increment of Eq. (7).

4. Update $\mathbf{M_b}$:

$$M_{bs} := M_{bs} + \Delta M_{bs}, \quad M_{bt} := M_{bt} + \Delta M_{bt}$$
$$\begin{Bmatrix} \Delta M_{bs} \\ \Delta M_{bt} \end{Bmatrix} = \left[\mathbf{t_{gl}}\right]^T \begin{bmatrix} -k_n I_y & 0 \\ 0 & -k_n I_z \end{bmatrix} \left[\mathbf{t_{gl}}\right] \begin{Bmatrix} \Delta\theta_{bs} \\ \Delta\theta_{bt} \end{Bmatrix} \tag{21}$$

where I_y and I_z are the cross-sectional moments of inertia about the *y*- and *z*-axes, respectively, $\left[\mathbf{t_{gl}}\right]$ is the transformation matrix of Eq. (11), and $\Delta\boldsymbol{\theta}_\mathbf{b}$ is the relative bend-rotation increment of Eq. (7).

1.7 PROPERTIES

The property information is separated into parameters and state variables such that the parameters define the model, while the state variables describe its current state. The properties table provides a concise property reference that combines the parameters and state variables. The property information for the beam contact model is given in Tables 2–4.

Table 3 Beam Model Parameters

Parameter	Keyword	Description
	beam	model name
E	**bm_E**	Young's modulus
ν	**bm_nu**	Poisson's ratio
C_p	**bm_bhGiven**	cross-sectional properties code $\begin{cases} 0, \text{ specify directly} \\ 1, \text{ specify } b \text{ and } h \end{cases}$
A	**bm_A**	cross-sectional area $(C_p = 0)$
J	**bm_J**	polar moment of inertia $(C_p = 0)$
I_y	**bm_Iy**	moment of inertia about *y*-axis $(C_p = 0)$
I_z	**bm_Iz**	moment of inertia about *z*-axis $(C_p = 0)$
b	**bm_b**	cross-sectional width aligned with *y*-axis $(C_p = 1)$
h	**bm_h**	cross-sectional height aligned with *z*-axis $(C_p = 1)$
$\mathbf{Y}$	**bm_Ydir**	vector whose projection onto contact plane defines the beam *y*-axis

Table 4 Beam Model State Variables

Variable	Keyword	Description
L	**bm_L**	length
k_n	**bm_kn**	normal stiffness [stress/ disp.]
k_s	**bm_ks**	shear stiffness [stress/ disp.]
$\hat{\mathbf{y}}_b$	**bm_Yaxis**	beam coordinate system (*y*-axis)
$\mathbf{F}$	**bm_force**	beam force
$\mathbf{M}$	**bm_moment**	beam moment
E_k	**bm_Estr**	beam strain energy

Table 5 Beam Model Properties

Keyword	Symbol	Range	Default	Type	Modifiable
bm_E	E	$[0.0,\infty)$	0.0	FLT	yes
bm_nu	ν	$(-1.0,0.5]$	0.0	FLT	yes
bm_bhGiven	C_p	$\{0,1\}$	0	INT	yes
bm_A	A	$[0.0,\infty)$	0.0	FLT	yes
bm_J	J	$[0.0,\infty)$	0.0	FLT	yes
bm_Iy	I_y	$[0.0,\infty)$	0.0	FLT	yes
bm_Iz	I_z	$[0.0,\infty)$	0.0	FLT	yes
bm_b	b	$[0.0,\infty)$	0.0	FLT	yes
bm_h	h	$[0.0,\infty)$	0.0	FLT	yes
bm_Ydir	$\mathbf{Y}$	$[$ $]$	$(0,1,0)$	VEC3	yes
bm_L	L	$[0.0,\infty)$	NA	FLT	no
bm_kn	k_n	$[0.0,\infty)$	0.0	FLT	no
bm_ks	k_s	$[0.0,\infty)$	0.0	FLT	no
bm_Yaxis	$\hat{\mathbf{y}}_b$	$[$ $]$	NA	VEC3	no
bm_force	$\mathbf{F}$	$[$ $]$	**0**	VEC3	no
bm_moment	$\mathbf{M}$	$[$ $]$	**0**	VEC3	no
bm_Estr	E_k	$[0.0,\infty)$	0	FLT	no

1.8 ENERGIES

The beam contact model stores the strain energy as a property. The beam strain energy is updated:

$$\mathrm{E}_k = \frac{1}{2}\left(\frac{F_n^{\,2}}{k_n A} + \frac{\|F_s\|^2}{k_s A} + \frac{M_t^{\,2}}{k_s J} + \frac{M_{by}^{\,2}}{k_n I_y} + \frac{M_{bz}^{\,2}}{k_n I_z} \right). \tag{22}$$

1.9 METHODS

The beam contact model has no methods.

1.10 TIME STEP ESTIMATION SCHEME

The procedure to compute a stable time step (see Section 1.6 in the *Theory & Background* volume of Itasca [2008]) requires that each contact model return the contact translational and rotational stiffnesses. For the beam model, the translational stiffnesses are

$$\tilde{k}_n \quad \text{[illegible]} \qquad \tilde{k}_s \quad \text{[illegible]} \tag{23}$$

and the rotational stiffnesses are

$$\tilde{k}_t \quad \text{[illegible]}, \qquad \tilde{k}_b \quad \text{[illegible]}\left(I_y, I_z\right). \tag{24}$$

2.0 TEST PROBLEM

A test problem of a tip-loaded cantilever beam is provided for the beam contact model.

2.1 TIP-LOADED CANTILEVER BEAM

The cantilever beam test problem is in the **`BeamContactModel\Test-Beam(rectXC)`** example-project directory. The problem is shown in Figures 7 and 8. The beam ends are denoted by 1 and 2. The beam is fully fixed at end 1, and different deformations are imposed at end 2 to provide three loading cases corresponding with axial, twisting, and flexural deformations. The closed-form expressions (McGuire et al., 1979) shown in the figures give the force and moment at the beam ends for each loading case.

The beam is comprised of polypropylene material with a density (ρ), Young's modulus (E), and Poisson's ratio (ν) of $946\ \mathrm{kg/m^3}$, 1.2 GPa, and 0.42, respectively. The beam has a length (L) of 44 mm, and a rectangular cross section with a width (b) and height (h) of 4 and 1 mm, respectively. The cross-sectional properties of the rectangular cross section are given by Eq. (9). The closed-form expressions give the forces and moments at the beam ends, which are compared with the *PFC3D* model response below.

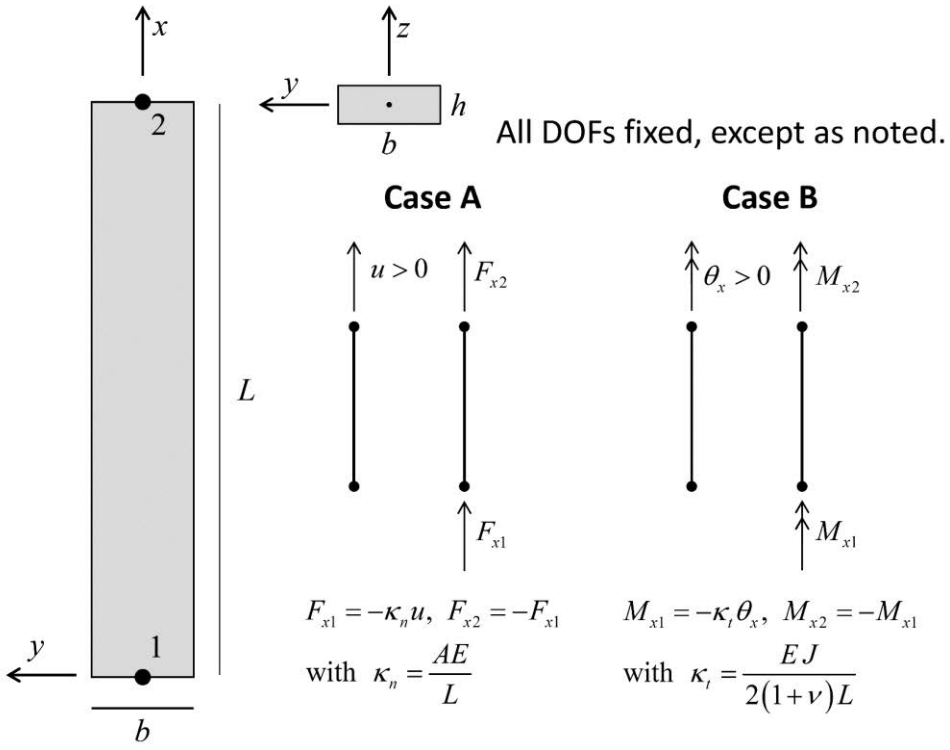

Figure 7 Cantilever beam test problem with loading cases for axial and twisting deformation.

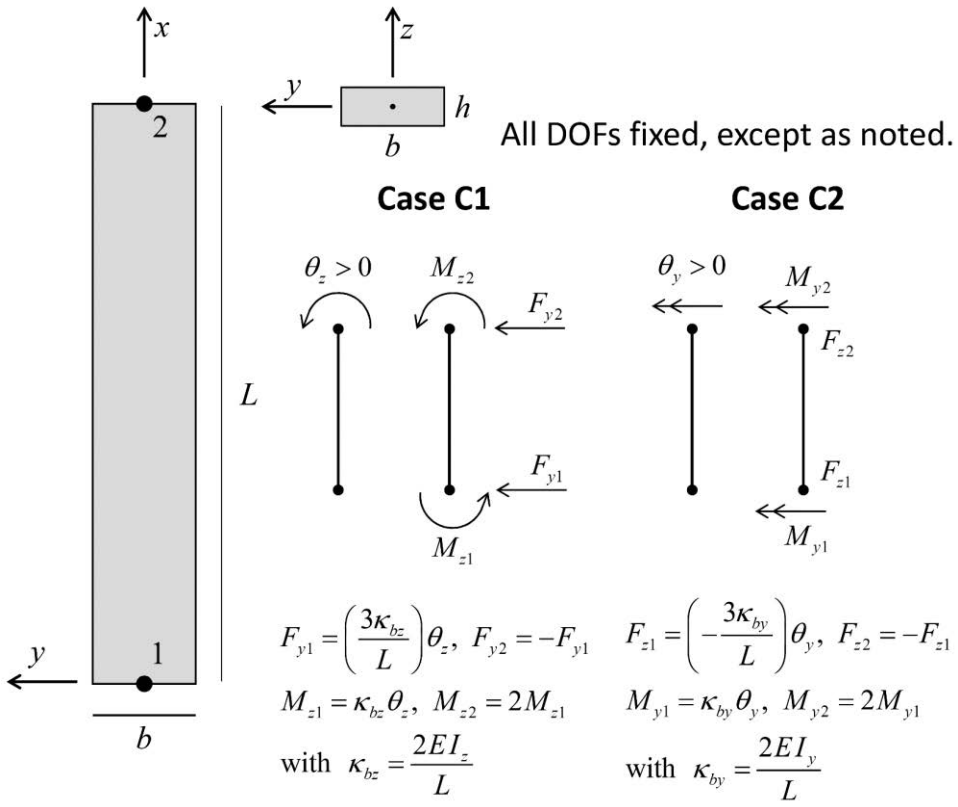

Figure 8 Cantilever beam test problem with loading cases for flexural deformation about the two principal axes of the beam cross section.

The beam is modeled as a collection of 12 balls joined by beam contacts (see Figure 9). All balls have a 4-mm diameter such that the end balls lie at the beam ends, and the 10 interior balls are placed next to one another with no overlap. The elastic constants, width and height of the beam cross section, and alignment of the *y*-axis are specified by assigning all beam contacts the properties:

$$\begin{aligned} &E = 1.2\ \text{GPa}, \quad \nu = 0.42 \\ &C_p = 1, \quad b = 4\ \text{mm}, \quad h = 1\ \text{mm}, \quad \mathbf{Y} = (0,1,0). \end{aligned} \tag{25}$$

For this model, the beam *y*-axis corresponds with the global *y*-axis. The motion of the end balls is specified, and the interior balls are free to move in response to this imposed deformation. The end-1 ball is fully fixed, and the motion of the end-2 ball differs for each loading case.[7] After the end motions have been imposed, the model is cycled until static equilibrium is reached. The externally applied force and moment acting on the end balls are compared with the values from the closed-form solution for each loading case. The relative error for all cases is less than 3%. The flexural deformation of loading case C1 is evident in Figure 10, which shows the undeformed and deformed beams.

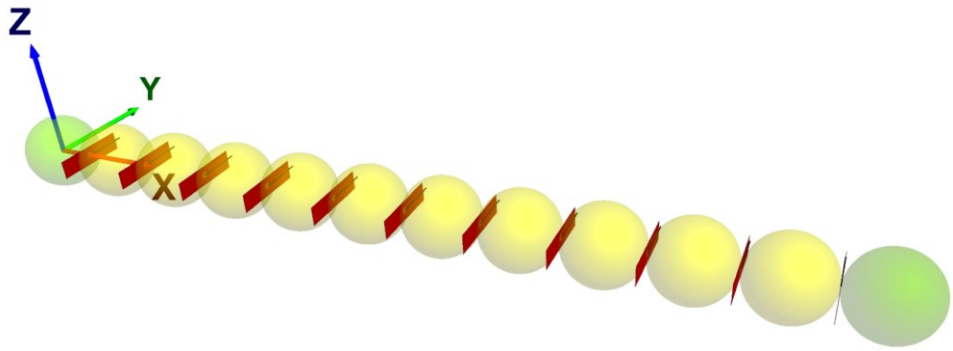

Figure 9 PFC3D model of cantilever-beam test problem showing the balls, beam interfaces, and global axes.

$$\text{Case A:}\quad u = 1 \text{ mm}$$

$$F_{x1} = \begin{cases} -1.0909 \times 10^{2} \text{ N}, & \text{analytical} \\ -1.0909 \times 10^{2} \text{ N}, & \text{numerical} \\ 0, & \text{relative error} \end{cases} \tag{26}$$

$$\text{Case B:}\quad \theta_x = 0.2 \text{ rad}$$

$$M_{x1} = \begin{cases} -1.0883 \times 10^{-2} \text{ Nm}, & \text{analytical} \\ -1.0883 \times 10^{-2} \text{ Nm}, & \text{numerical} \\ 0, & \text{relative error} \end{cases} \tag{27}$$

[7] For the flexural loading cases, the end-2 ball is freed in the x-direction to allow the beam to contract in the x-direction. If this is not done, then an axial force develops in the beam, and the PFC3D model exhibits stress stiffening such that the closed-form solution based on simple beam theory is no longer valid.

Case C1: $\theta_z = 0.2$ rad

$$F_{y1} = \begin{cases} 3.9669 \text{ N, analytical} \\ 3.9113 \text{ N, numerical} \\ 1.4\%, \text{ relative error} \end{cases} \tag{28}$$

$$M_{z1} = \begin{cases} 5.8182\times10^{-2} \text{ Nm, analytical} \\ 5.6846\times10^{-2} \text{ Nm, numerical} \\ 2.3\%, \text{ relative error} \end{cases}, \quad M_{z2} = \begin{cases} 1.1636\times10^{-1} \text{ Nm, analytical} \\ 1.1481\times10^{-1} \text{ Nm, numerical} \\ 1.3\%, \text{ relative error} \end{cases}$$

Case C2: $\theta_y = 0.2$ rad

$$F_{z1} = \begin{cases} -2.4793\times10^{-1} \text{ N, analytical} \\ -2.4988\times10^{-1} \text{ N, numerical} \\ 0.8\%, \text{ relative error} \end{cases} \tag{29}$$

$$M_{y1} = \begin{cases} 3.6364\times10^{-3} \text{ Nm, analytical} \\ 3.6718\times10^{-3} \text{ Nm, numerical} \\ 1.0\%, \text{ relative error} \end{cases}, \quad M_{y2} = \begin{cases} 7.2727\times10^{-3} \text{ Nm, analytical} \\ 7.2942\times10^{-3} \text{ Nm, numerical} \\ 0.3\%, \text{ relative error} \end{cases}$$

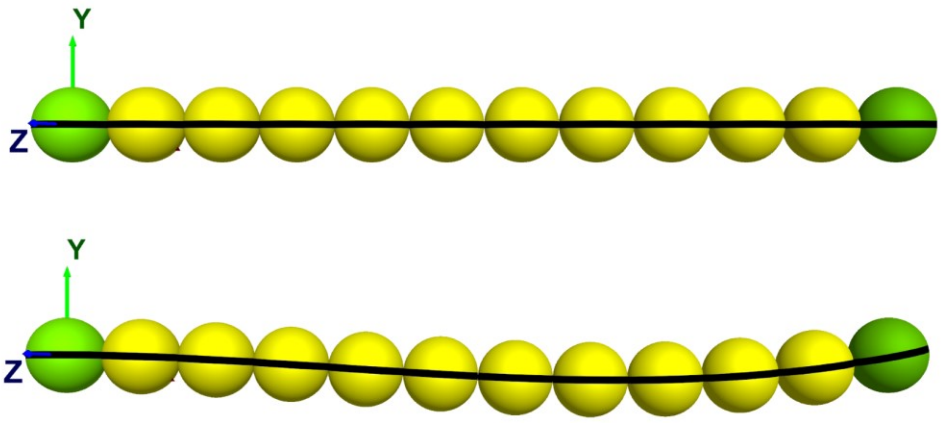

Figure 10 **PFC3D model of cantilever-beam test problem at the start (top) and end (bottom) of loading case C1.**

3.0 REFERENCES

Itasca Consulting Group, Inc. (2018) ***PFC — Particle Flow Code in 2 and 3 Dimensions***, Version 5.0, Documentation Set of version 5.00.35 [March 21, 2018]. Minneapolis: Itasca.

Itasca Consulting Group, Inc. (2008) ***PFC3D — Particle Flow Code in 3 Dimensions***, Version 4.0, User's Manual. Minneapolis: Itasca.

McGuire, W., and R.H. Gallagher. (1979) ***Matrix Structural Analysis***, New York: John Wiley & Sons.

Potyondy, D. (2018) "Pavement-Design Package for PFC3D [pdPkg14]," Itasca Consulting Group, Inc., Technical Memorandum ICG16-8528-15TM (June 22, 2018), Minneapolis, Minnesota.

Potyondy, D. (2017) "Material-Modeling Support in PFC [fistPkg25]," Itasca Consulting Group, Inc., Technical Memorandum ICG7766-L (March 16, 2017), Minneapolis, Minnesota.

Ugural, A.C., and S.K. Fenster. (1987) ***Advanced Strength and Applied Elasticity***, Second SI Edition, New York: Elsevier.